
8-2014

Volumetric Scintillation Dosimetry For Scanned Proton Beams

Daniel G. Robertson

Follow this and additional works at: https://digitalcommons.library.tmc.edu/utgsbs_dissertations



Part of the [Medicine and Health Sciences Commons](#), and the [Other Physics Commons](#)

Recommended Citation

Robertson, Daniel G., "Volumetric Scintillation Dosimetry For Scanned Proton Beams" (2014).
Dissertations and Theses (Open Access). 473.
https://digitalcommons.library.tmc.edu/utgsbs_dissertations/473

This Dissertation (PhD) is brought to you for free and open access by the MD Anderson UTHealth Houston Graduate School at DigitalCommons@TMC. It has been accepted for inclusion in Dissertations and Theses (Open Access) by an authorized administrator of DigitalCommons@TMC. For more information, please contact digcommons@library.tmc.edu.

VOLUMETRIC SCINTILLATION DOSIMETRY FOR SCANNED PROTON BEAMS

by

Daniel Gordon Robertson, B.S.

APPROVED:

Sam Beddar, Ph.D.
Supervisory Professor

Geoffrey Ibbott, Ph.D.

Dragan Mirkovic, Ph.D.

Arvind Rao, Ph.D.

Narayan Sahoo, Ph.D.

Richard Wendt III, Ph.D.

APPROVED:

Dean, The University of Texas
Graduate School of Biomedical Sciences at Houston

VOLUMETRIC SCINTILLATION DOSIMETRY FOR SCANNED PROTON BEAMS

A
DISSERTATION

Presented to the Faculty of
The University of Texas
Health Science Center at Houston
and
The University of Texas
MD Anderson Cancer Center
Graduate School of Biomedical Sciences
in Partial Fulfillment

of the Requirements

for the Degree of

DOCTOR OF PHILOSOPHY

by

Daniel Gordon Robertson, B.S.
Houston, Texas

August 2014

The glory of God is intelligence, or, in other words, light and truth.

- Doctrine and Covenants 93:36

ACKNOWLEDGEMENTS

I would like to thank my advisor, Dr. Sam Beddar, for his patient mentoring and for believing in me and in my potential as a researcher. He taught my many things about being a scientist that I couldn't have learned in books. I'm grateful that he pushed me to do many things that I didn't want to do at the time, but that have proved to be invaluable learning experiences.

I would also like to thank the members of my advisory committee, Dr. John Cook, Dr. Geoffrey Ibbott, Dr. Dragan Mirkovic, Dr. Arvind Rao, Dr. Narayan Sahoo, and Dr. Richard Went III, for their time and support and for the wisdom and perspective they shared with me. I would particularly like to thank Dr. Mirkovic for all of his Monte Carlo help, Dr. Wendt for his mentoring and many interesting discussions, and Dr. Sahoo for his endless patience and for never being too busy to help me with anything I needed to do at the proton therapy center. I also want to thank other faculty members who have mentored me, including Dr. Radhe Mohan, Dr. Xiaodong Zhang, Dr. Uwe Titt, Dr. Gabriel Sawakuchi, and Dr. Jeremy Polf.

Many thanks go to Norma Hall, Afra Gatson, Georgeanne Moore, and Gloria Mendoza, who have looked out for my best interests and taken care of countless administrative requirements so that I could spend my time and energy on my studies.

I am also grateful to the faculty and staff at the proton therapy center for their endless helpfulness, for giving me as much beam time as I needed, and for putting up with my growing piles of experimental apparatus. Special thanks go to Matt Kerr for his help on many late nights and early mornings of measurements.

I must thank the members of my research group, Francois Therriault-Proulx, Landon Wootton, Becket Hui, and David Klein, for many helpful and productive discussions and for detailed scrutiny of my papers and presentations. More importantly, their true friendship and

good humor made work an enjoyable place to be and helped to soften many of the bumps along the way.

I gratefully acknowledge the financial support I have received from the National Cancer Institute through award number P01CA021239. I am also grateful to the Sowell and Huggins families, the Cancer Answers Foundation, and the Presidents of UTHHealth and the UT MD Anderson Cancer Center, whose scholarship awards have given me confidence that I have a chance at being a successful researcher.

The teachers and mentors who have influenced me throughout my life and helped bring me to this point are too numerous to mention. However, I would like to particularly thank my 5th Grade teacher Jon Bagley for encouraging me to strive for excellence, and my undergraduate research advisor Dr. Branton Campbell, for his dedicated personal mentoring even after I parted ways with Materials Science.

Special thanks go to Dr. Ray Richards for introducing me to the world of Medical Physics and gently nudging me towards it, as well as to Dr. Harald Paganetti and Dr. Joao Seco for giving me such an excellent first experience in the field.

I would like to thank my wonderful church family at Hermann Park Ward of The Church of Jesus Christ of Latter-day Saints, for giving me a home away from home and helping me to keep an eternal perspective.

I can't express my gratitude enough to my wonderful parents, Mark and Theresa Robertson, who provided me with a loving, happy home, who taught me to be a good person, and who have always encouraged me to do my best. Thanks go also to my siblings Rachel, Becky, and David, for their love and friendship throughout my life and for always helping me to remember who I am. Thank you Baby Mark, for bringing such joy into my life, and for your love and smiles, even when daddy gets home late from work.

Finally, I want to express my gratitude to my brilliant wife Angie. Thank you for your love and support throughout this adventure. Thank you for being such a good mother to Mark and for keeping track of so many details in our life that would otherwise have been forgotten or neglected. Thank you for many valuable insights into my research and the world of academia. Thank you for your encouragement and understanding and patience through the high and low times. I'm so grateful to have you as my eternal companion and to be a co-investigator with you in our continual search for truth.

VOLUMETRIC SCINTILLATION DOSIMETRY FOR SCANNED PROTON BEAMS

Daniel Gordon Robertson, B.S.

Advisory Professor: Sam Beddar, PhD

Scanned beam proton therapy is a promising cancer treatment modality which is becoming more widely available with the increasing number of proton radiotherapy centers. Scanned proton beams can produce complex 3D dose distributions, presenting a challenge for adequate quality assurance testing. Because each scanned beam dose measurement requires the delivery of the entire field, multiple measurements can be time consuming. These quality assurance challenges limit the number of patients who can be treated with this modality. The overall objective of this project is to increase the safety and availability of complex proton therapy treatments by developing a fast volumetric scintillation detector.

Volumetric scintillation dosimetry is a new technique with the potential to provide fast, high-resolution measurements of scanned proton beams. Initial studies using scintillation dosimetry for IMPT quality assurance have shown promise, despite quenching effects caused by the nonlinear response of the scintillator to low-energy protons. All previous studies have used a single camera to image a tank of scintillator. However, to obtain real-time 3D information, at least two cameras are required. The purpose of this study is to develop a dual-camera volumetric scintillation dosimetry system and test its capabilities for quality assurance of scanned proton beams.

A prototype detector was built, consisting of a tank of LS imaged by two orthogonally-positioned CCD cameras. The optical response of the system was evaluated, and correction methods were developed for optical artifacts. Quenching correction methods were developed

to preserve the linearity of dose measurement in the Bragg peak. The new detector was used to measure the range, lateral profile, and lateral position of scanned proton beams of multiple energies and lateral locations. A high level of accuracy was obtained with the range and lateral profile measurements. The lateral position measurements were precise but suffered from systematic errors related to uncertainties in the day-to-day setup of the detector.

The new detector design shows the potential to significantly improve the efficiency and comprehensiveness of quality assurance measurements for scanned proton beam delivery systems. It provides the novel capability of measuring the proton beam range, lateral profile, and lateral position simultaneously and rapidly with high resolution. These capabilities will facilitate increased patient safety and an improved capacity to detect beam delivery errors.

TABLE OF CONTENTS

Acknowledgements.....	iv
Abstract.....	vii
Table of Contents.....	ix
List of Figures.....	xiii
List of Tables	xvii
Chapter 1: Introduction	1
1.1 Purpose statement	2
1.2 Rationale and significance.....	2
1.3 Hypothesis.....	3
1.4 Specific aims	4
1.5 Dissertation organization	4
Chapter 2: Background	6
2.1 Proton radiation therapy	7
2.2 Motivation for proton therapy.....	7
2.3 Proton interactions with matter.....	8
2.4 Scanned beam proton therapy	10
2.5 Quality assurance for scanned beam proton therapy	10
2.6 Dosimeters used for scanned proton beam QA	11
2.7 Scintillation dosimetry	13
2.8 Ionization quenching of scintillation light.....	14
Chapter 3: Optical artifact characterization and correction in volumetric scintillation dosimetry	16
3.1 Introduction.....	17

3.1.1 Scintillator tank artifacts.....	18
3.1.2 Optical train artifacts.....	20
3.1.3 CCD artifacts	20
3.2 Materials and methods	21
3.2.1 Liquid scintillator detector	22
3.2.2 Artifact analysis and correction methods	23
3.2.2.1 CCD artifacts	23
3.2.2.2 Lens artifacts.....	24
3.2.2.3 Scintillator tank artifacts.....	28
3.2.3 Artifact correction evaluation methods.....	30
3.2.3.1 Proton beam measurements.....	31
3.2.3.2 Monte Carlo calculations.....	32
3.3 Results	33
3.3.1 CCD artifacts	33
3.3.2 Lens artifacts.....	35
3.3.3 Scintillator tank artifacts.....	37
3.3.4 Artifact correction evaluation	40
3.4 Discussion.....	44
3.4.1 Point spread function.....	44
3.4.2 Gamma analysis.....	45
3.4.3 Sources of error	46
3.4.4 Reflections.....	47
3.5 Conclusions	47
Chapter 4: Quenching correction	49
4.1 Introduction.....	50

4.2 Materials and methods	52
4.2.1 Quenching model	52
4.2.2 Quenching correction factors.....	53
4.2.3 LS detector system.....	54
4.2.4 Image processing	55
4.2.5 Monte Carlo LET and dose data.....	56
4.2.6 Analytical LET calculation	56
4.2.7 Quenching parameter determination	57
4.2.8 Quenching correction.....	59
4.3 Results	59
4.3.1 Miniature LS detector linearity.....	59
4.3.2 LET calculation	60
4.3.3 Quenching parameter determination	63
4.3.4 Quenching correction.....	64
4.4 Discussion.....	67
4.5 Conclusions	68
Chapter 5: Quality assurance of scanned proton beam delivery systems with a 3D	
liquid scintillator detector	70
5.1 Introduction.....	71
5.2 Materials and methods	74
5.2.1 Detector design	74
5.2.2 Detector calibration	77
5.2.3 Scanned proton beam delivery system.....	78
5.2.4 General measurement parameters	78
5.2.5 Study 1: Beam range measurement.....	79

5.2.5.1 Measurement parameters.....	79
5.2.5.2 Data processing procedure.....	79
5.2.5.3 Data analysis	82
5.2.6 Study 2: Lateral position measurement.....	82
5.2.6.1 Measurement parameters.....	82
5.2.6.2 Data processing procedure.....	83
5.2.6.3 Data analysis	87
5.2.7 Study 3: Lateral profile measurement	87
5.2.7.1 Measurement parameters.....	87
5.2.7.2 Data processing procedure.....	87
5.2.7.3 Data analysis	88
5.3 Results	88
5.3.1 Study 1: Beam range measurement.....	88
5.3.2 Study 2: Lateral position measurement.....	91
5.3.3 Study 3: Lateral profile measurement	93
5.4 Discussion.....	95
5.5 Conclusions	96
Chapter 6: Conclusions and future directions.....	98
6.1 Summary and Conclusions	99
6.2 Evaluation of the hypothesis.....	101
6.3 Future directions.....	103
Bibliography	105
Vita.....	115

LIST OF FIGURES

Figure 2.1 The central-axis depth-dose curve of a 161.6 MeV proton beam. The peak near the end of the beam range is known as the Bragg peak.	8
Figure 3.1 Workflow of the optical artifact correction process.	21
Figure 3.2 Liquid scintillator detector system.	22
Figure 3.3 The angle θ used in the ‘cos ⁴ θ rule’ for camera vignetting is defined as the angle between the camera’s optical axis and the ray from the exit pupil of the lens to measurement point x on the image sensor.	25
Figure 3.4 Consider a pinhole camera located at point C. a) The camera is focused on the focal plane (FP) where $\overline{O_1C}$ is the focal length. Photons originating from line \overline{MC} will be translated to the point X in the FP in the CCD image. For example, point P of the proton track (PT) will be mapped to point X at the FP. The apparent location of P will be shortened from $\overline{O_2P}$ to $\overline{O_1X}$ in the FP. b) In the presence of the liquid scintillator (LS), the photon beam is bent at the LS-air junction, causing another displacement of apparent location to a different point at the FP. The correction algorithm calculates the mapping from X back to P. In addition, it corrects the pixel values altered by the change in apparent pixel size.	29
Figure 3.5 Experimental setup for proton beam measurements with the scintillator detector.	32
Figure 3.6 The mean pixel value of the CCD for dark frame images of various exposure lengths.	34
Figure 3.7 The lateral profile of a 100.9-MeV proton pencil beam before (black) and after (grey) application of a 3x3 spatial median filter. The median filter effectively	

removed the transient spike caused by stray radiation incident on the CCD chip without affecting the underlying light distribution.	35
Figure 3.8 The measured vignetting as a function of distance from the lens centre (dashed line) is compared to the $\cos^4(\theta)$ function (solid line) used to model the vignetting.....	36
Figure 3.9 The lens distortion model of the CCD camera. The direction and magnitude of the arrows indicate the direction and relative magnitude of the pixel position corrections. The contour plot indicates the magnitude of pixel position corrections in units of pixels. The '×' indicates the image centre, and the '○' marks the principal point of the camera.	37
Figure 3.10 The PSF of the scintillator detector, measured at a distance of 3 cm (green), 10 cm (blue), and 19 cm (red) behind the tank window, and the PSF of the lens measured in air at a distance equivalent to 10 cm behind the tank window (blue dashed).....	39
Figure 3.11 The lateral profile at the Bragg peak of a 144.9 MeV proton pencil beam, delivered at a distance of 5 cm (blue), 10 cm (green), and 15 cm (red) behind the tank window.....	40
Figure 3.12 Central-axis comparison of light signals from Monte Carlo calculations (dashed line) and the raw (gray) and corrected (black) CCD images.....	41
Figure 3.13 Gamma analysis pass maps with gamma criteria of 2% and 2mm for 85.6-MeV (left) and 144.9-MeV (right) proton pencil beams. Passing pixels are in red, and failing pixels are in green. The blue pixels are below the dose threshold (5% of maximum dose) and were not considered in the gamma analysis. Top) Uncorrected CCD images. Bottom) Corrected CCD images.....	43
Figure 4.1 Schematic of LS detector system.....	55

Figure 4.2 Schematic of miniature LS detector.....	57
Figure 4.3 The results of a linearity test of a miniature LS detector in a 6-MV photon beam. The scintillation light (red) was measured by subtracting the Cerenkov signal (blue) from the miniature LS detector signal (green). The R2 value of a linear fit to the scintillation signal was 0.9999.	60
Figure 4.4 (top) Track-averaged LET calculated with Monte Carlo methods and with an analytical formula for a 100.9-MeV proton beam in LS. (bottom) The difference between the analytically-derived LET values to the Monte Carlo-derived values.....	61
Figure 4.5 The Monte Carlo LET calculation shows an off-axis LET increase of up to 22% in pixels containing 1% or more of the peak dose. The lateral dose profile is shown for reference.....	62
Figure 4.6 (top) Central axis depth-dose profiles for proton pencil beams. The dose calculated by the validated Monte Carlo model is shown in black. The uncorrected scintillation signal is shown in blue. The corrected scintillation signal is shown in red. (bottom) The ratio of the corrected scintillation signal to the Monte Carlo dose.....	63
Figure 4.7 (top) The light signal from the miniature LS detectors before (+) and after (x) the correction factor was applied. The dose from the Monte Carlo calculation is shown for comparison. (bottom) The ratio of the corrected light signal (DLS) to the Monte Carlo dose (DMC).	64
Figure 4.8 The measured scintillation signal (top), the dose calculated using Monte Carlo methods (centre), and the corrected scintillation signal (bottom) for a 100.9-MeV proton pencil beam.	65

Figure 4.9 Lateral dose profiles for a 144.9-MeV proton pencil beam at three depths: a) 3.5 cm (proximal build-up region), b) 14.9 cm (proximal 50% dose), and c) 15.9 cm (centre of Bragg peak).....	66
Figure 5.1 A schematic of the dual-camera detector design.	75
Figure 5.2 A series of proton beam scintillator depth-light curves used for beam range calibration (blue -), with the distal 80% of the light curve marked for each beam (black +).....	80
Figure 5.3 The measured distal 80% light signal vs. the nominal range (black +), and a calibration fit to the data (red -).....	81
Figure 5.4 The distance of closest approach of the projected rays for all image pairs from the two cameras, (a) before and (b) after optimization of the focal length and the camera tilt angle.	86
Figure 5.5 The depth-light curves of 60 beam energies measured with the scintillator detector. The first 2 cm of the light signal is absent due to the passage of the beam through the tank wall and tank-edge artifacts.....	89
Figure 5.6 The measured (black +) and nominal (red •) lateral positions of proton beams of 5 energies at the isocenter plane.	92
Figure 5.7 The full width at half-maximum (FWHM) of proton beams ranging from 72.5 MeV to 168.8 MeV, measured with the scintillator detector (black +) and a pinpoint ionization chamber (red •).....	93
Figure 5.8 The lateral profile of a 131.0 MeV proton beam at a depth of 2 cm, measured with the scintillator detector (black +) and a pinpoint ionization chamber (red •). The spikes in the scintillator signal at -60 mm and 55 mm are reflections from screws in the scintillator tank assembly.	94

LIST OF TABLES

Table 3.1 Optical artifacts in a volumetric scintillation dosimetry system.....	18
Table 3.2 Gamma analysis pass rates for proton pencil beam light distributions measured with the scintillator detector, as compared to projected dose distributions calculated using Monte Carlo methods.	42
Table 3.3 Differences in gamma analysis (2%, 2 mm) pass rates for measured CCD images lacking one of the optical artifact correction steps, as compared to projected dose distributions calculated using Monte Carlo methods. The comparison was performed for four beam energies.	44
Table 4.1 Peak-to-plateau ratios for the Monte Carlo dose calculation, the measured signal from the CCD, and the corrected CCD signal.	67
Table 4.2 Percentage difference between the calculated peak height and the peak height from the measured and corrected CCD signals.	67
Table 5.1 The mean and standard deviation of the corner-corner distances of the checkerboard calibration pattern before and after optimization of the camera-tank distances. The actual distance is 13.7 mm.	85
Table 5.2 Measured and nominal proton beam ranges.	89
Table 5.3 The difference between the nominal lateral position and the mean of the measured position, as well as the standard deviation of the measured locations.	92
Table 5.4 Mean and standard deviation of proton beam FWHM for five beam energies.	94

CHAPTER 1

INTRODUCTION

1.1 Purpose statement

The main objective of my research is to develop fast, high-resolution, 3D radiation detectors based on liquid scintillators. Scintillators convert the energy from ionizing radiation beams into visible light, which can then be recorded with a camera and converted into radiation dose. During my doctoral research I have designed and characterized an improved scintillator detector, developed methods to convert the measured scintillation light into appropriately scaled radiation dose values, and tested procedures for applying this new detector to clinical quality assurance tasks at the MD Anderson Proton Therapy Center. This detector design has the potential to improve patient safety by providing more detailed measurements of radiation treatment plans than current detectors. It is also expected to increase access to complex proton therapy treatments by reducing the time required for quality assurance tests.

1.2 Rationale and significance

Radiation therapy technology for cancer treatment has advanced rapidly in recent years, and the complexity of treatments has skyrocketed in the pursuit of higher radiation doses to tumors and decreased damage to healthy tissues. The availability of three-dimensional (3D) anatomical imaging has led to the use of increasingly complex radiation treatment techniques incorporating heterogeneous doses and steep dose gradients near critical structures. The safety and accuracy of these treatments depends on verification measurements, but obtaining these measurements has become increasingly difficult as treatment fields have become more complex. While modern radiotherapy fields have complex 3D features, the standard measurement tools are point detectors and 2D detector arrays. As a result, verification procedures can be very time consuming, even while measuring the dose at only a few points. Ideally, 3D dose distributions would be measured prior to treatment for all

patients. Unfortunately, this is impractical because of time constraints and the limited availability of suitable detectors.

In the last decade, proton radiation therapy has matured from an experimental cancer therapy to a mainstream, cutting edge treatment modality. There are currently 14 proton therapy centers in the United States, with 12 new centers under development. Internationally, there are 25-30 operational proton therapy centers with more in development. The interest in proton therapy springs from significantly improved radiation dose distributions and decreases in the dose to healthy tissues compared to other treatment modalities.

One of the major challenges to a clinical proton therapy facility is performing detailed QA measurements of the beam delivery system and patient treatment fields. These measurements have the conflicting goals of being comprehensive and efficient. This is particularly challenging with scanned proton beam delivery systems because of the temporal dependence of the dose delivery and the presence of sharp dose gradients, which result in long measurement periods and the need for high-resolution detectors.

Volumetric scintillation detectors feature high spatial and temporal resolution and immediate readout, and they are capable of measuring an entire radiation field in a single measurement. These features could increase the accuracy and comprehensiveness of QA and significantly decrease the time required for measurements, leading to improved patient safety and greater availability of advanced proton therapy treatments.

1.3 Hypothesis

A large liquid scintillator detector can measure three-dimensional dosimetric information in scanned proton beams within 3% or 3 mm to agreement with calculated doses. Dose distributions and the locations and profiles of individual pencil beams can be measured during a single delivery of each treatment field.

1.4 Specific aims

1) Characterization and correction of optical artifacts: The optical artifacts inherent in volumetric scintillation detectors will be evaluated, and correction methods will be developed for each source of error. Optical artifacts including parallax, reflection, refraction, lens aberrations, and light scattering will be considered.

2) Quenching correction: The signal loss due to quenching in LS proton beam measurements will be determined by comparing measured light distributions to calculated and measured doses. Linear energy transfer (LET) distributions of mono-energetic proton beams will be calculated using analytical and Monte Carlo methods. The quenching parameter, a material-specific constant describing the amount of quenching in a scintillator, will be measured for the LS used in this study. A semi-empirical quenching correction method will be developed using a known relationship between LET and light emission. This model will be used to obtain 3D quenching correction factors based on LET calculations and the measured value of the LS quenching parameter.

3) 3D dosimetric evaluation: A LS dosimetry system will be constructed consisting of a 20x20x20 cm³ volume of LS, imaged simultaneously by two orthogonal high-speed CCD cameras. The beam ranges, lateral locations, and lateral profiles of proton pencil beams will be measured and compared with ionization chamber measurements and the nominal values of these parameters for the PTHC. The accuracy and precision of these measurements will be determined. Recommendations will be made for use of the scintillator detector in quality assurance of scanned proton beam delivery systems.

1.5 Dissertation organization

The remaining chapters of this dissertation include one chapter of general background information and three chapters dedicated to the results of the three specific aims listed above.

Each of the chapters reporting on the specific aims contains its own introduction, materials and methods, results, discussion, and conclusions. A final chapter summarizes the findings and conclusions and indicates the direction of future work.

The remaining chapters of this dissertation are organized as follows:

Chapter 2 gives background information beyond that which is contained in the other chapters.

Chapter 3 reports on the first specific aim, including the characterizing and correction of optical artifacts in a volumetric scintillation detector.

Chapter 4 reports on the second specific aim, including a study of ionization quenching in scintillators and a method for correcting quenching to obtain accurate dose measurements.

Chapter 5 reports on the third specific aim, including the design of a new dual-camera scintillator detector and an evaluation of its usefulness for quality assurance measurements for scanned proton beam delivery systems.

Chapter 6 summarizes the findings of the entire body of research, draws conclusions, and indicates future areas of study growing out of this dissertation.

CHAPTER 2

BACKGROUND

2.1 Proton radiation therapy

In 1930 the cyclotron was developed by E O Lawrence, providing the first reliable, intense source of high-energy protons and other charged particles, a necessary precursor to proton radiation therapy. Proton therapy for cancer treatment was initially proposed by Robert Wilson in 1946 (Wilson, 1946). He pointed out the potential advantage of the dose distribution of high-energy proton beams for cancer treatment, and he proposed practical methods for treatments using proton beams.

The first use of proton therapy in humans was performed in 1958 at the Lawrence Berkeley Laboratory for treatment of the pituitary gland in metastatic breast cancer patients (Tobias *et al.*, 1958). In the decades after these initial treatments, proton therapy programs were initiated at several other institutions. Other institutions providing important early developments in proton therapy include the Gustaf Werner Institute in Uppsala, Sweden; the Harvard Cyclotron Laboratory in Cambridge, MA; the National Institute for Radiological Sciences in Chiba, Japan; and Loma Linda University Medical Center in Loma Linda, CA.

The last twenty years have seen a transition in proton therapy from large research laboratories to smaller hospital-based facilities, coupled with a rapid expansion in the number of proton therapy facilities. This trend continues today, as there are currently 14 operational proton therapy centers in the United States and 12 new centers in development. Approximately 25-30 other proton therapy centers exist throughout the world, primarily in Europe, Japan, China, and Russia.

2.2 Motivation for proton therapy

The motivation for proton therapy lies in the physics of the energy deposition of high-energy proton beams. While a beam of photons traverses the entire patient with exponential attenuation, a proton beam stops at a given depth determined by its initial energy. The

majority of the energy in the proton beam is deposited in the last few centimeters of the proton range, leading to a large dose peak called the Bragg peak, after William Henry Bragg, who discovered this phenomenon (Figure 2.1). The Bragg peak opens the possibility of treating the target volume to a therapeutic dose while sparing regions of healthy tissue that would normally be irradiated using a conventional photon-based treatment modality.

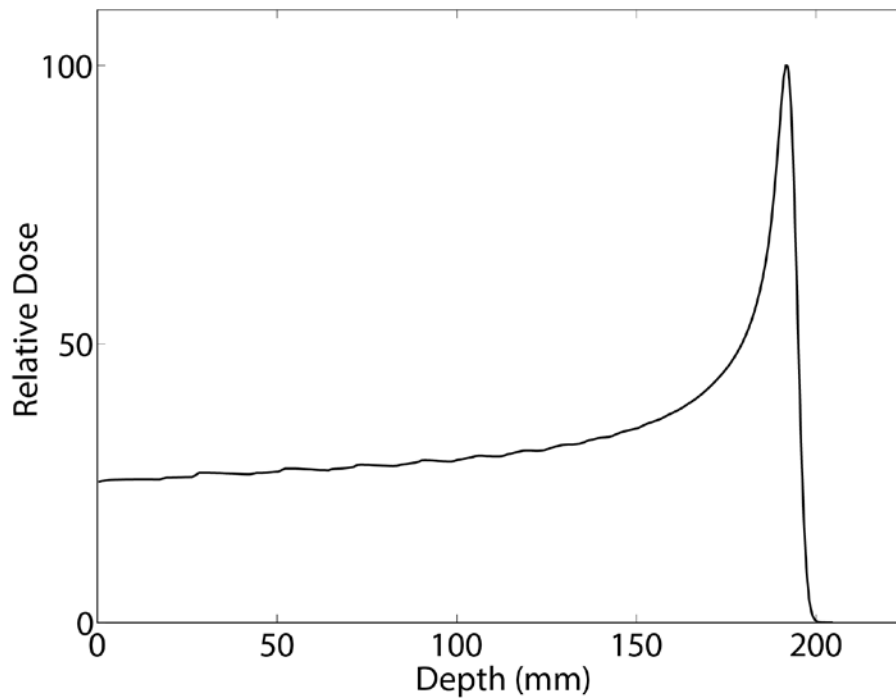


Figure 2.1 The central-axis depth-dose curve of a 161.6 MeV proton beam. The peak near the end of the beam range is known as the Bragg peak.

2.3 Proton interactions with matter

For protons between ~ 0.5 MeV and 250 MeV, the energy range of interest for proton therapy, the atoms in the beam path can either be excited or ionized. The most important parameter characterizing proton energy loss in a material is *electronic collisional stopping power*, S_{col} which is the mean energy lost per unit path length in a material due to collisions with electrons.

$$S_{col} = -\left(\frac{dE}{dx}\right)_{el}$$

A small contribution comes from the *nuclear collisional stopping power*, S_{nuc} which is the mean energy lost per unit path length in a material due to Coulomb collisions with the nuclei, imparting energy to the atoms.

$$S_{nuc} = -\left(\frac{dE}{dx}\right)_{nuc}$$

The stopping power is often divided by the density of the material, ρ , to give the *mass stopping power*. The sum of the electronic and nuclear collisional mass stopping powers for a proton can be calculated using the Bethe formula:

$$\frac{S_{col}}{\rho} + \frac{S_{nuc}}{\rho} = \frac{4\pi \left(N_A Z/A\right) r_0^2 m_0 c^2}{A \beta^2} \left[\ln \left(\frac{2m_0 c^2 \beta^2}{I(1 - \beta^2)} \right) - \beta^2 \right]$$

where m_0 is the proton mass, c is the speed of light, β is the velocity of the proton relative to the speed of light, I is the mean of the ionization and excitation potentials of the atoms in the stopping medium, $(N_A Z/A)$ is the number of electrons per gram of the medium, and r_0 is the classical electron radius, defined as $r_0 = e^2/m_0 c^2$.

Because the mass of a proton is so much larger than the mass of an electron, each ionization event removes only a small amount of energy from the incident proton. The combined effect of many small interactions is a gradual slowing of the proton. The *continuous slowing down approximation*, or CSDA, assumes that energy is lost continuously along the particle track. The *CSDA range* is calculated by integrating the stopping power with respect to energy:

$$R_{CSDA} = \int_0^E -\left(\frac{dE}{dx}\right) dE$$

This gives a close approximation to the average path length of the particles.

2.4 Scanned beam proton therapy

A pristine Bragg peak has a very narrow high-dose region that is too small for the treatment of most tumors. For proton beams to effectively treat a sufficiently large volume, the dose must be spread over a larger area. This is typically done by either broadening the incident proton beam through a scattering and range modulation system or by magnetically scanning beams of several energies across the target volume. The first technique, called “passive scattering proton therapy” was adopted first because of its relative technical simplicity and the straightforward nature of treatment planning with a broad beam.

In recent years technical advances in patient imaging, inverse treatment planning, and beam control systems have facilitated the development of proton therapy treatments with scanned beams. Treatment with scanned beams has several advantages over passive scattering proton therapy, including improved dose distributions, decreased neutron dose to the patient, and no need for patient-specific hardware.

The use of a scanning beam also makes it possible to modulate the dose in the depth direction, leading to an advanced modality called intensity modulated proton therapy (IMPT). IMPT is a conformal radiotherapy modality employing numerous proton pencil beams to form complex treatment fields. The distinctive feature of IMPT is the delivery of multiple inhomogeneous fields from different angles to achieve a homogeneous dose to the target (Lomax *et al.*, 2001). These dose distributions are determined by computer optimization and can be very complex.

2.5 Quality assurance for scanned beam proton therapy

All radiotherapy modalities require a quality assurance (QA) program to ensure that equipment functions properly and treatments are delivered accurately. This includes regular tests of the delivery system as well as measurements of patient treatment fields. ICRU Report

78 (ICRU, 2007) gives recommendations for QA measurements for the delivery system as well as patient-specific QA.

Delivery system QA for a scanned beam proton therapy system should include regular measurements of the beam range and lateral profile for each beam energy. In addition, the function of the scanning magnets should be regularly checked by measuring the position of beams which are scanned away from the central axis.

Patient-specific QA requires measurements of complex 3D dose distributions with high spatial resolution (Pedroni *et al.*, 2005; ICRU, 2007). The time-dependent nature of scanned beam delivery also complicates measurements. Each pencil beam contributes dose along its entire range and lateral extent, so that the dose at any point in a treatment field includes contributions from numerous pencil beams (Sawakuchi *et al.*, 2010). As a result, the entire field must be delivered to measure the dose at any point. Detailed dose measurements may require thousands of measurement points, making it impractical to measure scanned-beam dose distributions using standard single-point detectors. A QA program for scanned proton beams therefore requires the use of higher-dimensional detectors in order to obtain adequate dose measurements in a clinically practical time frame.

2.6 Dosimeters used for scanned proton beam QA

Dose verification for scanned proton beam treatments has been carried out using ionization chambers, scintillating plates and CCDs, and gafchromic films in the past. Because ionization chambers measure the dose at a single point, it is difficult to use them to measure complex 3D treatment fields. To improve measurement efficiency, some investigators have constructed linear and orthogonal arrays of 20 to 30 individual chambers (Karger *et al.*, 1999; Lomax *et al.*, 2004; Coray *et al.*, 2002). 2D arrays consisting of 1020 ionization chambers have become commercially available and are used for IMPT dose verification (Arjomandy *et al.*,

2010; Zhu *et al.*, 2011). However, these devices are limited by the number of chambers in the array, the number of measurement depths, and the chamber spacing. They are also subject to volume averaging effects, decreasing their accuracy in highly inhomogeneous regions. In addition, ionization chambers perturb the radiation beam because they are not water equivalent.

A scintillating plate/CCD system can be used to measure relative 2D distributions with sub-millimeter accuracy (Boon *et al.*, 1998). Such systems are used for proton beam measurements at the Paul Scherrer Institute (Pedroni *et al.*, 2005) and at the Svedberg Laboratory in Uppsala, Sweden (Tilly *et al.*, 2007). However, although scintillating plate/CCD systems increase operational efficiency, they cannot provide 3D measurements.

Films are also widely used to measure 2D dose distributions in water or plastic phantoms. Film dosimetry has well-known limitations, including LET dependency, scanner calibration instability, complex optical density-to-dose calibration protocols, and sensitivity of film response to environmental conditions (Karger *et al.*, 2010). Although strict adherence to scanning and calibration protocols can provide acceptable dose distributions for complex proton treatment fields (Zhu *et al.*, 2011; Kim *et al.*, 2012b), the irradiation and analysis are time consuming and provide dose information at only a few depths.

BANG polymer gels and PRESAGE radiochromic polymer dosimeters have the potential to provide 3D dose distributions for IMPT verification (Zeidan *et al.*, 2010). However, the radiochromic polymer dosimeters are still investigational (Jordan, 2010) and the response of gel dosimeters is sensitive to variability in their preparation methods (Baldock *et al.*, 2010). Both the radiochromic and gel dosimeters have other limitations including LET and energy dependence, lack of reusability, and the need for off-line readout (Karger *et al.*, 2010).

Preliminary studies performed by our research group have demonstrated the high accuracy of a prototype large-volume liquid scintillation detector in measuring the range,

lateral position, and intensity of proton beams (Archambault *et al.*, 2012). The effective pixel size of the detector was 0.3 mm, providing high-resolution images of the scintillation light. After correcting for inverse square losses and attenuation in the scintillator, less than 0.5% deviation in measured light intensity was found at different distances from the camera. In a preliminary test on a four-field box photon beam plan, the dose measured in 96% of the pixels was within 3% or 3 mm to agreement with the treatment plan (Ponisch *et al.*, 2009).

2.7 Scintillation dosimetry

Scintillation dosimetry is a relatively new discipline that shows particular promise for IMPT dosimetry. Plastic scintillators are attractive for dosimetry because of their radiological water equivalence, small size, and low energy dependence (Beddar *et al.*, 1992a, b; Beddar, 2006). Arrays of miniature plastic scintillator detectors have been developed for 2D dosimetry applications (Archambault *et al.*, 2007; Lee *et al.*, 2008; Safai *et al.*, 2004; Guillot *et al.*, 2011). Detectors consisting of scintillating screens coupled to cameras have also been developed for dosimetry of complex fields, including IMPT fields (Boon *et al.*, 1998; Collomb-Patton *et al.*, 2009).

Large 3D scintillation detectors have been developed to evaluate the dose distribution of a radiation source. This technique was initially proposed and developed for brachytherapy eye plaques (Kirov *et al.*, 2005a; Kirov *et al.*, 2005b), and further work by our research group has extended its use for photon beams (Ponisch *et al.*, 2009). Recent work has focused on the development of large-volume liquid scintillation detectors to measure scanned proton beams (Beddar *et al.*, 2009; Archambault *et al.*, 2012).

Liquid scintillator (LS)-based detectors have several attractive features for dosimetric measurements. They exhibit high resolution, dose rate independence, and a linear dose response (Ponisch *et al.*, 2009). A large volume of liquid scintillator can serve as the

measurement medium in addition to the detector, thus eliminating perturbations to the radiation field by the detector. LS measurements are immediate and do not require readout after the dose delivery like other 3D dosimeters. The light emission from the LS occurs within nanoseconds, making it possible to perform repeated measurements very quickly (Beddar *et al.*, 2009). Despite these advantages, scintillators tend to under-respond to protons with high linear energy transfer (LET), and this “quenching” effect has limited their use in proton dosimetry (Birks, 1951; Mouatassim *et al.*, 1995; Smith *et al.*, 1968). However, models have been developed to quantitatively describe this phenomenon (Birks, 1951; Chou, 1952).

2.8 Ionization quenching of scintillation light

Ionization quenching is a known obstacle that needs to be overcome to perform accurate scintillation dosimetry for proton beams. The earliest and most widely used ionization quenching model was developed by Birks (1951). This model is based on the assumption that quenching in scintillators is linearly related to the LET of the ionizing radiation. Chou (1952) proposed the addition of a second-order term, and others have developed variations of the model to expand its utility to ions heavier than protons (Papadopoulos, 1999; Yoshida *et al.*, 2010).

Another quenching model that is relevant to organic scintillators was developed by Michaelian and Menchaca-Roca (1994). This model is based on the assumption that there exists a maximum electron energy deposition density $\rho(r)$ above which the scintillator does not respond linearly, where $\rho(r)$ is a function of the radial distance from the ionization track of a heavy ion. This model has been expanded to incorporate a quantum impact parameter (Cruz-Galindo *et al.*, 2002), and a simplified form has also been developed that exchanges the dependence on $\rho(r)$ for dependence on LET, in analogy to the Birks model (Menchaca-Rocha, 2009).

Most of the quenching models described above are functions of the LET of the radiation. LET is a very difficult quantity to measure, so it is usually calculated using Monte Carlo or analytical methods (Tilly *et al.*, 2005; Sawakuchi *et al.*, 2010; Grassberger *et al.*, 2011). An analytical proton beam LET calculation method was developed by Wilkens and Oelfke (2003), based on the analytical proton beam dose calculation method of Bortfeld (Bortfeld *et al.*, 1996; Bortfeld, 1997). This method provides a dramatic increase in calculation speed with a modest decrease in accuracy of the calculated LET values.

Recent studies have investigated scintillator quenching in mono-energetic proton beams using the first- or second-order Birks quenching models (Torrissi *et al.*, 2000; Kim *et al.*, 2012a). Torrissi *et al.* obtained high measurement accuracy in the depth direction by performing measurements with a thin sheet of polyvinyl toluene plastic scintillator. They found that the second-order term was required to account for non-linear quenching correction factors at high LET values. Although their approach provided high resolution in the depth direction, they did not measure changes in quenching as a function of radial distance from the beam axis. Kim *et al.* used the first-order Birks model to obtain quenching factors for arrays of plastic scintillating fibers. Although their detector had 1-mm lateral resolution, they did not consider radial variation in quenching, and their measurement accuracy was poor. In summary, early work on quenching correction for scintillation dosimetry has shown promise, but the accuracy of quenching correction methods is still below that required for radiotherapy dosimetry.

CHAPTER 3

OPTICAL ARTIFACT CHARACTERIZATION AND CORRECTION IN VOLUMETRIC SCINTILLATION DOSIMETRY

This chapter is based upon material that was published in Physics in Medicine and Biology in January 2014 by the author of this dissertation [Robertson D, Hui C, Archambault L, Mohan R and Beddar S 2014 Optical artifact characterization and correction in volumetric scintillation dosimetry Phys. Med. Biol. 59 23-42]. Upon transfer of copyright, IOP Publishing grants back to authors the right to include the article in research theses or dissertations.

3.1 Introduction

The goal of volumetric scintillation dosimetry is to evaluate the dose distribution of a radiation source by measuring the light emission from a scintillating volume. It was initially proposed and developed for brachytherapy eye plaques (Kirov *et al.*, 2005), and further work has extended its use to photon beams (Ponisch *et al.*, 2009) and proton beams (Fukushima *et al.*, 2006). Recent work has focused on the application of a large-volume liquid scintillator (LS) detector for quality assurance measurements of scanned proton beams (Beddar *et al.*, 2009; Archambault *et al.*, 2012). The detection system used in this study consists of a cubic tank containing a LS solution and a charge-coupled device (CCD) camera for obtaining images of the light distribution in the tank.

In order to accurately measure the scintillation light distribution, one must correct for various optical artifacts that arise as the light propagates from the scintillating centres to the detector and as the detector measures the incident light. Although prior studies have acknowledged the presence of these artifacts and taken initial steps to correct them (Archambault *et al.*, 2012; Ponisch *et al.*, 2009), a systematic evaluation of the impact of optical artifacts and the methods for correcting them has not been performed. The purpose of this study, therefore, was to examine the various sources of optical artifacts present in volumetric scintillation dosimetry and then to develop correction methods to remove or mitigate the effects of those artifacts so that meaningful dosimetric measurements could be obtained. The

optical artifacts will be divided into those produced in the scintillator and its container, those associated with the optical train of the camera, and those related to the CCD chip (see Table 3.1).

Table 3.1 Optical artifacts in a volumetric scintillation dosimetry system.

Artifact source	Physical phenomenon	Effect
Light propagation in the scintillator and tank	Photon scattering	Blurring of light signal
	Refraction	Changes in effective pixel size and intensity
	Perspective	Changes in effective pixel size with depth
Optical train	Vignetting	Decreased brightness at image periphery
	Lens distortion	Radial variation in pixel size and location
	Lens point spread function	Blurring of light signal
CCD chip	Stray radiation	Hot pixels and streaks
	Background noise	Measurement uncertainty and pixel value offset

3.1.1 Scintillator tank artifacts

Interactions of scintillation light within the scintillator tank change the light distribution that is measured by the camera and therefore constitute the first source of error to be dealt with by any correction algorithm. Scintillation light undergoes scattering as it travels through the scintillator. In addition, it can be reflected at the tank wall, and its path can be altered by refraction through the window-air interface. Each of these interactions changes the light distribution that is measured by the camera.

Although scintillators are designed to be transparent to their own light emissions, scintillation photons experience Rayleigh scattering and additional scattering due to absorption and re-emission as they pass through the scintillator. The result of this scattering is a blurring of the measured light distribution that is independent of the camera's focus settings. This blurring may be particularly problematic when measuring steep dose gradients and highly

heterogeneous radiation fields such as proton Bragg peaks, where blurring leads to a broadening of the Bragg peak and a decrease in its height.

Previous work in volumetric scintillation dosimetry has shown that blurring due to photon scatter can be corrected by deconvolving a point spread function (PSF) from the images (Kirov *et al.*, 2005; Ponisch *et al.*, 2009). These studies obtained the PSF by assuming a functional form of the PSF and then fitting the parameters of the function based on a comparison between the measured and expected scintillation light projections. While this approach provided reasonable results, the PSF was not derived from any measurement or calculation.

Refraction changes the path of light as it travels from one medium to another. Refraction at the interface between the LS solution and the tank window is minimal because the materials' indexes of refraction are similar. However, refraction at the window-air interface is significant, leading to a shift in the expected positions of individual pixels and an increase in the apparent size of objects or light sources within the tank.

Another challenge associated with measuring light from a large volume with a lens-camera system is perspective, the decrease in an object's apparent size with its increasing distance from the lens. Telecentric lenses can be used to acquire images without perspective, but these lenses can only acquire light from an area as large as the diameter of the primary lens. In the case of a large detector such as the one in this study, the weight and cost of a telecentric lens large enough to measure the entire detector would be substantial. If non-telecentric optics are used for quantitative measurements, the size of objects must be scaled by their distance from the lens.

3.1.2 Optical train artifacts

The scintillation light from the detector is collected and transmitted to the CCD chip by a compound optical lens, which introduces additional artifacts, including vignetting, lens distortion, and blurring due to the point spread function of the lens.

Vignetting is the decrease in a camera's measurement efficiency with distance from the image centre, and is typically classified as mechanical, optical, or natural. Mechanical and optical vignetting are caused by the physical obstruction of light in the optical train and can be prevented by appropriate selection of the lens settings. Natural vignetting is caused by the divergence of light as it travels from the lens to the image sensor. The degree of natural vignetting varies with the lens and camera design, but it is present in most cameras and must be corrected for accurate quantitative light measurement over the entire image.

Lens distortion is the nonlinear mapping of radial distance in image space that results from imperfect lens design. It is typically either 'barrel distortion,' in which the image is magnified at the centre relative to the edges, or 'pincushion distortion,' in which the image is magnified at the edges relative to the centre. Modern scientific lenses are designed to minimize lens distortion, but no lens is perfect.

In addition to the blurring caused by light scattering in the scintillating medium, the lens itself also introduces blurring to the optical system. As a result, the blurring in the scintillator detector is a combination of two PSFs, one from scattering in the scintillator and one from the lens.

3.1.3 CCD artifacts

The CCD chip is the final source of error in the image acquisition chain. CCD chips are subject to various sources of noise, including photon noise, dark noise, and readout noise. An additional source of noise is stray radiation, including gamma rays and secondary neutrons,

protons, and nuclear fragments. The CCD can be exposed to these stray particles, which may deposit their energy within individual pixels, leading to transient spikes or streaks in the images.

3.2 Materials and methods

The detection system used in this study was described previously (Archambault *et al.*, 2012). Here, we will describe the details of the system that are relevant for consideration of the optical artifacts. We will then describe our methods for characterizing and correcting the optical artifacts of interest. The correction methods will be addressed in the order in which they are applied in the image processing chain. The image processing workflow (Figure 3.1) proceeds in reverse order of the photon path, beginning at the CCD and concluding with refraction and blurring in the scintillator tank. With the exception of the Monte Carlo dose calculations, all computations and analysis were performed using MATLAB version 2012b (The MathWorks, Natick, MA).

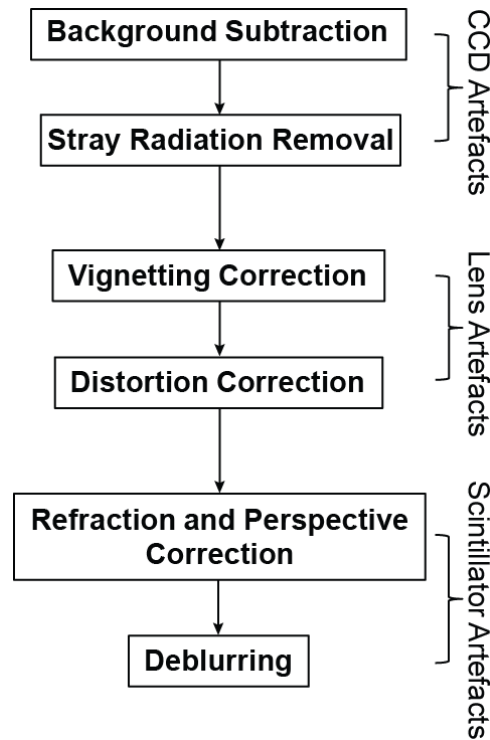


Figure 3.1 Workflow of the optical artifact correction process.

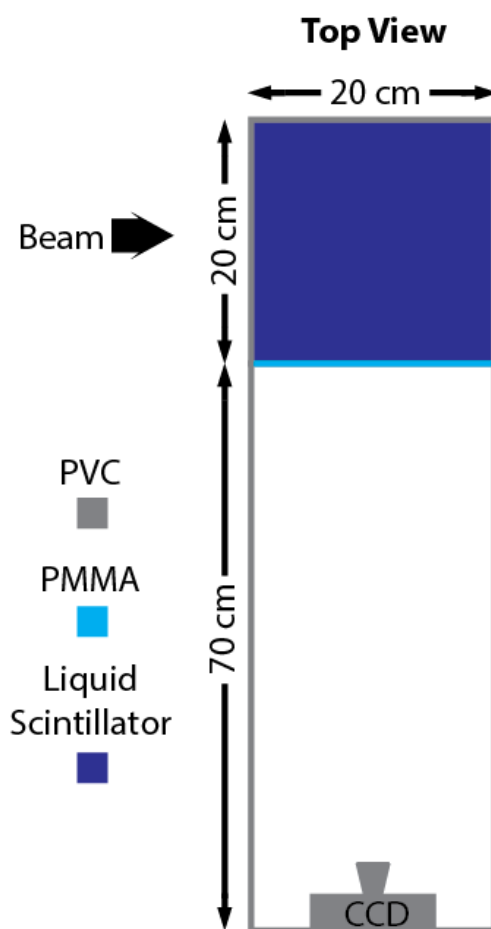


Figure 3.2 Liquid scintillator detector system.

3.2.1 *Liquid scintillator detector*

The detection system used in this study consists of a cubic tank containing a volume of LS solution, with a CCD camera for measuring the light distribution in the tank (Figure 3.2). The LS solution serves as the detection medium and also as the attenuating phantom. The LS solution used in this study is BC-531 (Saint-Gobain Crystals, Hiram, OH), which consists of scintillating molecules in a mixed solvent of linear alkyl benzene and 1,2,4-trimethylbenzene. The density of the scintillator is 0.87 g cm^{-3} , and its refractive index is 1.47. Its light emission peak is centred at 425 nm, its light output is 59% of the output of anthracene, and the decay time of the principal scintillation light emission is 3.5 ns. A scintillator-to-water proton range

scaling factor of 0.902 was calculated for BC-531 using the Monte Carlo package MCNPX version 2.7.0 (Los Alamos National Laboratory, Los Alamos, CA).

The tank walls are made of opaque polyvinyl chloride (PVC), except for one wall, which is made of clear polymethyl methacrylate (PMMA). This PMMA wall serves as a window through which the camera views the light emission from the scintillator. The tank and camera are connected by a light-tight housing, also constructed of PVC, which isolates the detector optics from ambient light. The tank dimensions are $20 \times 20 \times 20 \text{ cm}^3$, and the camera is located 70 cm away from the tank. To reduce reflections from the grey PVC tank walls, the interior walls of the tank were covered with a lining of black polymer. The surface of this polymer was roughened by hand with sandpaper to further reduce reflections. Reflections at the LS-air interface at the top of the tank were avoided by filling the tank until the LS-air interface was above the region viewed by the camera.

The CCD camera used in this study is the Luca^{EM} S 658M (Andor Technology, Belfast, Northern Ireland). The CCD resolution is 658×496 pixels, and the physical pixel size is $10 \text{ }\mu\text{m}$. The camera digitizes optical signals at 14 bits and is capable of measuring 37 full frames per second. The chip is cooled to -20°C via an on-board thermoelectric cooling system. An objective lens (JML Optical Industries, Rochester, NY) with an effective focal length of 25 mm was fitted to the camera, and the focus and aperture were set to 0.82 m and $f/5.6$, respectively, resulting in a focal depth of 11.6 cm centred on the scintillator tank.

3.2.2 Artifact analysis and correction methods

3.2.2.1 CCD artifacts

CCD noise: Dark frame images were acquired to measure the dark current and noise of the CCD camera. Dark frame images were obtained by taking repeated images with the lens cover attached. Because the temperature of the CCD chip affects the dark current and noise, all

images in this study were obtained after the CCD temperature had stabilized at its set point of -20° C. To evaluate the effect of exposure time on the dark noise, we took a series of dark frames with exposure times ranging from 4.7×10^{-4} s (the minimum exposure time available on the camera) to 100 s. The average pixel value and the standard deviation of the pixel values over the entire image were calculated as a function of exposure time. In practice, the offset due to dark current is subtracted during background subtraction. However, the noise in the dark current remains along with the other CCD noise sources.

Stray radiation: The transient spikes and streaks in the CCD images caused by stray radiation were removed by applying a spatial median filter. While a temporal median filter is preferred for spatial accuracy, temporal filters require at least three repeated acquisitions of any given field. To avoid this repetition, we applied a spatial median filter to the 3×3 region surrounding each pixel.

3.2.2.2 Lens artifacts.

Vignetting: Natural vignetting is approximated by the ‘ $\cos^4(\theta)$ law of illumination’ (Ray, 1994), which states that the degree of vignetting is proportional to $\cos^4(\theta)$, where θ is the angle between the optical axis and the ray from the exit pupil of the lens to the measurement point on the imaging sensor (Figure 3.3). The vignetting value for a given pixel (i,j) can therefore be calculated by the equation

$$V_{i,j} = \cos^4(\theta_{i,j}) = \frac{a^4}{(a^2 + d_{i,j}^2)^2} \quad (3.1)$$

Where a is the distance from the exit pupil to the principal point (the point where the optical axis meets the image sensor), and $d_{i,j}$ is the distance from the principal point to pixel (i,j) . Depending on the lens design, the distance a may differ significantly from the focal length. In the event that the parameter a is not known, it can be approximated by the ratio of the object-space focal distance to the measured object-space pixel size at the focal plane. The $\cos^4(\theta)$ rule

is only strictly valid for thin lenses, and some commercially available lenses diverge significantly from this behaviour (Goldman, 2010). However, the $\cos^4(\theta)$ rule provides a simple analytical model of vignetting that is effective in many cases. Those desiring a more accurate vignetting correction can use alternate vignetting models, such as those proposed by Litvinov and Schechner (2005) or Goldman (2010).

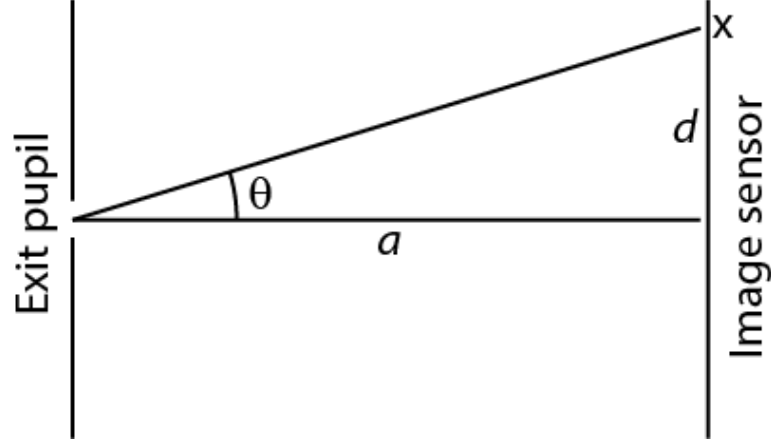


Figure 3.3 The angle θ used in the ' $\cos^4\theta$ rule' for camera vignetting is defined as the angle between the camera's optical axis and the ray from the exit pupil of the lens to measurement point x on the image sensor.

The vignetting in our lens-camera system was measured by analysing flat field images. These were acquired by attaching a diffusing filter to the front of the lens and acquiring images of the centre of a flat screen computer monitor at close range. Several flat field measurements with different camera orientations were averaged together to reduce the impact of any non-uniformities in the monitor output. The resulting flat field was fit to a $\cos^4(\theta)$ function using least squares optimization. The pixel size of the camera was known, allowing $d_{i,j}$ to be calculated precisely. Because the distance a was not known for the lens used in this study, the fit of the $\cos^4(\theta)$ function consisted of fitting the parameter a of equation 3.1. The vignetting in the detector system was corrected by scaling each image by the $\cos^4(\theta)$ function determined by the fit.

Lens distortion: One approach to solving the lens distortion problem is to calibrate a lens and map its distortion modes. Camera calibration methods using vanishing points and vanishing lines to identify the camera focal length have been extensively developed (Caprile and Torre, 1990; Wang and Tsai, 1990), and calibration techniques for determining lens distortion have been developed for machine vision applications (Tsai, 1992; Zhang, 1999). In this study, lens distortions were measured and corrected using the Camera Calibration Toolbox for Matlab (Bouguet, 2010), which is an implementation of the previously cited camera calibration techniques. It was used to develop a model of the camera's intrinsic and extrinsic parameters, including focal length, principal point, and lens distortions, based on multiple images of a checkerboard pattern at different orientations. The lens distortion was modelled using the second order symmetric radial distortion model used by Zhang (1999). The calibrated distortion model then was used to restore the rectilinearity of each image acquired with the detector.

Lens PSF: In the simplifying case of a perfect (aberration-free) lens, the PSF is produced by the diffraction of light from the source as it travels through the lens aperture, and is equivalent to the Fraunhofer diffraction pattern of the aperture. Real lenses diverge from this ideal behaviour, as the PSF is broadened by imperfections in the optical system.

The point spread function of a lens with a fixed focal length can be described as a function of six variables, including the wavelength of the light, the image coordinates (x and y), the lens aperture, the distance from the lens to the object (z), and the back focal distance (Shih *et al.*, 2012). In the case of the detector described here, the light wavelength, lens aperture, and back focal distance are fixed. This leaves the lens-object distance and the image coordinates as the variable parameters of the PSF. Because the lens-object distance is constrained to the inside of the scintillator tank, the lens PSF is essentially a three-dimensional function with a unique value for every point in space within the scintillator tank.

The PSF of the entire system consists of the convolution of the lens PSF and the PSF due to light scatter within the scintillator:

$$PSF_{sys}(x, y, z) = PSF_{scatter}(x, y, z) * PSF_{lens}(x, y, z) \quad (3.2)$$

While PSF_{lens} is technically a function of the three-dimensional location inside the scintillator tank, in practice its variation may be small enough over the region of interest that an invariant PSF_{lens} could be assumed as a first-order approximation. Because of the expected small variation and the difficulty of measuring the PSF_{lens} at multiple locations, we assumed an invariant PSF_{lens} in this study. We leave as future work the determination of the spatial variation of PSF_{lens} .

PSF_{lens} was measured using the method described in ISO standard 12233 for measuring the resolution of photographic cameras (ISO, 2000). This process involves three steps:

1. Photograph a slanted edge formed by the interface between black and white regions.
2. Measure the edge-spread function (ESF) perpendicular to the slanted line. Repeating this measurement at multiple locations along the slanted line allows the ESF to be determined with a resolution greater than the camera resolution.
3. Take the derivative of the ESF to obtain the line-spread function, which is the one-dimensional equivalent of the PSF.

The test pattern was formed by joining a black strip of plastic to a white strip along a carefully machined straight edge. This pattern provided the required ESF and was chemically compatible with the scintillator solution. This test pattern was affixed to a rigid surface and viewed at an angle with the camera to produce the requisite slanted edge. The measurement of PSF_{lens} in air was compared to the measurement of PSF_{sys} performed in the scintillator tank, as described in section 3.2.2.3.

3.2.2.3 Scintillator tank artifacts

Refraction and perspective: Refraction and image perspective both affect the location and apparent size of objects and light sources within the tank. Because of this interconnection, refraction and perspective are corrected simultaneously. We developed a first-order correction for refraction and perspective based on the simplifying assumption that our camera system is a pin-hole camera. As shown in Figure 3.4a, any photon created along the line \overline{MC} is projected onto the point X in the camera focal plane. Therefore, the apparent size and location of an object depends on its distance away from the focal plane. The presence of the scintillator solution creates an additional change in the object's apparent size and location. As shown in Figure 3.4b, refraction changes the direction of the photon track and thus changes the observed position of the photon origin. In addition to change of location, the change in apparent pixel size causes a change in the pixel value in the CCD image.

Refraction and perspective are corrected analytically based on the pin-hole camera assumption. The index of refraction of the LS is 1.47 and that of the acrylic tank is 1.49. Since refraction at the LS-window interface is very small, only refraction at the window-air interface is considered in the correction. Considering that most of the photons are created along the proton track, the goal of the correction is to translate the image from the focal plane to the plane of the proton track.

First, the coordinate of each pixel in the camera plane is mapped to the proton track plane using Snell's law and trigonometric identities. Based on the coordinate translation map, the ratio of the pixel area at the proton track plane to that at the focal plane is calculated for each pixel. The pixel value at the proton track plane is then normalized by dividing each pixel value by its corresponding area ratio. For example, if the area ratio is smaller than 1, the normalized pixel value will be higher than the measured value. The normalized pixel values with the

translated coordinates are then used to interpolate to the final pixel value at the proton track plane.

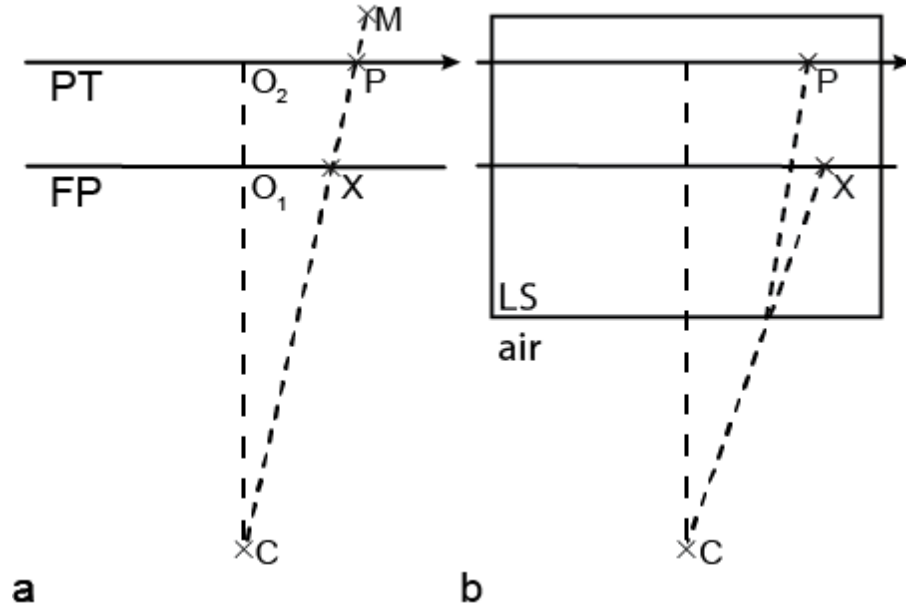


Figure 3.4 Consider a pinhole camera located at point C . a) The camera is focused on the focal plane (FP) where $\overline{O_1C}$ is the focal length. Photons originating from line \overline{MC} will be translated to the point X in the FP in the CCD image. For example, point P of the proton track (PT) will be mapped to point X at the FP. The apparent location of P will be shortened from $\overline{O_2P}$ to $\overline{O_1X}$ in the FP. b) In the presence of the liquid scintillator (LS), the photon beam is bent at the LS-air junction, causing another displacement of apparent location to a different point at the FP. The correction algorithm calculates the mapping from X back to P . In addition, it corrects the pixel values altered by the change in apparent pixel size.

Photon scatter: The final step of our artifact correction is to address photon scatter in the scintillator. We adapted the method described in section 3.2.2.2 to measure PSF_{sys} for the scintillation detector. The test pattern was placed in the scintillator tank, and the light source for the photograph was produced by exciting the scintillator with an ultraviolet lamp (F15T8/BLB, General Electric Lighting) with a 368-nm emission peak. This ensured that the wavelength of light used for the measurement was the same as that of the light produced during LS irradiation. The PSF_{sys} measurement was repeated with the test pattern placed at a

distance of 3 cm, 10 cm, and 16 cm from the tank window in order to evaluate the relationship between scatter and the distance travelled through the scintillator.

The low-intensity tail of the measured PSF was fit to an exponential function. This preserved the shape of the PSF and prevented the noise in its low-intensity tail from propagating to the images during blurring correction. Blurring in the detector was corrected by deconvolving the measured PSF from the detector images using the Lucy-Richardson deconvolution algorithm (Biggs and Andrews, 1997).

3.2.3 Artifact correction evaluation methods

For each source of error, our goal was to describe the magnitude of error it caused and the effectiveness of our correction method for mitigating it. Thereafter, we used gamma analysis to identify the correction steps that played the greatest role in restoring the images to the original dose distributions.

Proton pencil beams of four energies (85.6, 100.9, 144.9, and 161.6 MeV) were used for in-depth testing of the optical artifact corrections. Depth-light profiles were plotted for qualitative comparison of the measured and calculated distributions. The overall effectiveness of the optical artifact corrections was evaluated by comparing raw and corrected CCD measurements with Monte Carlo dose calculations.

Two-dimensional gamma analysis (Low *et al.*, 1998) was performed to quantify the agreement between the CCD images and the corresponding projections of the Monte Carlo dose distributions. The analysis included all pixels in which the reference distribution was at least 5% of the maximum value. This analysis was performed with the uncorrected and corrected images and with each one of the corrections left out to show its contribution to the overall correction process.

Gamma analysis was also performed on the corrected images with the analysis parameters varying from 1% to 3% dose difference and from 1 mm to 3 mm distance to agreement. Beginning at the commonly used gamma analysis criteria of 3% dose difference and 3 mm distance to agreement, we decreased both of these parameters until the passing rate for at least one of the beam energies dipped below 95%, which we set as the limit for ‘acceptable agreement’ between the measured and calculated distributions.

While it is common practice to use a percentage of the maximum dose as the dose difference criterion for gamma analysis, we elected to use a percentage of the local dose at each pixel as the dose difference criterion. We consider this to be appropriate for this study because the maximum dose in a proton Bragg peak is much higher than the average dose in the region, and the use of a percentage of the maximum dose would be too generous of a dose difference criterion, limiting the utility of gamma analysis for comparison of dose distributions.

3.2.3.1 Proton beam measurements

Proton beam measurements with the scintillator detector were carried out at the MD Anderson Cancer Center Proton Therapy Center-Houston on the scanning beam gantry. The detector was aligned isocentrically on the treatment couch, and mono-energetic proton pencil beams were directed into the scintillator tank perpendicular to the camera axis at a depth of 10 cm from the tank window. Pencil beams were also delivered at depths of 5 cm and 15 cm from the tank window in order to evaluate the variation in light scatter with distance travelled through the scintillator. The experimental setup is shown in Figure 3.5. Nominal proton beams of the four energies named above were delivered and measured separately. A total of 220 monitor units, as described in Gillin *et al.* (2010), was delivered for each beam energy. The CCD camera acquired images at 2 frames per second, so that each proton beam was delivered over the course of 2 images.

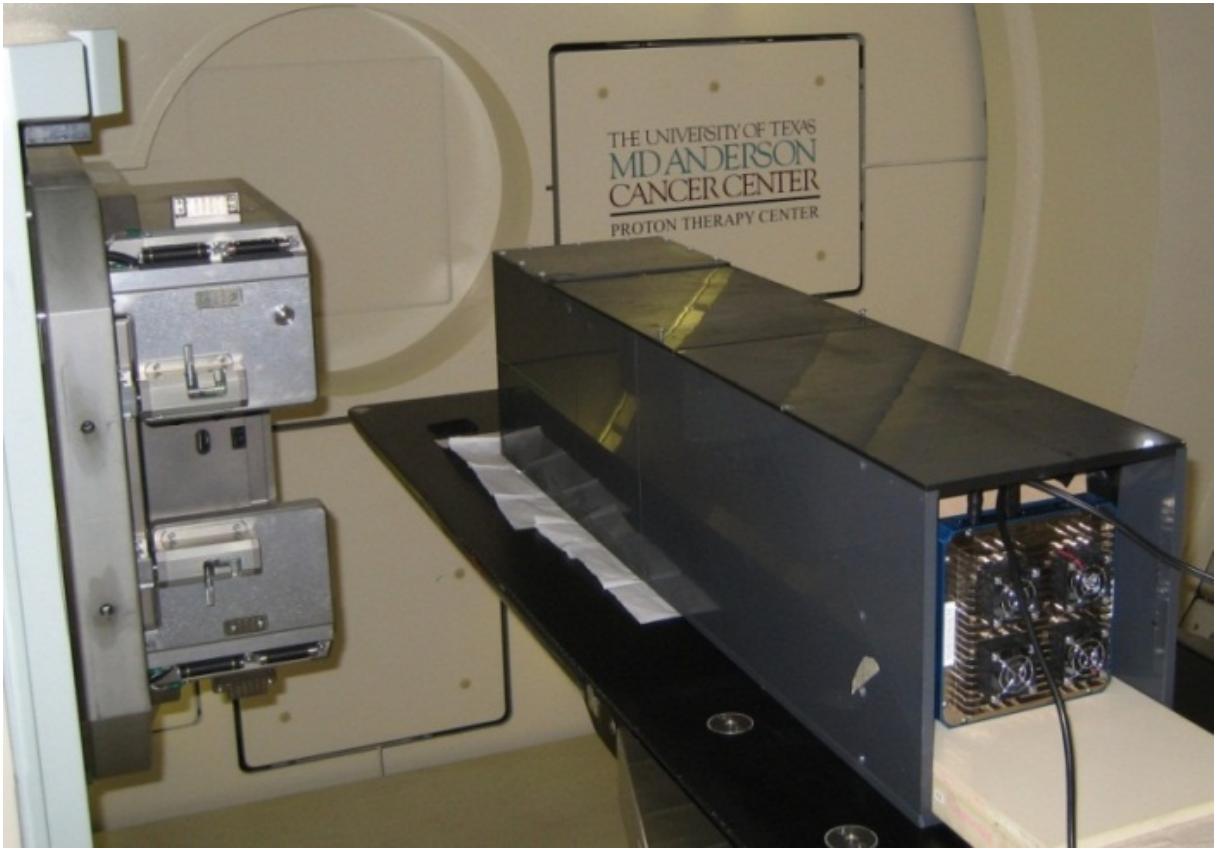


Figure 3.5 Experimental setup for proton beam measurements with the scintillator detector.

3.2.3.2 Monte Carlo calculations

Three-dimensional (3D) dose distributions were calculated for the beam energies named above using the Monte Carlo radiation transport code MCNPX, version 2.7d (Waters *et al.*, 2002) with validated phase space models of the specific scanning beam nozzle being used (Sawakuchi *et al.*, 2010). The voxel size was set to 1 mm perpendicular to the beam direction, and it varied from 1 mm to 0.1 mm in the beam direction, with higher resolution in the steep-dose-gradient region around the Bragg peak.

Scintillators exhibit a non-linear response to ionizing radiation with varying linear energy transfer, a phenomenon called ionization quenching. This phenomenon causes an under-response of the scintillator in the Bragg peak because of the steep increase in linear energy transfer in the Bragg peak region. To account for this effect in the comparison between the

Monte Carlo and CCD data, we applied a quenching model to the Monte Carlo dose data to obtain the scintillating radiation output. The parameters for this model were determined in a previous study by our group for the same detector configuration (Robertson *et al.*, 2013).

3.3 Results

We will first describe the magnitudes of the individual sources of error and their correction methods. Following this, we will give the results of the gamma analysis to identify the correction steps that played the greatest role in restoring the images to the original dose distributions.

3.3.1 CCD artifacts

CCD noise: The dark current of the CCD camera was evaluated by calculating the mean pixel value and standard deviation over the entire frame for a range of exposure times (Figure 3.6). As expected, the dark noise increased linearly with time. This is illustrated by a linear fit to the data, with an R^2 value of 0.9992. The baseline dark signal pixel value for the CCD is 510. The dark current offset is corrected during background subtraction.

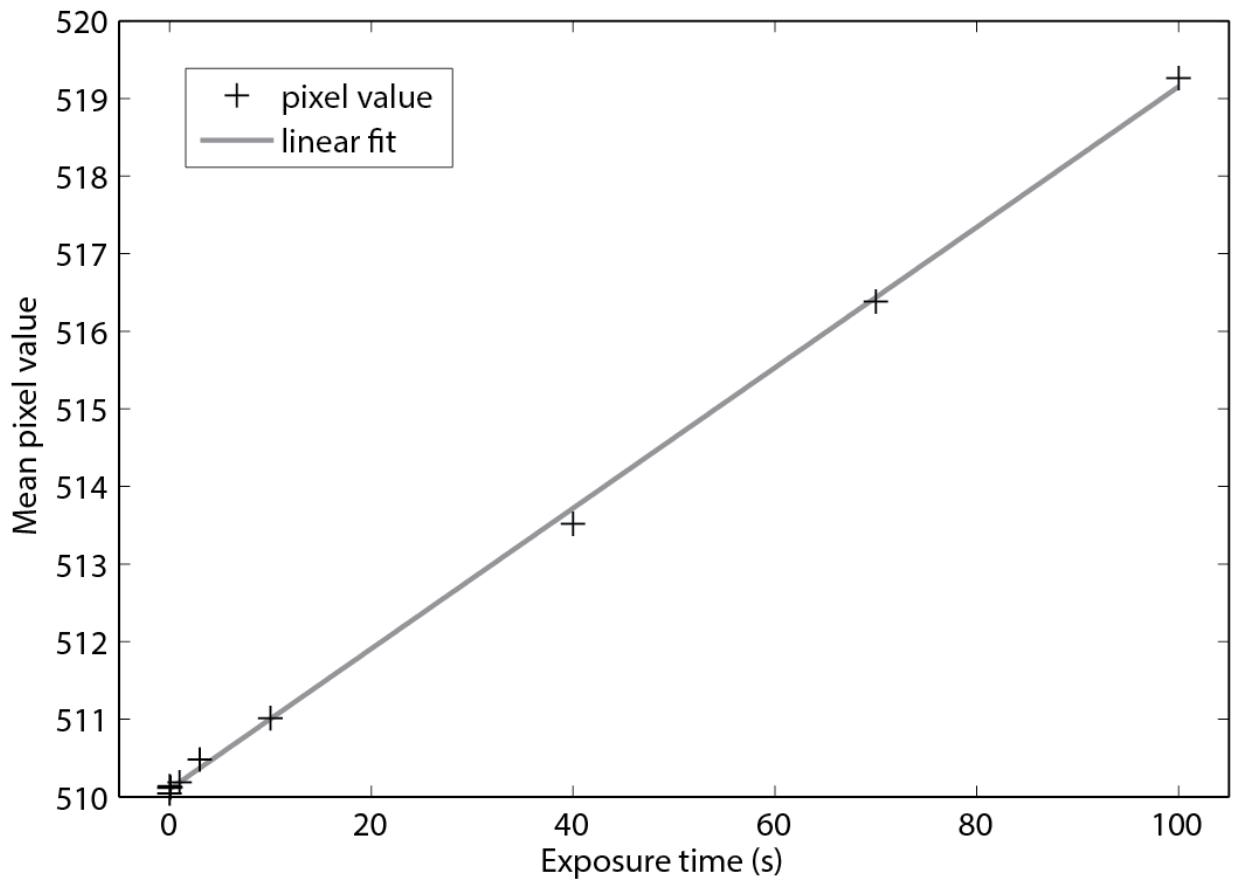


Figure 3.6 The mean pixel value of the CCD for dark frame images of various exposure lengths.

Stray radiation: The spatial median filter effectively removed single-pixel spikes caused by stray radiation (Figure 3.7). The mean number of transient spikes and streaks in the test images decreased from 3 to 0 after the median filter was applied. The median filter did not significantly affect the shape of the underlying light distribution.

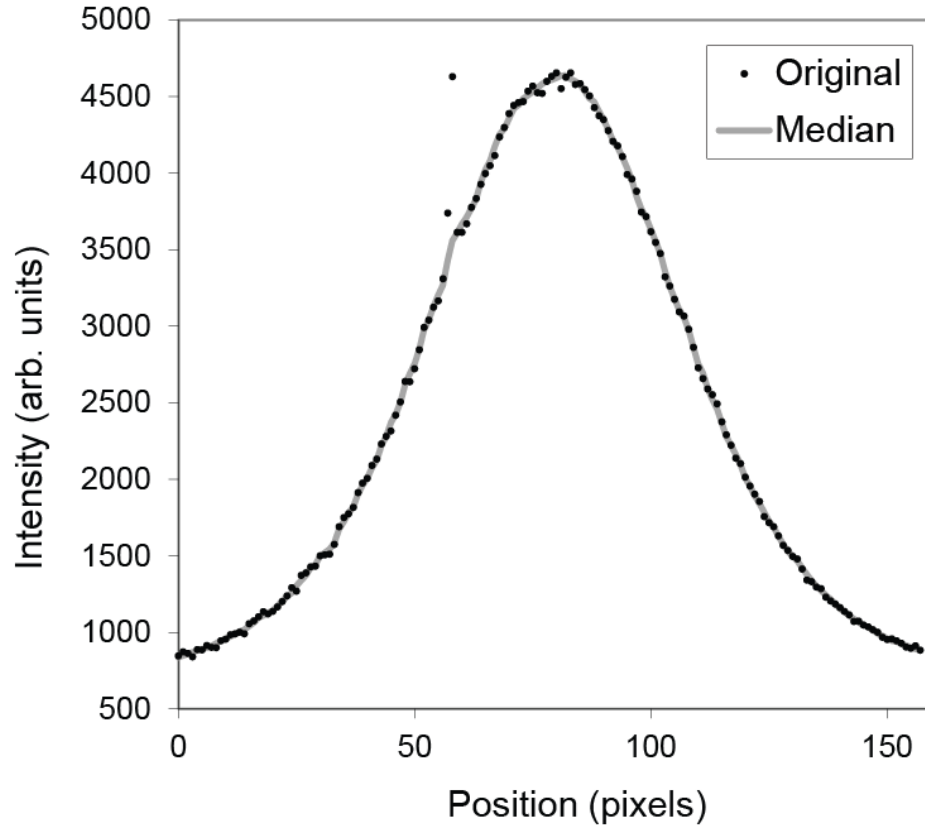


Figure 3.7 The lateral profile of a 100.9-MeV proton pencil beam before (black) and after (grey) application of a 3x3 spatial median filter. The median filter effectively removed the transient spike caused by stray radiation incident on the CCD chip without affecting the underlying light distribution.

3.3.2 Lens artifacts

Vignetting: The $\cos^4(\theta)$ vignetting model provided a good approximation to the measured vignetting behaviour of the camera (Figure 3.8). The fit to equation 3.1 yielded a value of $a = 26.5$ mm, which matches well with the lens focal length of 25 mm and the approximation of a based on object-space parameters, which was 26.9 mm. While the $\cos^4(\theta)$ model did not perfectly match the measured signal falloff, the agreement is considered sufficient for the purposes of this study. The under-response due to vignetting measured for this detector was as great as 4% at the corners of the image, with 7.8% of all pixels under-responding by 3% or more. After the vignetting correction was applied, 99.8% of pixels in the flat field image were within 1% of the pixel value at the centre of the image.

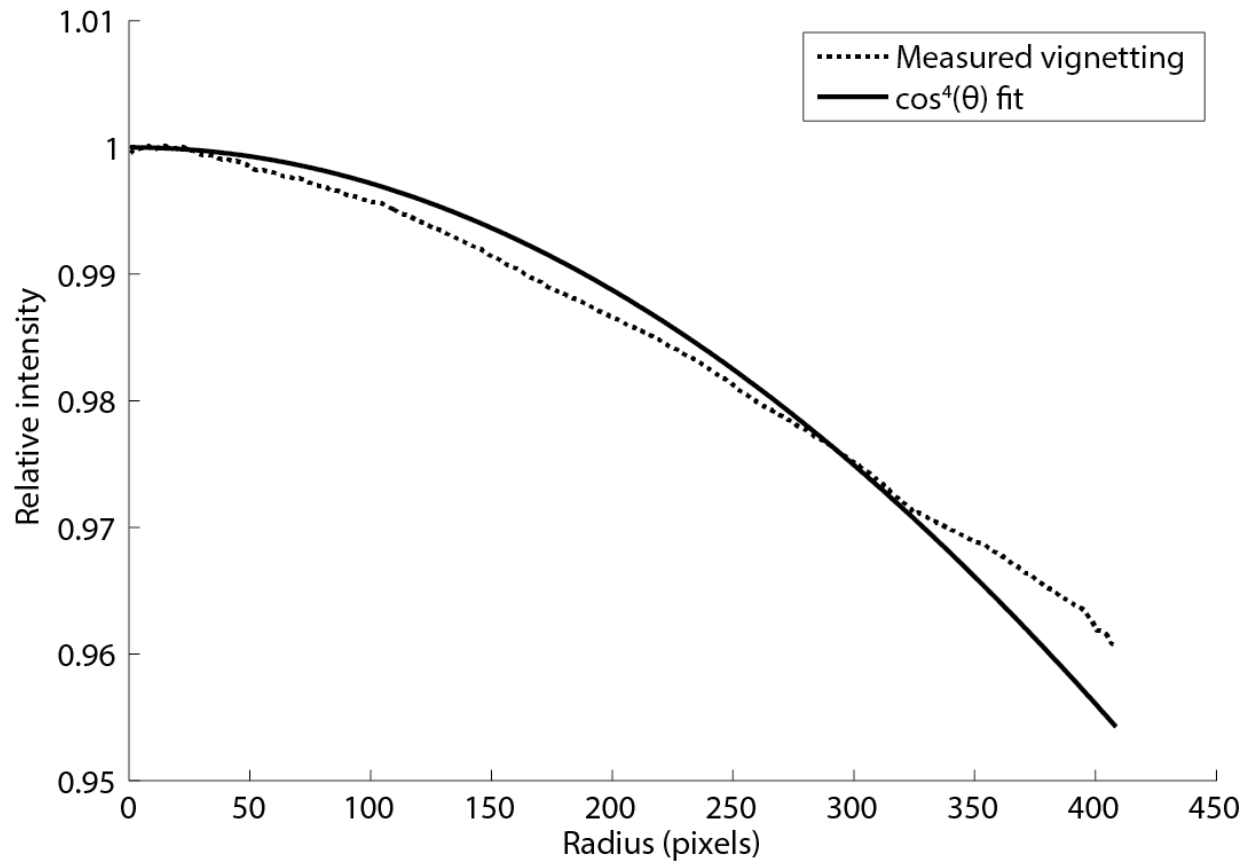


Figure 3.8 The measured vignetting as a function of distance from the lens centre (dashed line) is compared to the $\cos^4(\theta)$ function (solid line) used to model the vignetting.

Lens distortion: As expected, the lens distortion model obtained from the calibration process showed very little distortion in the centre of the field of view. Pixels at the edges of the field of view could be displaced by as much as 2 pixels, which corresponds to a measurement error of 0.6 mm (Figure 3.9). The small magnitude of these distortions illustrates the quality and appropriateness of the lens selected for this detector.

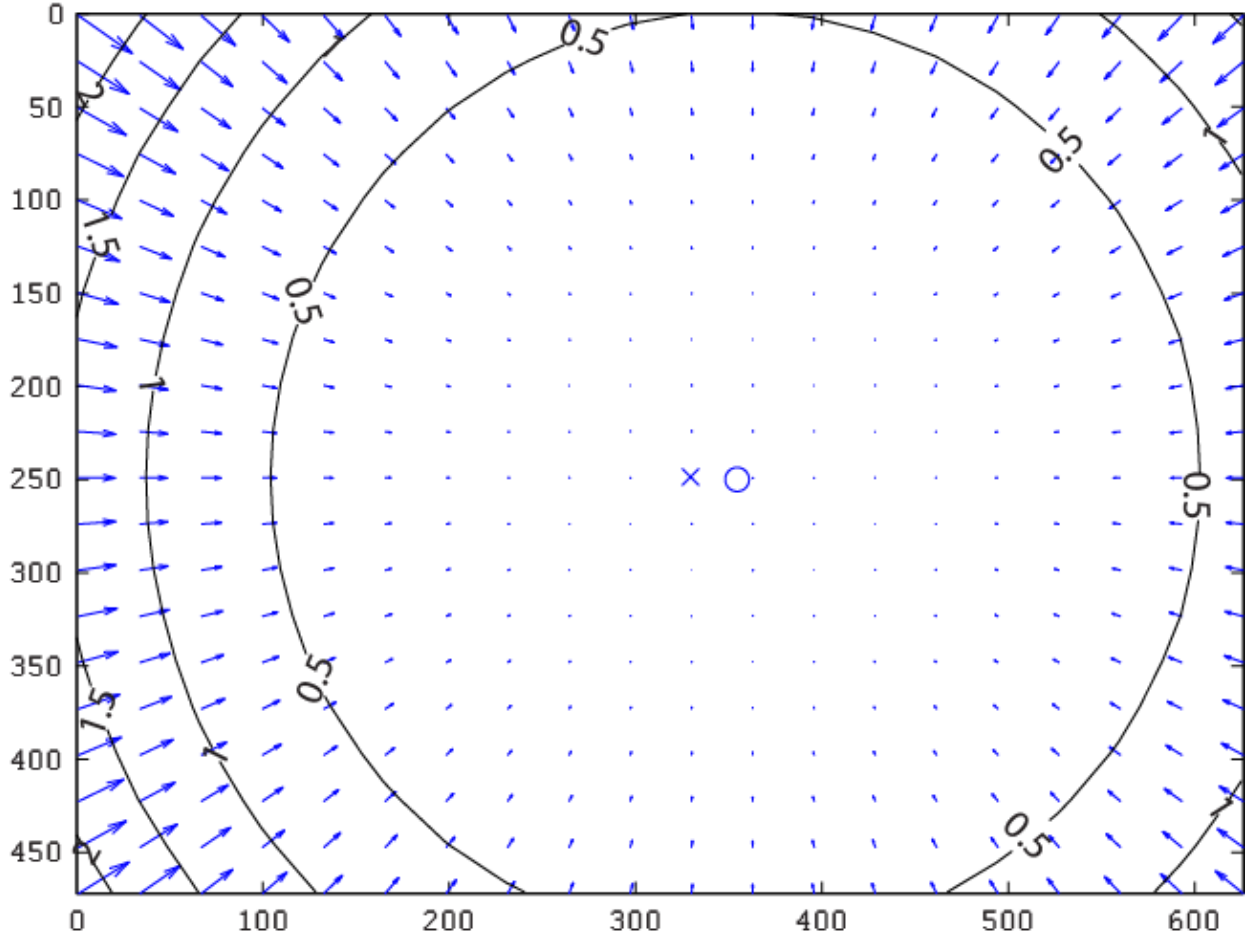


Figure 3.9 The lens distortion model of the CCD camera. The direction and magnitude of the arrows indicate the direction and relative magnitude of the pixel position corrections. The contour plot indicates the magnitude of pixel position corrections in units of pixels. The 'x' indicates the image centre, and the 'o' marks the principal point of the camera.

Lens PSF: The PSF_{lens} measurement results are described in conjunction with the PSF_{sys} measurement results in section 3.3.2.

3.3.3 Scintillator tank artifacts.

Refraction and perspective: The average increase in apparent pixel size due to refraction was 4.1% at the focal plane. The expansion of pixel size caused a relative decrease in pixel count. The apparent pixel count reduction was 7.7% at the image centre and 7.8% in the corners. Both of these effects were corrected. Since our proton track was aligned with the focal plane, no additional step was needed to refocus the track to a different plane.

Photon scatter: PSF_{sys} was found to be a sharp peak with very steep fall-off, dropping to 0.015% within 10 pixels from the centre. At a distance of 8 pixels from the centre, the noise contribution was significant enough that, while the PSF continued to decrease on average, it no longer decreased monotonically. In order to extend the range of the measured PSF beyond 8 pixels, the low-intensity tail was fit to a decreasing exponential function. This allowed the measured PSF to be extrapolated to a distance of 64 pixels from the centre.

To our surprise, there was no substantial difference between the PSF_{sys} measurements performed at different depths in the scintillator. In addition, the measured PSF_{lens} was equivalent to the measured PSF_{sys} (Figure 3.10). This suggests that PSF_{lens} is the primary contributor to PSF_{sys} in our detector, with $PSF_{scatter}$ making a negligible contribution. The invariance of PSF_{sys} with depth in the scintillator tank is confirmed by comparison of the lateral profiles of proton pencil beams delivered at depths of 5, 10, and 15 cm from the tank window. After correction for perspective, attenuation, and inverse-square intensity falloff, there was no substantial difference between the profiles (Figure 3.11).

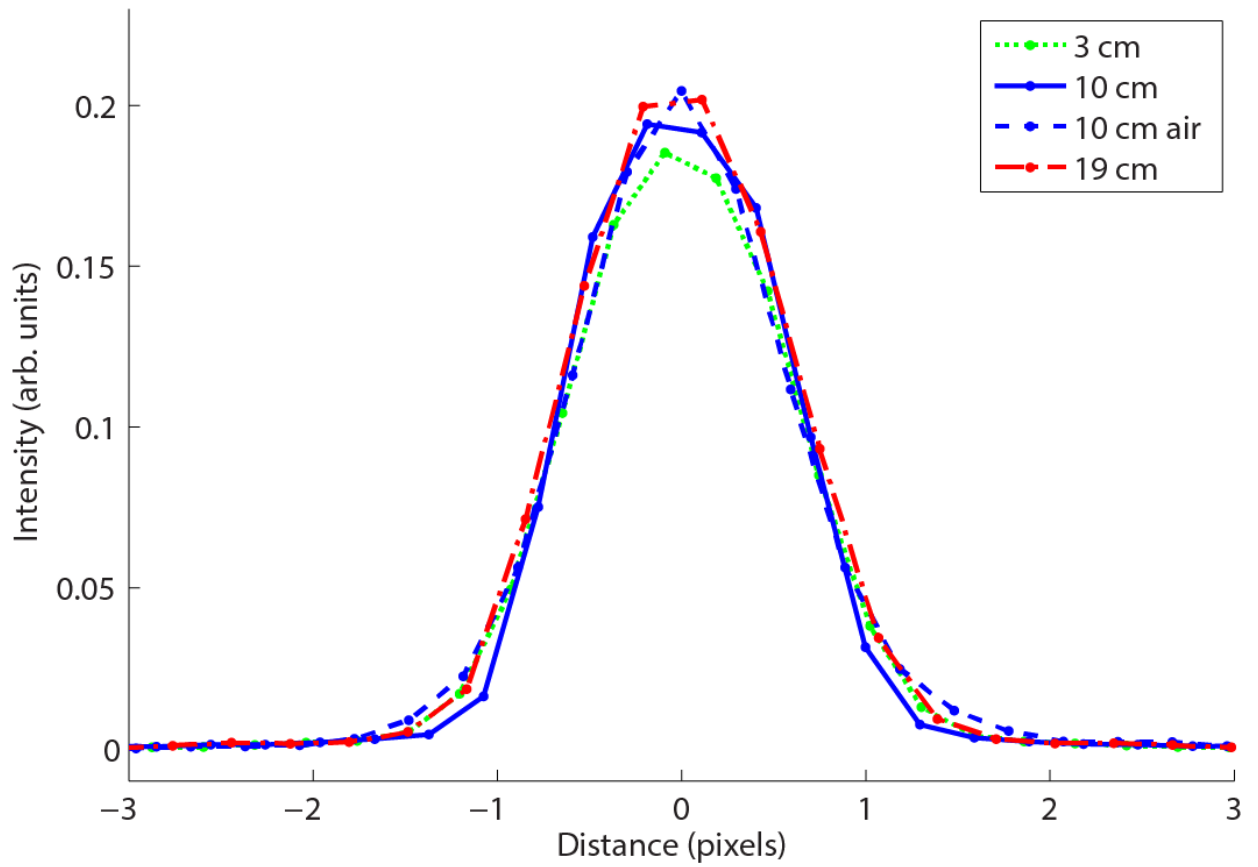


Figure 3.10 The PSF of the scintillator detector, measured at a distance of 3 cm (green), 10 cm (blue), and 19 cm (red) behind the tank window, and the PSF of the lens measured in air at a distance equivalent to 10 cm behind the tank window (blue dashed).

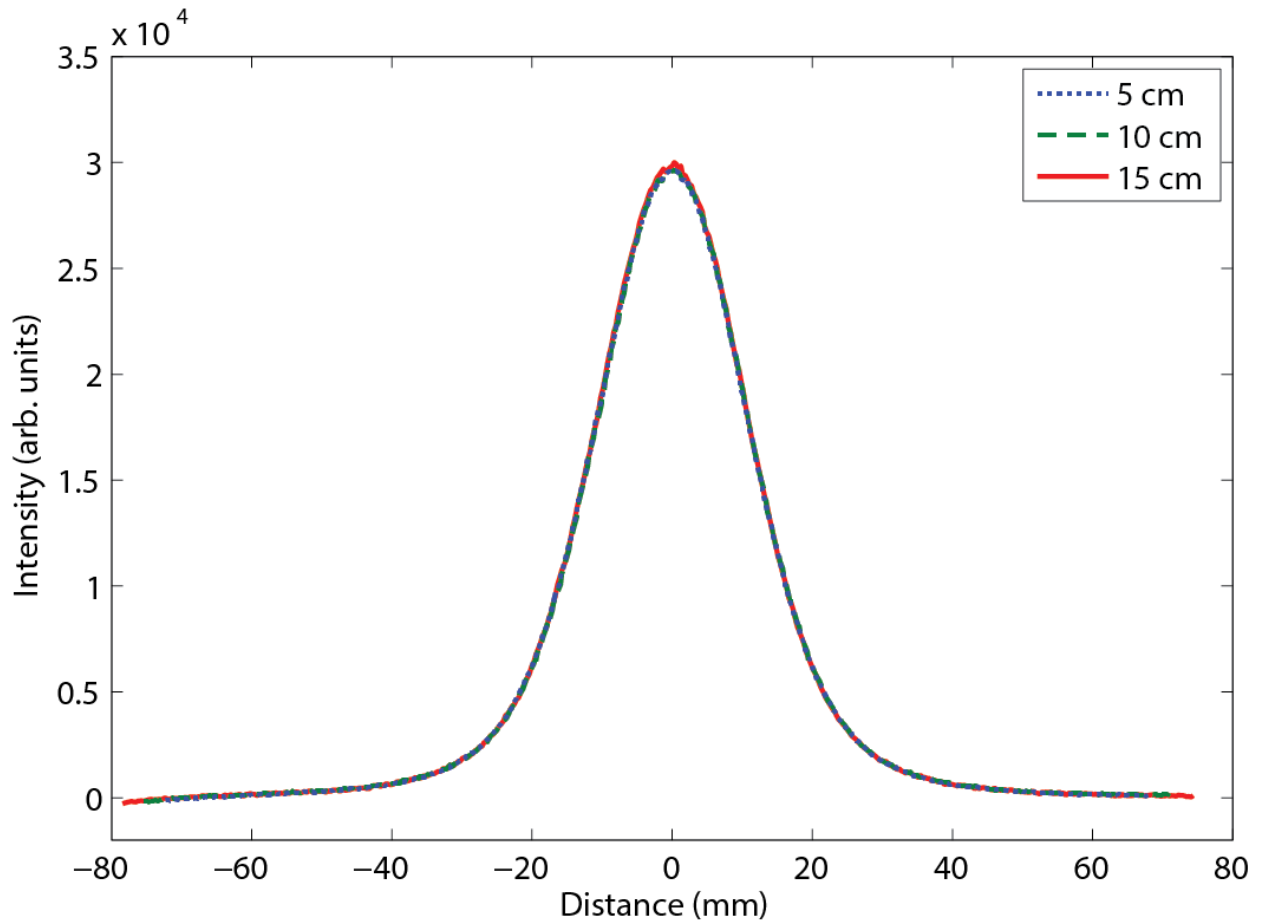


Figure 3.11 The lateral profile at the Bragg peak of a 144.9 MeV proton pencil beam, delivered at a distance of 5 cm (blue), 10 cm (green), and 15 cm (red) behind the tank window.

3.3.4 Artifact correction evaluation

The corrected CCD light distribution on the beam's central axis exhibited a clear improvement in agreement with the Monte Carlo light distribution in comparison to the uncorrected CCD light distribution (Figure 3.12). The light distributions all exhibited decreased signal in the Bragg peak due to quenching, as described in section 2.3.2.

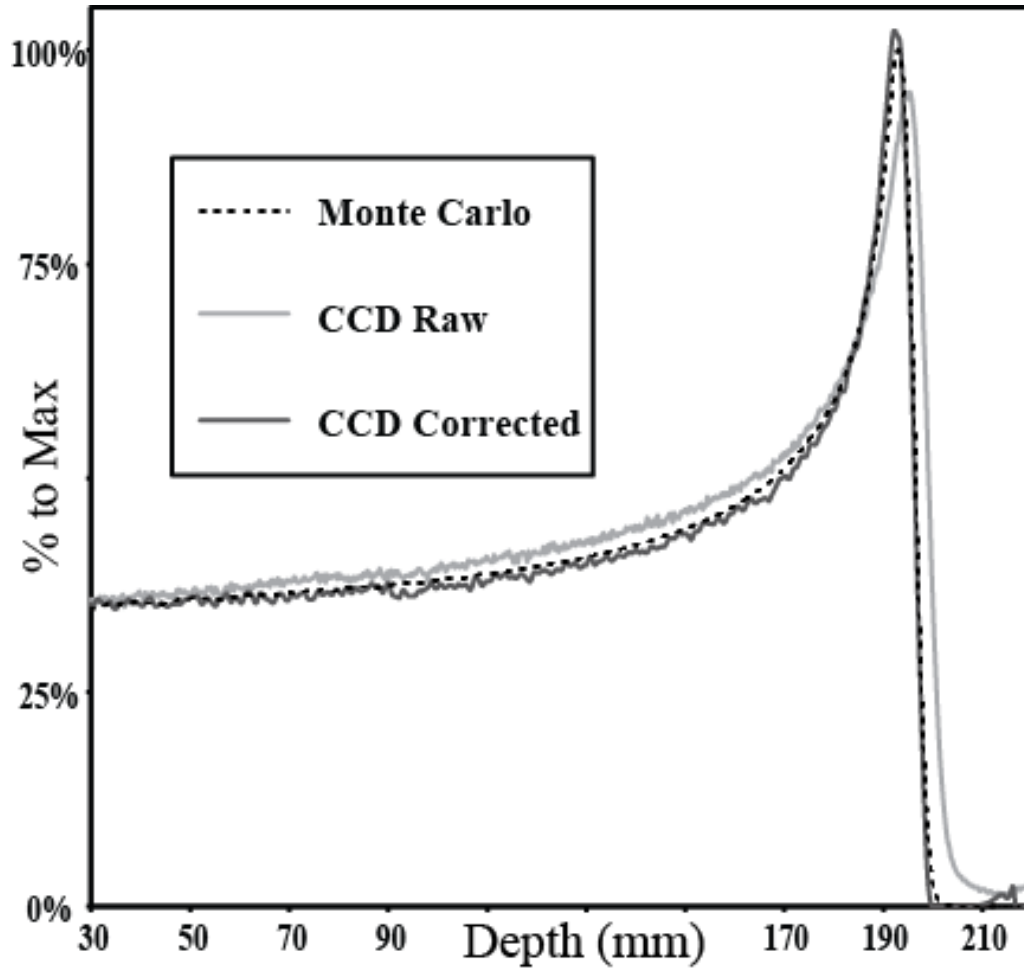


Figure 3.12 Central-axis comparison of light signals from Monte Carlo calculations (dashed line) and the raw (gray) and corrected (black) CCD images.

Gamma analysis was used to compare the scintillation light measurements from the LS detector system with the projected scintillation light distributions calculated using Monte Carlo methods. The minimum gamma analysis parameters that provided ‘acceptable agreement’ were 2%/2 mm and 3%/1 mm. The gamma analysis pass rates for the varying gamma criteria are given in Table 3.2 for each of the four beam energies. The gamma pass maps with the 2% and 2 mm criteria are shown in Figure 3.13 for the 85.6-MeV and 144.9-MeV proton beams.

The gamma analysis clearly demonstrates the effectiveness of the optical artifact corrections applied to the CCD data. With the common gamma criteria of 3%/3 mm, the average passing rate rose from 85.6% for the uncorrected light distributions to 99.7% for the

corrected distributions. Using the more stringent criteria of 2%/2 mm, the difference was larger, rising from 65.9% for the uncorrected distribution (Figure 3.13, top) to 98.2% for the corrected distribution (Figure 13, bottom) on average.

Table 3.2 Gamma analysis pass rates for proton pencil beam light distributions measured with the scintillator detector, as compared to projected dose distributions calculated using Monte Carlo methods.

Gamma Criteria	Gamma Analysis Pass Rates							
	85.6 MeV		100.9 MeV		144.9 MeV		161.6 MeV	
	Original	Corrected	Original	Corrected	Original	Corrected	Original	Corrected
3%, 3 mm	80.7%	99.1%	81.9%	99.7%	84.5%	100.0%	95.3%	100.0%
2%, 3 mm	80.3%	98.9%	81.5%	99.7%	84.0%	100.0%	94.9%	99.9%
1%, 3 mm	79.3%	98.7%	80.6%	99.6%	82.8%	99.7%	94.1%	99.8%
3%, 2 mm	61.2%	95.3%	63.5%	98.4%	65.3%	99.9%	76.2%	99.9%
2%, 2 mm	60.6%	94.9%	62.9%	98.3%	64.6%	99.9%	75.5%	99.8%
1%, 2 mm	59.4%	93.9%	61.6%	98.0%	63.4%	99.5%	74.0%	99.4%
3%, 1 mm	31.8%	76.9%	31.7%	85.1%	37.7%	97.8%	43.9%	99.7%

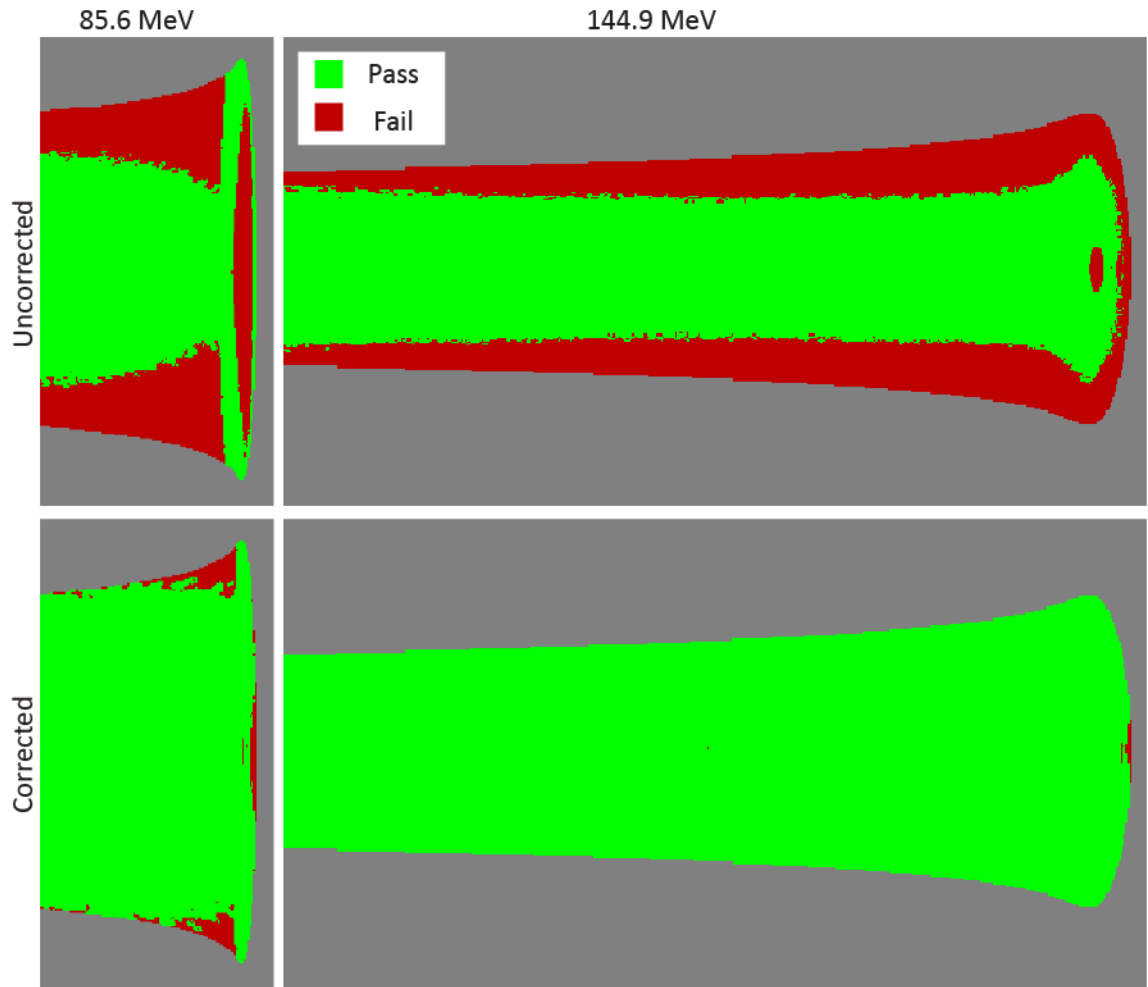


Figure 3.13 Gamma analysis pass maps with gamma criteria of 2% and 2mm for 85.6-MeV (left) and 144.9-MeV (right) proton pencil beams. Passing pixels are in red, and failing pixels are in green. The blue pixels are below the dose threshold (5% of maximum dose) and were not considered in the gamma analysis. Top) Uncorrected CCD images. Bottom) Corrected CCD images.

To evaluate the contribution of each step in the overall correction process, the gamma analysis was repeated with each of the corrections omitted. The results are shown in Table 3.3. The contribution of the spatial median filter, vignetting, and lens distortion corrections was minimal. The refraction correction was larger, and the greatest proportion of the overall correction was contributed by the blurring correction.

Table 3.3 Differences in gamma analysis (2%, 2 mm) pass rates for measured CCD images lacking one of the optical artifact correction steps, as compared to projected dose distributions calculated using Monte Carlo methods. The comparison was performed for four beam energies.

Post-processing	Difference in Pass Rates			
	85.6 MeV	100.9 MeV	144.9 MeV	161.6 MeV
No correction	-34.8%	-35.6%	-35.3%	-24.4%
w/o median filter	0.4%	0.1%	0.0%	0.0%
w/o vignetting	0.0%	-0.4%	0.0%	0.0%
w/o lens distortion	0.9%	0.1%	-0.1%	0.0%
w/o refraction	-26.4%	-12.5%	-1.5%	-3.5%
w/o de-blurring	-18.4%	-19.6%	-20.8%	-7.5%

3.4 Discussion

3.4.1 Point spread function

We determined that blurring from the lens was the primary source of the overall PSF, while light scatter in the scintillator was negligible. This was contrary to our expectations, as previous studies assumed that light scatter was the primary source of blurring. This result suggests that the scintillator BC-531 effectively meets the desirable criteria of transparency to its own emissions. It also highlights the importance of using high-quality optics in order to obtain the narrowest possible PSF.

While unexpected, this finding is fortuitous, as it renders unnecessary the use of different PSFs for different depths within the scintillator tank. While photon scatter proved to be insignificant in this study, we wish to emphasize that this result is valid only for the scintillator BC-531, and that the level of scattering in other scintillators has not yet been evaluated for this application. The primary significance of this finding is that blurring due to the lens is non-negligible and requires separate treatment from blurring due to light scatter.

3.4.2 *Gamma analysis*

In our results, the areas that most frequently failed the gamma analysis were the low-dose edges, where noise and offsets in the background level have a much larger influence than they do on the beam axis. This is a result of our decision to use a percentage of the local pixel dose in our gamma analysis rather than a percentage of the maximum dose, as is commonly used in radiation therapy dose evaluation. The local dose difference is a stricter criterion, which provides more meaningful comparisons in low-dose regions. Had we chosen to use a percentage of the maximum dose, the pixels in these low-dose areas would have passed.

The vignetting and lens distortion corrections showed little contribution to the gamma pass rate in this study, and in some cases they even caused a small decrease in the passing rate. However, the value of these corrections should not be overlooked. The vignetting and lens distortion corrections are largest at the edges of the image, and because our dose distributions included very little data near the image edges, these corrections appeared to have little effect. That being said, the use of low-distortion lenses and telecentric lenses could render lens distortion and vignetting corrections unnecessary, especially considering that the data at the tank edges are likely to be less important than the data in the centre.

The spatial median filter had a small negative effect on the gamma pass rates. This is unsurprising given the tendency of median filters to blur sharp edges. However, this effect was small, and gamma analysis is not sensitive to the spikes and streaks that the median filter is designed to remove. The median filter may prove to be more important when multiple cameras are used to obtain a 3D reconstruction of the light distribution, as high-intensity spikes could interfere with 3D reconstruction algorithms.

3.4.3 Sources of error

The central-axis light signal data shown in Figure 3.12 reveal an imperfect match between the Monte Carlo calculations and the corrected CCD data. The disagreements may come from several possible factors, including noise in the CCD measurements as well as imperfections in the correction factors and Monte Carlo calculations. The refraction and perspective corrections only apply analytically to one plane within the detector, and the light signal outside of that plane cannot be completely corrected for these phenomena. However, we believe that in the current study, this limitation was not observed because the dose was concentrated along a single narrow pencil beam.

The most notable disagreement between the CCD and Monte Carlo data was in the maximum light intensity at the Bragg peak, which differed by $\pm 3\%$. This variation was unsurprising, given the sharpness of the proton Bragg peak and the high spatial resolution of the data. An additional source of error in the Bragg peak height came from the quenching parameters applied to the Monte Carlo dose calculations to obtain the Monte Carlo light distribution. In a previous study, we reported that this quenching calculation method was accurate to within $\pm 5\%$ (Robertson *et al.*, 2013), and the maximum errors in that study were in the Bragg peak. This source of uncertainty alone is sufficient to explain the deviations between the Monte Carlo and CCD peak light values. Further efforts to decrease the error in the quenching correction process are underway.

An additional source of error in the correction factors is the difficulty of exactly measuring the PSF. Our method allowed us to measure the PSF with twice the spatial resolution of the CCD camera, but this resolution was still coarse compared to the sharp peak of the PSF. We selected the peak value of the PSF by fitting a Gaussian function to the immediately surrounding data points, but this method only provides an approximate peak value. The actual peak value may vary by as much as a factor of 2, which could change the

results of the blurring correction. However, our results match the Monte Carlo data well, suggesting that our measured PSF was sufficiently close to the actual PSF to provide an accurate blurring correction for this detector system. An alternative approach for analytically calculating the lens PSF based on the lens prescription (Shih *et al.*, 2012) may provide improvements in accuracy while also facilitating the use of a PSF that varies with position inside the tank.

3.4.4 Reflections

Reflection of the scintillation light is a source of artifacts that was not dealt with directly in this study. Reflections may occur at any interface between the scintillator and the tank wall, the tank window, or the air above the scintillator. Reflections have been problematic in previous studies involving volumetric scintillation dosimetry (Beddar *et al.*, 2009; Ponisch *et al.*, 2009; Kirov *et al.*, 2005). Reflections are highly dependent on the geometry and materials of the scintillator tank, and are difficult to correct through image processing. We believe that the best approach to minimize artifacts due to reflection is to prevent them through careful detector design, such as we did in the steps described in section 3.2.1.

3.5 Conclusions

Optical artifacts introduce significant deviations into the scintillation light distribution measured by the described volumetric scintillation detector. Optical artifact corrections are essential to accurately measure the intensity and spatial distribution of the scintillation light emission.

The largest optical artifacts in this detector system are blurring due to the lens PSF and refraction at the tank window-air interface. Blurring can be corrected very effectively by deconvolution of the PSF, which can be directly measured using the process described above. Refraction can be analytically modelled and corrected because of the simple geometry of the

detector system. Photon scatter in the scintillator was not found to be a significant source of artifacts.

Other optical artifacts that introduce detectable deviations to the measured light signal include vignetting, lens distortion, and the spikes and streaks caused by stray radiation incident on the CCD chip. These artifacts can be corrected through camera calibration and image filtering, but the correction steps may be unnecessary, depending on the prevalence of stray radiation in the vicinity of the camera and the quality and type of optical components.

Using the described correction methods, we have demonstrated gamma analysis passing rates of 95% or higher with the criteria of 2% local dose difference and 2 mm distance to agreement, when comparing corrected images from the scintillation detector to dose distributions calculated using Monte Carlo methods. We conclude that optical artifacts must be addressed in order to obtain accurate light measurements, and we have demonstrated effective strategies for correcting these optical artifacts. The optical artifact correction methods described here can be directly applied to future systems incorporating multiple cameras to facilitate a full 3D reconstruction of the light signal.

CHAPTER 4

QUENCHING CORRECTION FOR VOLUMETRIC SCINTILLATION DOSIMETRY OF PROTON BEAMS

This chapter is based upon material that was published in Physics in Medicine and Biology in January 2013 by the author of this dissertation [Robertson D, Mirkovic D, Sahoo N and Beddar S 2013 Quenching correction for volumetric scintillation dosimetry of proton beams Phys. Med. Biol. 58 261-273]. Upon transfer of copyright, IOP Publishing grants back to authors the right to include the article in research theses or dissertations.

4.1 Introduction

Volumetric scintillation dosimetry is a promising new area of study with the goal of making fast, high-resolution measurements of three-dimensional (3D) dose distributions. Interest in 3D dosimetry has increased as highly modulated conformal radiation therapy techniques have grown more complex and become common in the clinic. The 3D dosimetry approach is particularly important for proton therapy because the finite range of the proton beam makes it possible to modulate the dose in depth. As a result, it is not possible to predict the proton beam dose at all depths on the basis of the dose at a single depth, as is the case with photon-based modalities. Therefore, measurements must be made at multiple depths to fully characterize a proton beam dose distribution (ICRU, 2007). For instance, the clinical standard for patient-specific quality assurance at the Proton Therapy Center-Houston is to measure intensity-modulated proton therapy treatment fields by delivering each field multiple times to a two-dimensional array of ionization chambers placed at different depths in a plastic water phantom (Arjomandy *et al.*, 2010). The quality assurance process can take 6-8 hours per patient, limiting the number of patients who can benefit from intensity-modulated proton therapy.

Three-dimensional scintillation dosimetry with a liquid scintillator (LS) was originally proposed and explored by Kirov *et al.* (2000; 2005) for brachytherapy eye plaques in a small detection volume. Fukushima *et al.* subsequently developed a proton beam range-

measurement tool using a long, narrow block of plastic scintillator (2006). Our research group has developed a large-volume LS detector with the goal of rapidly measuring 3D dose distributions (Beddar *et al.*, 2009; Ponisch *et al.*, 2009; Archambault *et al.*, 2012). This detector system exhibits a linear dose response, a spatial resolution of 0.3 mm, and a temporal resolution of 0.05 seconds (Archambault *et al.*, 2012). The current system gathers light from a single viewing angle. However, future detectors will measure from multiple viewing angles, making 3D dose reconstruction possible.

The functional principle behind volumetric scintillation dosimetry is the gathering of light emissions from a volume of scintillating material, followed by 3D reconstruction of the light distribution. If the light emission from the scintillator is proportional to the dose deposition, then the measured light distribution is equivalent to a relative dose distribution. This process is complicated in proton beams by a phenomenon known as ionization quenching. While the mechanism of ionization quenching is not fully understood, the result is an underresponse of the scintillator in regions with a very high ionization density (Birks, 1951; Chou, 1952). This condition is met in the Bragg peak of therapeutic proton beams, where the low proton energy corresponds to a sharp increase in the stopping power (ICRU, 1993). Ionization quenching removes the linear relationship between dose and scintillation light in proton beams, making scintillation dosimetry for proton beams more challenging.

The goal of this study was to develop an ionization quenching correction method to restore the linear dose response of scintillators irradiated by proton beams. The quenching correction method is based on an empirical model that predicts quenching on the basis of the linear energy transfer (LET) of the proton beam (Birks, 1951). A recent study found that this model can be used to correct for quenching in plastic scintillator detectors, showing an agreement within 5% between scintillator and ionization chamber measurements of proton beams (Wang *et al.*, 2012).

The LET values were calculated using Monte Carlo and analytical methods. The material-specific quenching coefficient for the scintillator was obtained by measuring the light emission as a function of depth using a novel miniature liquid scintillator detector. This approach ensured that the measured quenching coefficient was independent of optical artefact corrections associated with the volumetric detector. The quenching correction method was applied to images from the volumetric detector, and the accuracy of the corrected dose measurements was determined by comparing them with doses calculated using a validated Monte Carlo model.

4.2 Materials and methods

4.2.1 Quenching model

In this study, ionization quenching was modelled using the empirical formula developed by Birks (1951). This model describes scintillation light emission in terms of the stopping power of the scintillator for the particle beam:

$$dS/dx = \frac{A \cdot dE/dx}{1 + kB \cdot dE/dx} \quad (4.1)$$

where S is the scintillation light emitted, dE/dx is the energy deposited by the protons over a distance x in the medium, A is the scintillation efficiency of the medium, and k and B are empirical factors describing the nonscintillation energy loss in the medium. An additional multiplicative factor ϵ should technically be added to account for the collection efficiency of the light, which is dependent on the detector geometry and the attenuating properties of the materials. However, in this work ϵ is implicitly included in the parameter A . In the Birks model, $B \cdot dE/dx$ is the specific density of ionized and excited molecules along the particle track, and k is the quenching parameter (Birks, 1964). These two values are difficult to obtain

individually from measurements, so as a general practice k and B are treated together as a single parameter kB .

When a realistic therapeutic proton beam is considered, it is appropriate to replace the stopping power term of the Birks equation with LET, which is defined as the average stopping power in a given region (Berger, 1993; ICRU, 1970). LET values can be generated via Monte Carlo calculations or using an analytical equation, such as that developed by Wilkens and Oelfke (2002). While the analytical method allows for arbitrarily small values of dx , the use of Monte Carlo calculations requires a finite voxel size. Measurements of scintillation light also require a finite detection volume. We can rewrite equation 4.1 in terms of finite voxels as follows:

$$S_v = \frac{A \cdot L_v}{1 + kB \cdot L_v} \phi_v \quad (4.2)$$

where S_v is the light emitted from a voxel of volume v , L_v is the track-averaged LET within the voxel, and ϕ_v is the particle fluence in the voxel. The track-averaged LET is defined as the arithmetic mean of the stopping power of all protons in a given region. Because L_v is an average LET value, it does not provide information about the absolute energy deposited in the voxel. The fluence term (ϕ_v) is added to scale the emitted light according to the energy deposited.

4.2.2 Quenching correction factors

To convert a LS detector's light signal into a dose measurement, a quenching correction factor is required. This factor may take the form

$$Q_v = \frac{E_v}{S_v} \quad (4.3)$$

where Q_v , the correction factor for voxel v , is the ratio of the deposited energy to the emitted light for voxel v . In this form, the energy deposited in a voxel can be recovered by multiplying

the correction factor by the light emitted from a voxel. Because the energy deposited in a voxel is equivalent to the track-averaged LET in that voxel multiplied by the particle fluence through the voxel,

$$E_v = L_{t,v} \cdot \phi_v \quad (4.4)$$

we can combine equations 4.2, 4.3, and 4.4 to describe the quenching correction factor as

$$Q_v = \frac{1 + kB \cdot L_v}{A}. \quad (4.5)$$

In our prototype, each pixel in the charge-coupled device (CCD) camera measures the light emitted from a column of LS extending from the window to the back of the tank. The column corresponding to each pixel is treated as a single voxel, with the dose and LET averaged over the entire column. By applying the quenching correction factors to all pixels, one obtains a two-dimensional projection of the dose distribution in the LS tank. This distribution can be compared to dose projections from a treatment planning system or Monte Carlo calculation.

4.2.3 LS detector system

The LS detector system has been described in previous publications (Ponisch *et al.*, 2009; Beddar *et al.*, 2009). It consists of a tank of LS with dimensions of 20 x 20 x 23 cm³. The LS (BC-531, Saint Gobain) consists of fluorescing molecules in a linear alkyl benzene solvent with a physical density of 0.87 g/cm³ as given by the manufacturer and a measured water equivalent thickness of 0.872 cm. The LS emits photons with a wavelength distribution centred at 425 nm. The tank is constructed of opaque gray polyvinyl chloride (PVC) with a clear polymethyl methacrylate (PMMA) viewing window on one side. The PVC continues past the viewing window, forming a light-tight housing 70 cm beyond the tank, for a total length of 90 cm (figure 4.1). A CCD camera (Andor Luca S) is attached to the far end and fit with an objective

lens to bring the LS volume into focus. The CCD has a resolution of 658 x 496 pixels, and the effective pixel size at the centre of the tank is 0.29 mm.

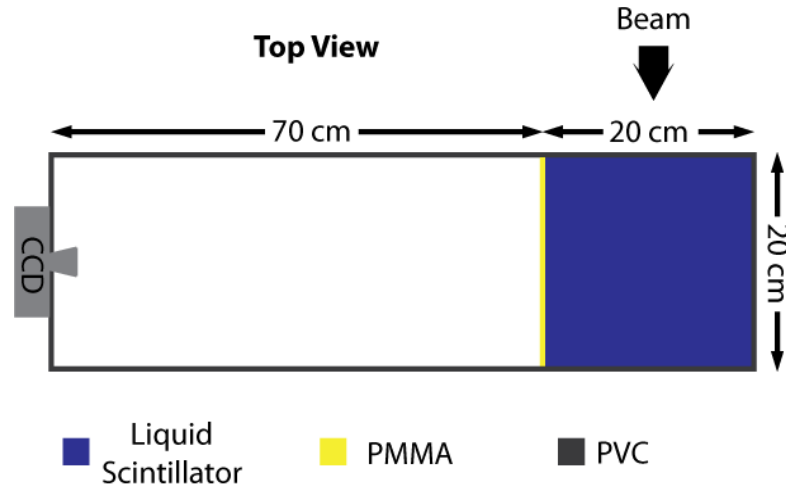


Figure 4.1 Schematic of LS detector system.

4.2.4 Image processing

The CCD images were processed to correct for artefacts introduced by the camera and the detector geometry. Background subtraction was performed using the average of a sequence of dark images. Depending on the timing of the camera acquisition and the number of monitor units delivered, consecutive images were needed to measure the entire beam delivery. In these cases, the images were summed to provide the total light measurement. A spatial median filter was used to remove random spikes caused by stray radiation incident on the CCD chip, as demonstrated previously (Archambault *et al.*, 2008). A lens calibration technique developed by the computer vision community was used to correct for lens aberrations (Bouguet, 2010). Vignetting was corrected by assuming a $\cos^4\theta$ vignetting function, and refraction at the tank-air interface was accounted for by calibrating the pixel size with a grid inside the LS tank. Blurring caused by light scatter in the LS was corrected by deconvolving a mathematically modelled point spread function from each image.

4.2.5 Monte Carlo LET and dose data

Three-dimensional LET and dose distributions of proton pencil beams were calculated using the Monte Carlo radiation transport code MCNPX, version 2.7d (Waters *et al.*, 2002). These data were calculated for 85.6, 100.9, 144.9, and 161.6 MeV proton beams using validated phase space models of the scanning beam nozzle at the Proton Therapy Center-Houston. The phase space files were generated from a complete model of the nozzle based on blueprints and validated with dose measurements (Sawakuchi *et al.*, 2010). The geometry of the Monte Carlo model mimicked the experimental setup, with the proton beam perpendicularly incident on the face of a cubic phantom of water or LS. The face of the phantom was located at the gantry isocenter. The tallies were counted on a cubic grid measuring $8 \times 8 \text{ cm}^2$ perpendicular to the beam and extending 1 cm or more beyond the end of the Bragg peak for each energy. The voxel size was $1 \times 1 \text{ mm}^2$ perpendicular to the beam, and the length of the voxels in the beam direction was 1 mm in the proximal build-up region and 0.1 mm in the Bragg peak.

For each beam energy, 5×10^7 incident protons were simulated, resulting in an uncertainty of less than 1% for all voxels with doses exceeding 2% of the maximum dose. All secondary particles were tracked. The energy deposition and particle flux and their uncertainties were scored in each voxel. The track-averaged LET was used in this study for simplicity and was calculated by dividing the energy deposition in each voxel by the particle fluence. The same equations and quenching correction method could be used with the dose-averaged LET if desired, but the values of the empirical parameters would change.

4.2.6 Analytical LET calculation

While the quenching parameters in this study were primarily determined using LET values calculated with the Monte Carlo model, LET values were also calculated using an analytical formula for comparison. Analytical LET calculation methods are much faster than

Monte Carlo methods, and speed is an important consideration in situations involving numerous beam energies or complex geometries. The analytical method of Wilkens and Oelfke (2002) was used to calculate LET values on the central axis of the beam. For 3D calculations, this model assumes a laterally constant LET (Wilkens and Oelfke, 2004). This approximation is justified by the small magnitude of the off-axis changes in LET.

4.2.7 Quenching parameter determination

The empirical parameters of the Birks model were determined by fitting the model to match measured light emissions and calculated LET values. To decouple the Birks parameters from the optical artefact corrections that were applied to the CCD images, an alternate means of scintillation light measurement was employed to determine the Birks parameters. Miniature LS detectors were constructed using optical fibres. The optical fibres consisted of a 1-mm-diameter clear plastic core covered by a 0.6-mm-thick opaque cladding, for a total diameter of 2.2 mm. A section of cladding was removed, and one end of the cladding was sealed to form a cap. This cap was filled with LS and glued to a section of stripped fibre (figure 4.2). The resulting assembly consisted of a cylinder of LS with a diameter of 1 mm and a length of 5 mm (for a total volume of approximately 0.004 cm^3) in direct contact with the optical fibre. The fibre ends were inserted into a modified lens cover connected to the CCD camera lens, allowing the camera to measure the light output from several miniature detectors simultaneously.

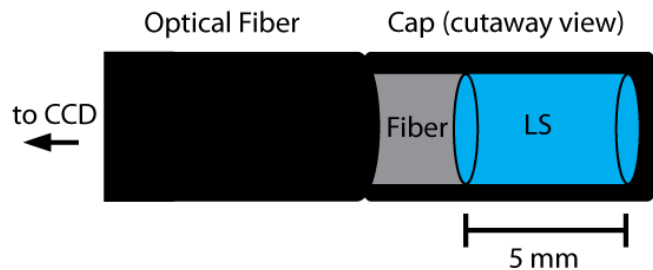


Figure 4.2 Schematic of miniature LS detector.

The linearity of the miniature LS detector response was verified using a clinical 6-MV photon beam (Varian 6EX). Several miniature detectors were placed in an acrylic phantom and irradiated with a 10 x 10-cm² field with exposures ranging from 50 to 500 monitor units. To account for the presence of Cerenkov light produced in the LS and fibres, a fibre with no detector was irradiated simultaneously, and the signal from this fibre was subtracted from the signal in the detectors, following the method proposed by Beddar *et. al.*(1992a, b). Cerenkov light is minimal in proton beams in the therapeutic energy range, so this subtraction is unnecessary for proton beam measurements.

Two miniature LS detectors and one fibre with no detector were used to measure the light signal on the central axis of a 161.6-MeV proton pencil beam in the scanning beam gantry at the Proton Therapy Center-Houston. The measurements were performed in a water-equivalent plastic phantom using a constant source-to-surface distance. For each measurement, 20 monitor units were delivered (as defined by Gillin et al. (2010)), and the light signal was measured by the CCD camera in a single exposure. The depth was corrected according to the measured water equivalent thickness of the plastic slabs.

The quenching correction factors were calculated using equation 4.5 with LET values generated by the Monte Carlo calculations described in section 2.5. These correction factors were applied to the light signal from the miniature LS detectors. The difference between the corrected scintillation signal and the Monte Carlo central-axis dose was then minimized using a least-squares curve-fitting algorithm to determine the optimal values of A and kB . An additional scaling factor was folded into the parameter A to account for differences in the light collection geometry between the miniature LS detectors and the large-volume LS detector system.

4.2.8 Quenching correction

To test the effectiveness of the quenching correction method, scintillation light distributions were measured with the large-volume LS detector for pencil beams with energies of 85.6, 100.9, 144.9, and 161.6 MeV. Quenching correction factors were calculated for each CCD pixel by applying equation 5 with the optimized quenching parameters from the miniature LS detector experiment. One set of correction factors was generated using LET values from the Monte Carlo calculations, and another was generated using LET values from the analytical method. Projected dose distributions for the four pencil beams were obtained by multiplying the light distributions by the correction factors.

The corrected light measurements from the LS detector system were compared to projected dose distributions from Monte Carlo calculations for the four beam energies. The degree of agreement was evaluated qualitatively by comparing depth-dose profiles on the beam axis and cross-plane profiles at three depths corresponding to the proximal build-up region (3.5 cm depth), the proximal 50% dose, and the centre of the Bragg peak for each beam energy. The degree of agreement was evaluated quantitatively by comparing the peak-to-plateau ratio and the Bragg peak height for the calculated dose, the measured light signal, and the corrected signal. The peak-to-plateau ratio was defined as the ratio of the dose or signal at the centre of the Bragg peak to the dose or signal at 3.5 cm depth on the beam's central axis.

4.3 Results

4.3.1 Miniature LS detector linearity

The LS detectors showed excellent linearity in their dose response. Because the linearity test was performed in a 6-MV photon beam, the scintillation light was mixed with Cerenkov light. After subtraction of the Cerenkov contribution, a linear fit of scintillation light versus the monitor units delivered by the linear accelerator exhibited an R^2 value of 0.9999 (figure 4.3),

indicating excellent linearity. No Cerenkov light was detected when the LS was irradiated in proton beams.

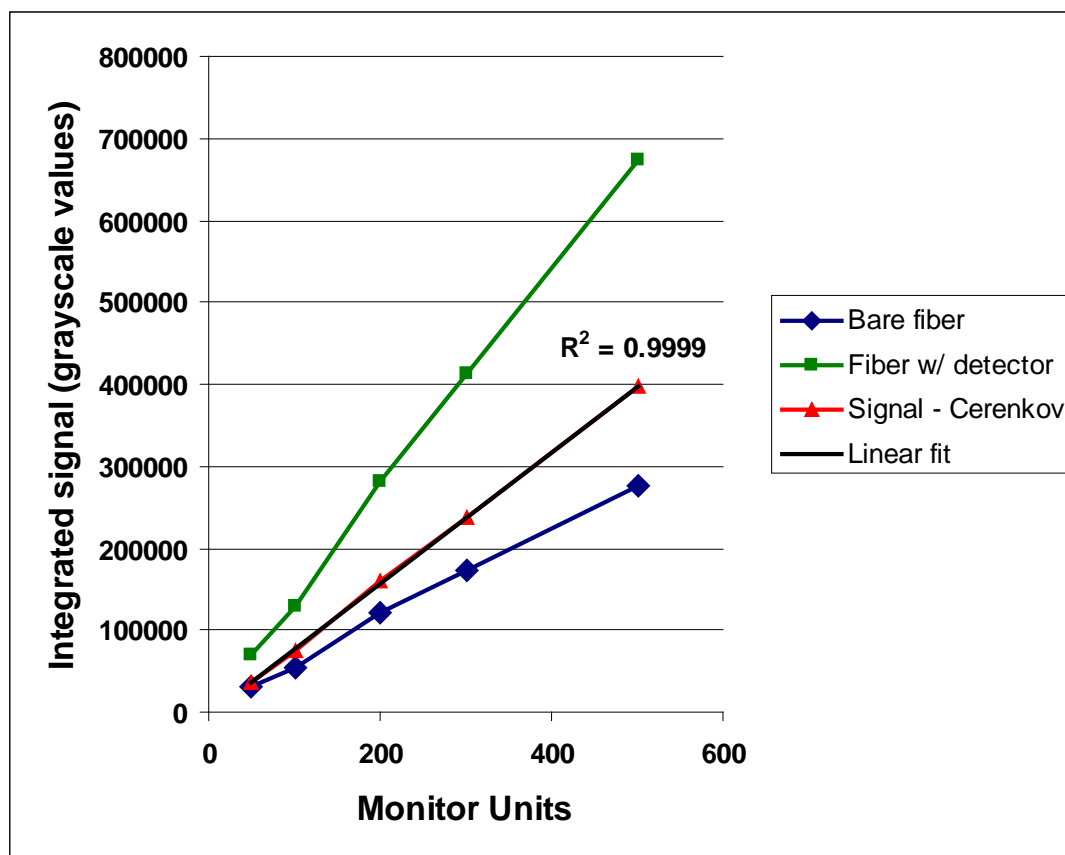


Figure 4.3 The results of a linearity test of a miniature LS detector in a 6-MV photon beam. The scintillation light (red) was measured by subtracting the Cerenkov signal (blue) from the miniature LS detector signal (green). The R^2 value of a linear fit to the scintillation signal was 0.9999.

4.3.2 LET calculation

The Monte Carlo and analytical LET values agreed within $\pm 5\%$ on the central axis of the proton beam (figure 4.4). The maximum quenching correction factor calculated in this study was 25%, which translates to a maximum dose error of 1.25% when using analytical LET values. In practice, the corrected dose using analytical LET values differed by less than 1% from the corrected dose using Monte Carlo LET values, because the analytical LET equation was more accurate in the Bragg peak region where the largest quenching correction factors

occurred. This level of error is comparable to the noise level of the CCD chip and does not significantly affect dose measurements. The off-axis LET values differed by as much as 22% in pixels containing 1% or more of the peak dose (figure 4.5). This increase occurred mainly in very low dose regions, and it did not result in an appreciable effect on the corrected dose (figure 4.6).

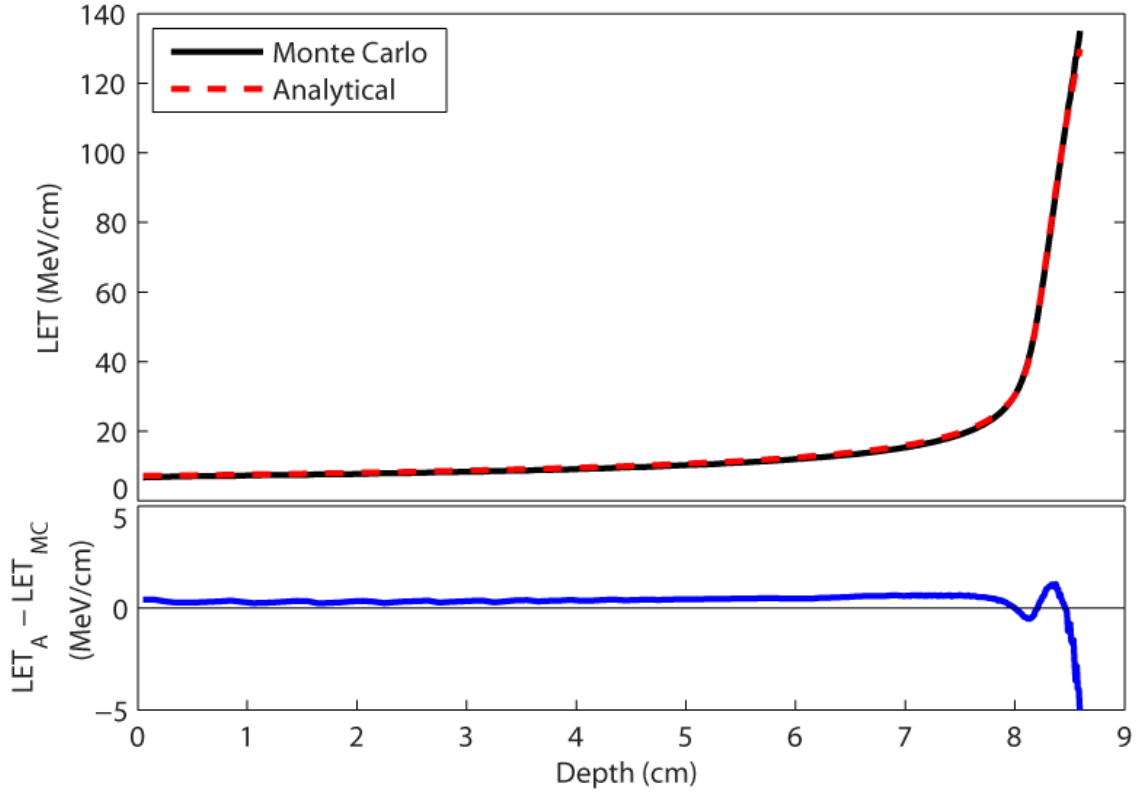


Figure 4.4 (top) Track-averaged LET calculated with Monte Carlo methods and with an analytical formula for a 100.9-MeV proton beam in LS. (bottom) The difference between the analytically-derived LET values to the Monte Carlo-derived values.

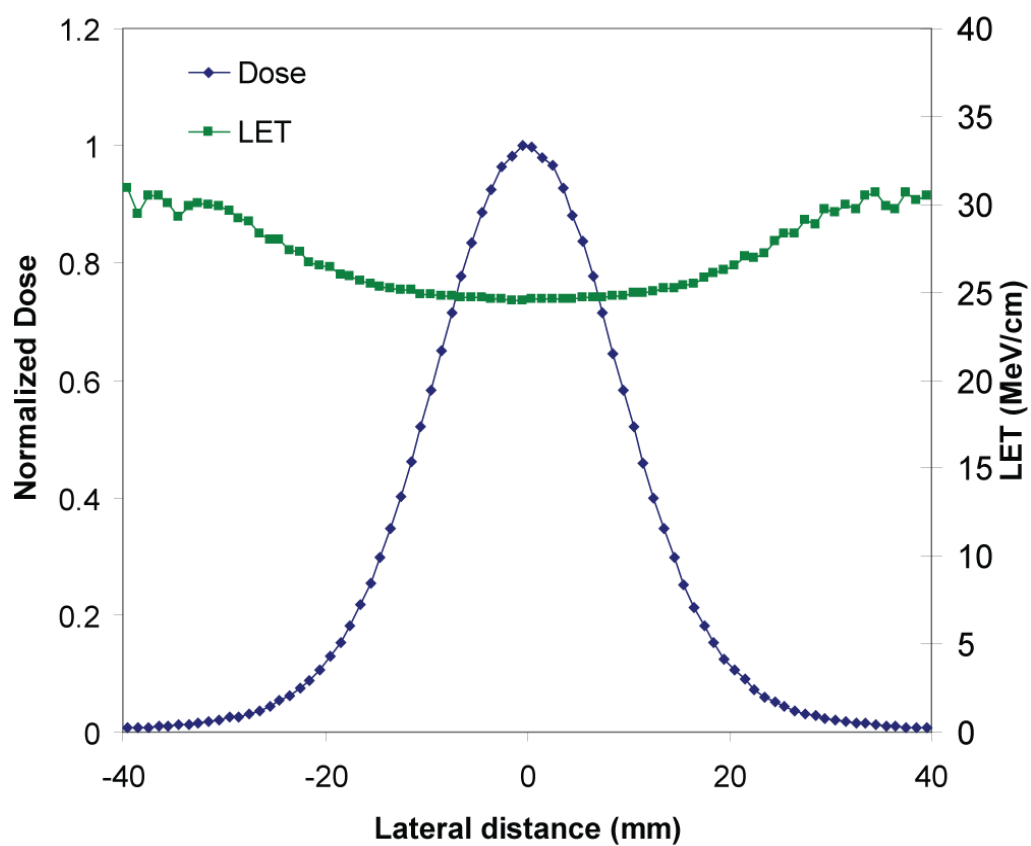


Figure 4.5 The Monte Carlo LET calculation shows an off-axis LET increase of up to 22% in pixels containing 1% or more of the peak dose. The lateral dose profile is shown for reference.

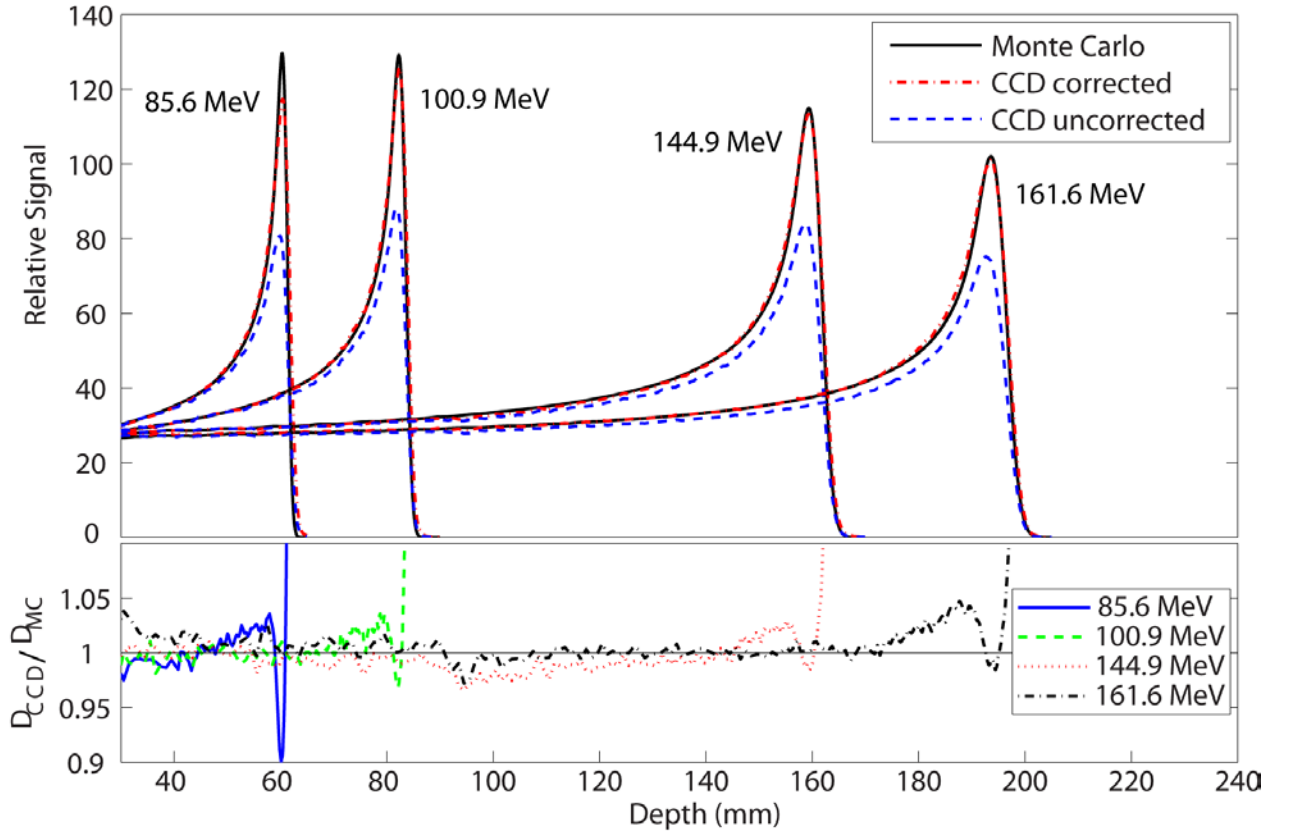


Figure 4.6 (top) Central axis depth-dose profiles for proton pencil beams. The dose calculated by the validated Monte Carlo model is shown in black. The uncorrected scintillation signal is shown in blue. The corrected scintillation signal is shown in red. (bottom) The ratio of the corrected scintillation signal to the Monte Carlo dose.

4.3.3 Quenching parameter determination

The correction factors produced by equation 4.5 with the optimized Birks parameters resulted in very close agreement between the corrected light signal and the calculated dose distribution (figure 4.7). The empirical parameters from this fit were as follows: $A = 1.94 \times 10^5$, $kB = 9.22 \text{ mg cm}^{-2} \text{ MeV}^{-1}$. The parameter A is a scaling factor that is dependent on the detector geometry and the number of particles in the Monte Carlo calculation, but kB is characteristic of the scintillating material and should not change with the experimental setup. The measured value of kB is similar to the measured kB values of other organic scintillators, which vary from 6.6 to $10.4 \text{ mg cm}^{-2} \text{ MeV}^{-1}$ (Birks, 1964).

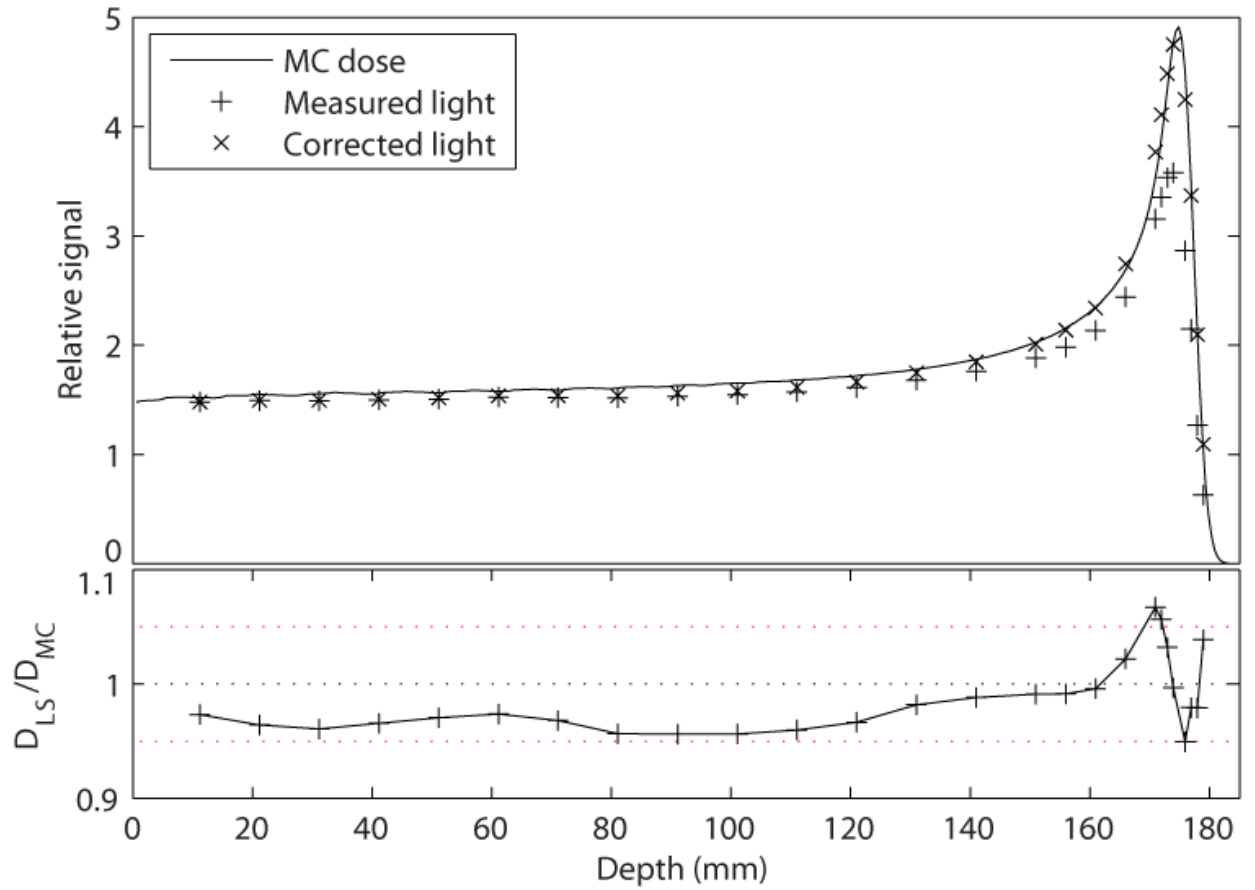


Figure 4.7 (top) The light signal from the miniature LS detectors before (+) and after (x) the correction factor was applied. The dose from the Monte Carlo calculation is shown for comparison. (bottom) The ratio of the corrected light signal (D_{LS}) to the Monte Carlo dose (D_{MC}).

4.3.4 Quenching correction

The corrected CCD measurements agreed closely with the Monte Carlo dose calculations as shown in figures 4.6, 4.8, and 4.9. The peak-to-plateau ratios for the calculated doses and corrected scintillation signals agreed well, while the peak-to-plateau ratios for the uncorrected scintillation signals were significantly decreased (table 4.1). The calculated and measured Bragg peak heights agreed within 3% for all energies except 85.6 MeV, for which the agreement was within 10% (table 4.2). The lateral penumbrae of the corrected light signals were slightly wider than the penumbrae of the calculated doses (figure 4.9). The greatest dose errors were found in the steep dose gradients in the Bragg peak, reaching 5% error in the proximal side of

the Bragg peak and significantly higher in the distal Bragg peak. The dose in these regions is particularly sensitive to the alignment of the Monte Carlo and CCD data sets as well as the parameters of the deblurring algorithm and detector size effects in the CCD and Monte Carlo verification measurements. While the dose difference was significant in these regions, the distance to agreement was less than 1 mm.

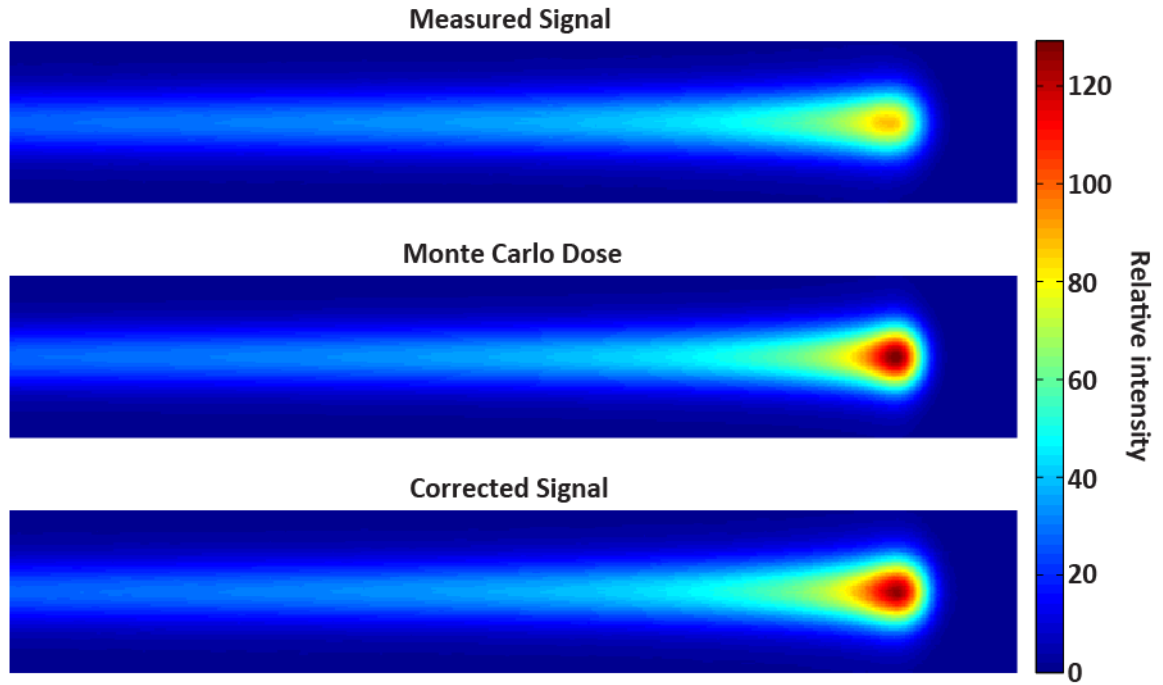


Figure 4.8 The measured scintillation signal (top), the dose calculated using Monte Carlo methods (centre), and the corrected scintillation signal (bottom) for a 100.9-MeV proton pencil beam.

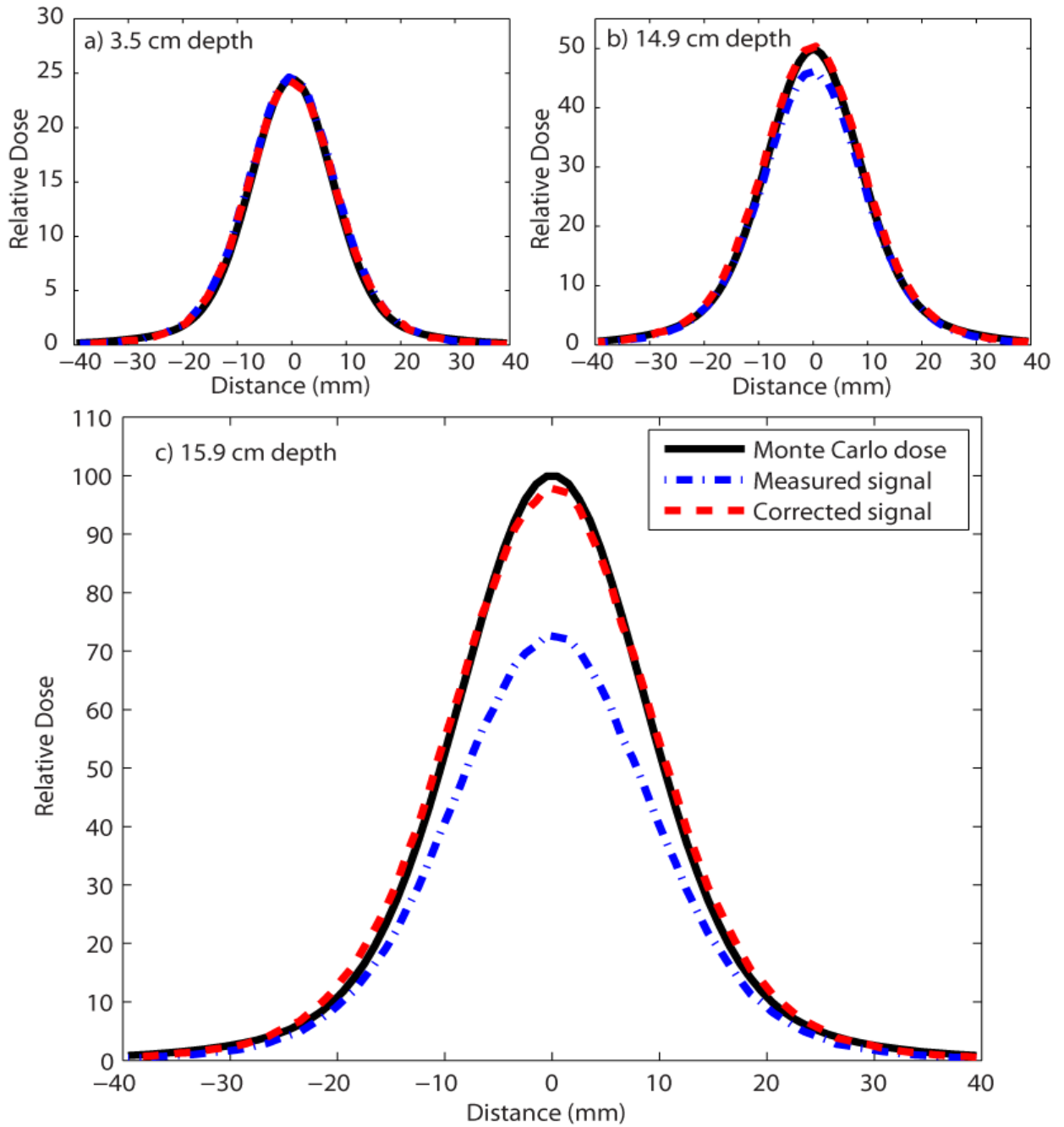


Figure 4.9 Lateral dose profiles for a 144.9-MeV proton pencil beam at three depths: **a)** 3.5 cm (proximal build-up region), **b)** 14.9 cm (proximal 50% dose), and **c)** 15.9 cm (centre of Bragg peak).

Table 4.1 Peak-to-plateau ratios for the Monte Carlo dose calculation, the measured signal from the CCD, and the corrected CCD signal.

Energy (MeV)	Peak to Plateau Ratio		
	Monte Carlo	Measured Signal	Corrected Signal
85.6	4.04	2.51	3.70
100.9	4.40	3.01	4.30
144.9	4.09	2.99	4.10
161.6	3.78	2.78	3.69

Table 4.2 Percentage difference between the calculated peak height and the peak height from the measured and corrected CCD signals.

Energy (MeV)	Percent Difference from Monte Carlo	
	Measured Signal (% difference)	Corrected Signal (% difference)
85.6	37.7	9.5
100.9	31.8	2.6
144.9	26.9	1.5
161.6	26.4	0.7

4.4 Discussion

The primary source of uncertainty in this study is the steep dose gradients and narrow high-dose regions present in proton Bragg peaks. This source of error was present throughout the measurements, including the determination of the scintillator's kB factor with the miniature detectors. The accuracy of the kB factor measurement may be increased by repeating the experiment with a more slowly-varying dose and LET distribution, such as a proton or carbon ion spread-out Bragg peak.

The decision to use Monte Carlo dose calculations as the standard of comparison in this study was appropriate considering the high resolution made possible by Monte Carlo and because of the availability of a carefully validated Monte Carlo model of the PTCH beamline. However, uncertainties in the measurements used to validate the Monte Carlo model may contribute to the differences between the calculated doses and those measured with the LS detector.

The quenching correction method proved to be effective for higher proton beam energies and less effective for the lowest energies. This decreased agreement is due to the increased sharpness of the proton Bragg peak at low energies. Measurements of very sharp Bragg peaks are prone to detector size effects. The thickness of the Monte Carlo voxels in the beam direction was set at 0.1 mm in the Bragg peak region in an attempt to avoid detector size effects. However, the effective pixel size of the CCD camera is 0.3 mm. While this may seem small, it is not small compared to the width of the Bragg peak for an 85.6-MeV proton beam, which is approximately 2 mm full width at half maximum. The result is a broader peak in the light measurement.

Additional difficulties with the very sharp low-energy peaks include imperfections in the deblurring process and imperfect alignment between the calculated and measured data. The observed difficulties with quenching correction at low energies are likely due to a combination of these effects. These effects may also be responsible for the wider lateral penumbræ of the corrected light signals. Future volumetric scintillation dosimetry systems should be optimized to obtain the smallest possible pixel size while still maintaining adequate signal collection. The current system may be further optimized by a detailed study of the point spread function of the camera system, which would facilitate improvements in the deblurring process.

4.5 Conclusions

We have developed a method to correct for scintillation quenching in a large detection volume with sufficient accuracy to fulfil dosimetric quality assurance and verification purposes. This method requires prior knowledge of the LET distribution of the beam and the Birks model parameters for the scintillator. We have calculated the LET distribution using Monte Carlo and analytical methods and measured the Birks parameters for the liquid scintillator BC-531. Our results suggest that analytical LET calculation methods are adequate

for determining the required LET distributions. This study demonstrates the effectiveness of a correction method that restores the linear dose response of a liquid scintillator throughout the proton beam range. The correction method is applied to a large-volume scintillation detector, addressing a major obstacle to fast 3D dosimetry of proton beams.

CHAPTER 5

QUALITY ASSURANCE OF SCANNED PROTON BEAM DELIVERY SYSTEMS WITH A 3D LIQUID SCINTILLATOR DETECTOR

5.1 Introduction

Proton radiation therapy is an advanced cancer treatment modality with the potential to deliver therapeutic radiation doses to tumors with less damage to healthy tissues than with photon-based methods. After several decades of development at a small number of institutions, proton therapy is currently in a phase of rapid expansion, with the number of centers in the United States expected to double in the next several years. Most older proton therapy centers employ broad, passively scattered proton beams, which are shaped to irradiate the target volume using patient-specific apertures and range compensators. However, the majority of new centers feature active scanning systems in which narrow mono-energetic proton beams are scanned across the treatment volume to form the desired dose distribution.

Scanned proton beams have several advantages over passive scattering systems, including improved dose distributions (Boehling *et al.*, 2012), decreased neutron dose to the patient (Fontenot *et al.*, 2008; Clasie *et al.*, 2010), and no need for patient-specific hardware. However, despite the clinical advantages of scanned proton beam systems, they present technical challenges in the areas of commissioning and quality assurance (QA) measurements.

Because a mono-energetic proton beam deposits its dose primarily in the Bragg peak at the end of the beam range, many different beam energies are required in a clinical system in order to cover a useful range of treatment depths. For example, at the MD Anderson Proton Therapy Center at Houston (PTCH), 94 beam energies are available in the scanning beam system (Smith *et al.*, 2009).

Ideally, the lateral profile, depth dose distribution, and scanning magnet accuracy at each of these beam energies should be measured initially as a part of commissioning and then periodically as a part of the QA program (ICRU, 2007). However, in practice only a subset of these measurements can be performed due to the prohibitive time requirements of measuring such a large number of beams. At the PTCH, several beam energies were measured during

commissioning, and the remainder of the beam data was acquired using a Monte Carlo beam model that was fit to the measured beams (Gillin *et al.*, 2010; Zhu *et al.*, 2013). While more comprehensive measurements would be desirable, they are prohibited by the busy clinical schedule, available manpower, and the limitations of current radiation detectors.

The detectors commonly used for scanned proton beam QA include ionization chambers and ionization chamber arrays, radiochromic films, and scintillating screens (Karger *et al.*, 2010). Miniature thimble-type ionization chambers may be used to measure lateral beam profiles, and parallel-plate ionization chambers may be used for depth-dose profile measurements. However, the procedure of scanning these detectors across the beam profile or beam range is too time-consuming for regular use. Arrays of ionization chambers such as the Matrixx and Zebra detectors can be used to quickly and easily make lateral or depth measurements of proton pencil beams (Arjomandy *et al.*, 2008; Dhanesar *et al.*, 2013). However, these detector arrays have limited spatial resolution and are relatively expensive.

Radiochromic film has been used successfully for lateral profile and beam position measurements of scanned proton beams. While films have very high spatial resolution, they suffer from limitations including scanner calibration instability, complex calibration procedures, and sensitivity of the film to environmental conditions (Karger *et al.*, 2010). In general, they require relatively large doses to achieve a good signal-to-noise (SNR) ratio. Furthermore, the time and effort spent in irradiating, developing, scanning, and processing of the film can be substantial, thus limiting their use for high-throughput QA measurements of many beams.

Scintillating plates measured with charge-coupled device (CCD) cameras have also been used for characterization of scanned proton beam profiles and measurement of spot positions (Boon *et al.*, 1998; Boon *et al.*, 2000). These can obtain resolution close to that of film, while providing nearly instantaneous readout. However, they are only capable of measuring lateral

profiles. One study reports the use of a block of plastic scintillator to measure proton beam ranges (Fukushima *et al.*, 2006), providing high spatial resolution and fast readout.

Liquid scintillator based detectors have several attractive features for dosimetric measurements. They exhibit high resolution and immediate readout, and the light emission from the LS occurs within nanoseconds, making it possible to perform repeated measurements very quickly. A large volume of liquid scintillator can serve as the measurement medium in addition to the detector, thus eliminating perturbations to the radiation field by the detector.

Our research group has developed a large organic liquid scintillator detector for the purpose of 2D and 3D dosimetry of photon and proton beams (Beddar *et al.*, 2009). Our previous work has focused on measuring 2D projections of the dose distribution within the scintillator using a single CCD camera (Ponisch *et al.*, 2009; Archambault *et al.*, 2012).

All large-volume scintillator/camera studies to this point have used only a single camera to image the scintillator volume, producing a 2D projection of the dose distribution in the scintillator. *It was hypothesized that a volumetric scintillator detector with two orthogonal cameras could simultaneously measure the range, lateral profile, and lateral position of multiple scanned proton pencil beams in a single measurement.*

To validate this hypothesis, a prototype volumetric scintillator was built, and the effectiveness of the prototype detector for quality assurance measurements of scanned proton beam delivery systems was evaluated. The accuracy of this detector was investigated for verification measurements of the range, width, and position of scanned proton beams. The scope of this study also comprised the evaluation of accuracy, precision, and reproducibility of these measurements.

5.2 Materials and Methods

This study consists of measurements of scanned proton pencil beams using a prototype liquid scintillator detector at the PTCH. The detector and its calibration methods will be described and the relevant aspects of the PTCH system will be summarized. Three related studies will then be described, which address important types of QA measurements that can be performed with the prototype detector, including measurements of the beam range, the lateral profile width, and the lateral position of the proton beam.

5.2.1 Detector design

The liquid scintillator detector used in this study consists of a cubic tank filled with liquid scintillator, two CCD cameras, a light-tight housing, and a mirror to redirect the light from one face of the scintillator tank to one of the cameras (Figure 5.1). The interior dimensions of the tank are 20×20 cm wide and 23 cm tall. Two adjacent sides of the tank are made of 1 cm-thickness sheets of the transparent plastic poly-methyl methacrylate (PMMA), and the other two sides and bottom of the tank are made of 1 cm sheets of black Polyoxymethylene (POM). The bottom and back side of the tank extend an additional 21 cm on one side of the tank, forming a base and enclosure for a mirror set at a 45° angle to one of the PMMA windows.

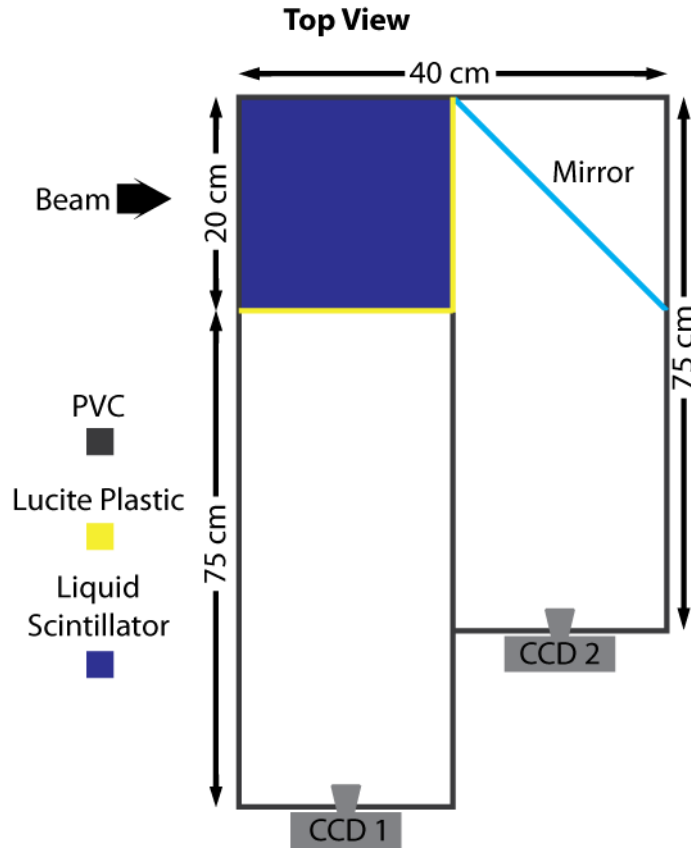


Figure 5.1 A schematic of the dual-camera detector design.

The mirror redirects the light exiting one of the windows so that it is parallel to the light exiting the other window. This arrangement serves the dual purpose of making a more compact apparatus and enabling the mirror-viewing camera to image along the proton beam axis without the risk of damaging the camera if the beam range exceeds the tank width.

The lid of the tank is removable to enable filling and emptying of the tank as well as the placement of calibration patterns within the tank. The lid also extends an additional 21 cm to one side, and it includes a fixture for the top of the 45° mirror and forms the top of the light-tight enclosure around the tank-mirror assembly. The tank and mirror were designed as a single integrated assembly in order to rigidly fix the angle of the mirror relative to the tank window.

A second interlocking assembly made of Polyvinylchloride (PVC) provides mounts for the cameras and a light-tight enclosure extending from the cameras to the window/mirror assembly. This assembly consists of two adjacent rectangular tubes with cross-sections the same size as the width and height of the tank (20×23 cm), and with lengths of 75 cm and 55 cm. The longer tube is aligned with one of the tank windows, and the shorter tube is aligned with the mirror segment of the tank/mirror assembly, and the ends of the tubes farthest from the tank are enclosed and provided with camera mounts. The lengths of the tubes were selected so that the path length of the light from the tank windows to the cameras would be equivalent.

The tank was filled to a height of 19 cm with the organic liquid scintillator OptiPhase HiSafe (PerkinElmer, details). This scintillator cocktail consists of 2,5-Diphenyloxazole (PPO) as the fluor; 1,4-Bis(2-methylstyryl) benzene (bis-MSB) as a wavelength-shifter; and a solvent mixture including Diisopropyl naphthalene, alkylphenoethoxylate, 2-(2-butoxyethoxy) ethanol, and Diethanolaminephosphoric acid ester. The density of the scintillator is 0.963 g/cm³, its refractive index is 1.5325, and its peak emission wavelength is about 425 nm.

The CCD cameras used in this study were a pair of Andor Luca S Electron Multiplying CCDs (EMCCDs) fitted with Computar M2518-MPW2 25 mm focal length objective lenses. These cameras have a resolution of 496×658 pixels and can acquire a maximum of 37 full frames per second. The CCD chips are thermo-electrically cooled to -20°C in order to decrease dark noise. During data acquisition, the cameras were connected to separate computers via USB cables. In the remainder of this chapter, the camera labeled “CCD 1” in Figure 5.1 will be referred to as the “window-facing camera,” and the camera labeled “CCD 2” will be referred to as the “mirror-facing camera”.

5.2.2 Detector calibration

The cameras were calibrated using the Camera Calibration Toolbox for Matlab (Bouguet, 2010). The calibration data consists of photographs of a black and white checkerboard pattern at multiple orientations. The toolbox features an automatic corner-detection algorithm to locate the corners of the checkerboard, from which it uses a maximum-likelihood estimation minimization algorithm to fit the parameters of a closed-form model of the intrinsic camera parameters based on the orthogonality of vanishing points (Zhang, 1999). The toolbox also features a stereo camera calibration tool which can be used to calibrate the relative position and orientation of the cameras in a stereo camera system.

While the camera calibration toolbox is effective at calibrating cameras using a pattern in air, the presence of a refracting material such as a liquid scintillator invalidates some of the assumptions implicit in the calibration method, leading to errors in the estimated intrinsic camera parameters. To overcome this challenge, the following camera calibration approach was used: First, the two cameras were calibrated separately using images of checkerboards in air. Second, the cameras were mounted in the detector assembly, and images were acquired of a checkerboard pattern suspended within the liquid scintillator tank. These images were used to perform a stereo calibration of the system. Finally, the incorrect intrinsic camera calibration parameters from the stereo calibration were replaced by the parameters from the in-air calibrations of the two cameras, while the extrinsic parameters determined during the dual-camera calibration, including the relative position and orientation of the two cameras, were left unchanged. The resulting hybrid dual-camera calibration contained correct intrinsic parameters for each camera and correct extrinsic parameters relating the cameras to one another.

5.2.3 Scanned proton beam delivery system

The PTCH scanned beam proton therapy system consists of a synchrotron, a beamline leading to an isocentric gantry with a radius of 5.5 m, and a gantry-mounted nozzle including dose monitors, beam position monitors, and two sets of scanning magnets used to change the lateral position of the proton beam (Smith 2009). 94 different beam energies have been commissioned for clinical treatment, with nominal energies ranging from 72.5 – 221.8 MeV and beam ranges between 4.0-30.6 g/cm². The lateral width of the proton beam is energy-dependent, varying from 3.4 cm full width at half-maximum (FWHM) for the 72.5 MeV beam to 1.2 cm for the 221.8 MeV beam. The lateral position of the proton beam is defined at isocenter, and the source-axis distance (SAD) is defined as the distance from the scanning magnets to isocenter. As the X and Y scanning magnets are positioned one after the other in the nozzle, the SAD is different for the X and Y scanning directions (Smith *et al.*, 2009).

5.2.4 General measurement parameters

The measurements for this study and the following two studies were performed in the same evening, and the following parameters and setup details were the same across all three studies: the detector was placed on the treatment couch, and the center of the scintillator tank was placed at the isocenter of the gantry. The room lights were turned off to reduce the potential of light leakage into the detector. The cameras were connected to two computers in the control room via USB, and a BNC cable carried a trigger signal from a computer in the control room to both of the cameras, ensuring that the camera acquisitions were synchronized. The cameras were operated in “frame transfer” mode, which enables the acquisition of consecutive images with only 0.33 ms dead time between images. The total setup time for the system was between 30-45 minutes.

All data processing and analysis were performed using Matlab release 2013a on a computer running 64-bit Windows 7 with a four-core Intel i7-3770k CPU at 3.5 GHz and 8 GB of RAM. Unless otherwise stated, all images were corrected for optical artifacts, including hot pixels caused by stray radiation, vignetting, lens distortions, and refraction at the tank-air interface, as described in chapter 2.

5.2.5 Study 1: Beam range measurement

5.2.5.1 Measurement parameters

The following parameters and setup details are specific to this study: the gantry was rotated to 270 deg., so that the proton beam entered the scintillator tank horizontally on the side opposite the mirror. In this orientation, the window-facing camera observed a lateral view of the proton beam, while the mirror-facing camera observed the beam's-eye-view. The cameras were set to acquire a sequence of 1-second exposures at a frame rate of 1 Hz. Because the PTCH system required 2 s to change from one beam energy to another, the 1 Hz frame rate ensured that there would never be more than one beam energy in a given image.

A sequence of 60 proton beams on the central beam axis with energies ranging from 72.5 MeV to 168.8 MeV was delivered to the tank and measured with the cameras. A total of 12 spots was delivered at each energy at the maximum intensity per spot, resulting in a total of 0.48 monitor units (MUs) per beam energy. The measurement of all 60 beams was completed in a single delivery sequence, requiring less than 3 minutes of beam time.

5.2.5.2 Data processing procedure

The detector was calibrated for range measurement using the following procedure. A set of images from an independent measurement with known beam energies and ranges was loaded and corrected for optical artifacts. The mirror-facing camera was used to identify the

distance from the proton beam to the window-facing camera. This distance must be accurately known in order to determine the effective pixel size and properly correct for refraction.

An image region around the proton pencil beam was selected and summed perpendicularly to the beam direction to form a one-dimensional (1D) depth-light curve. For each beam energy, the distal falloff region of the depth-light curve was fit with a smoothing spline, and the depth of the distal 80% of the depth-light curve was determined by interpolating this fit (Figure 5.2). Finally, a linear fit of the measured versus the nominal beam ranges provided the calibration factors needed for future range measurements (Figure 5.3).

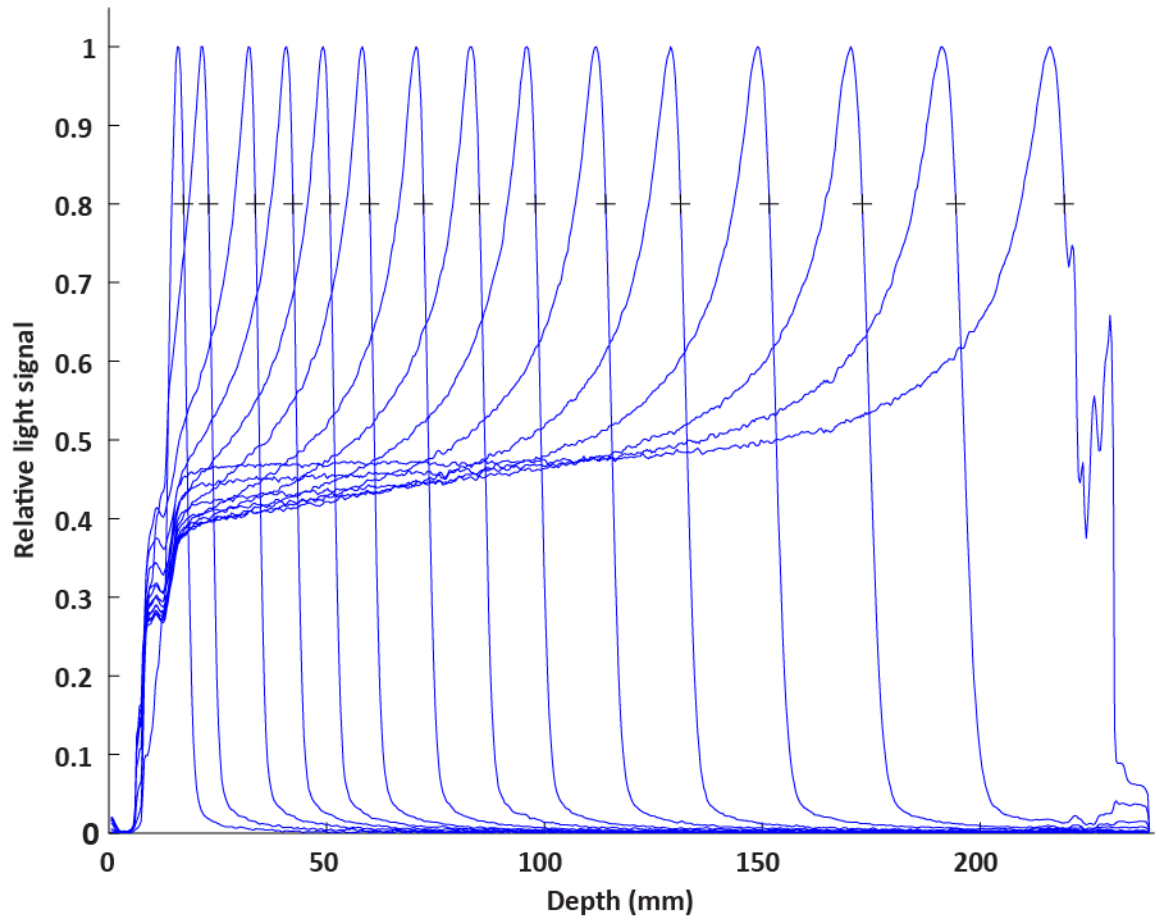


Figure 5.2 A series of proton beam scintillator depth-light curves used for beam range calibration (blue -), with the distal 80% of the light curve marked for each beam (black +).

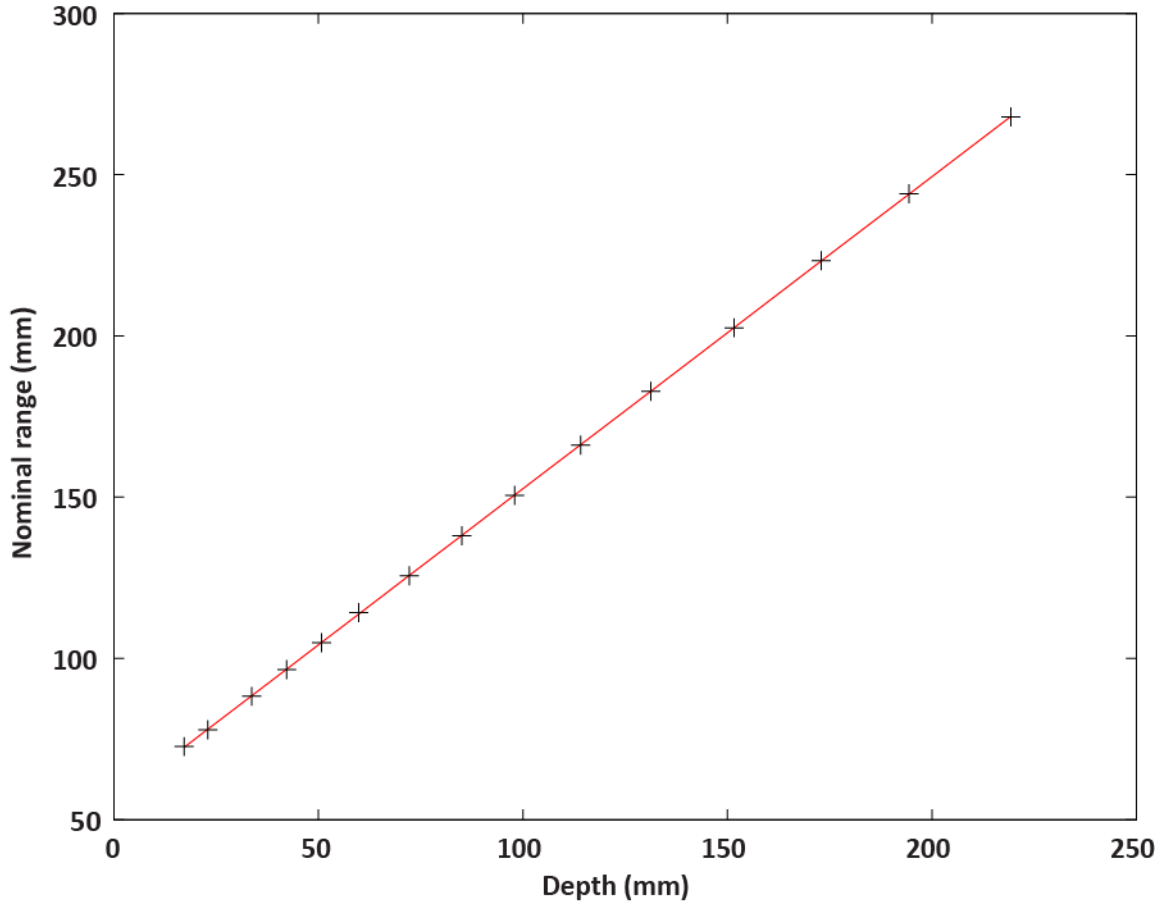


Figure 5.3 The measured distal 80% light signal vs. the nominal range (black +), and a calibration fit to the data (red -).

The slope of the linear fit is a range factor, ϕ , resulting from ionization quenching in the scintillator at the proton Bragg peak, as well as from the use of the distal 80% of the depth-light curve instead of the distal 90% of the depth-dose curve, which is the definition of range at the PTCH. The y-intercept of the linear fit is ζ , the zero depth in the camera reference frame. The value of the range factor from the calibration fit was $\phi = 0.968$.

The range measurement algorithm is similar to the range calibration algorithm, except that instead of performing a fit of the measured versus the nominal beam ranges, the actual beam ranges are determined using the equation

$$r_i = \frac{1}{\rho} (d_i \times \phi + \zeta) + b$$

where r_i is the range of the proton beam in water, ρ is the density of the liquid scintillator, d_i is the measured depth in the scintillator, ϕ is the range factor, ζ is the offset added to the measured depth to define zero depth, and b is the amount of water-equivalent buildup added in front of the scintillator tank. The image processing and data analysis calculations required less than one second of computation time per beam.

5.2.5.3 Data analysis

To evaluate the effectiveness of the range measurements, the measured ranges were compared to the nominal ranges of the proton beams. The measured ranges were also compared to a table of all of the beam energies and their corresponding ranges available in the PTCH system. For each measured beam range, the beam range in the table that was closest to the measured range was identified. To evaluate the accuracy of the range measurements, the mean and standard deviation of the differences between the measured and nominal ranges for all 60 beams were calculated.

5.2.6 Study 2: Lateral position measurement

5.2.6.1 Measurement parameters

The following parameters and setup details are specific to this study: the gantry was rotated to 0° , so that the proton beam entered the scintillator tank vertically through the lid. The cameras were set to acquire a sequence of 0.27 s exposures at a frame rate of 37 Hz. This is the maximum frame rate of the cameras at their full resolution. This high frame rate was selected in order to provide multiple measurements at each beam position, in order to study the variability in the beam position measurement procedure.

A pattern of proton beams at 5 different energies was delivered to the tank and measured with the cameras. The beam energies delivered were 85.6, 100.9, 124.0, 144.9, and 161.6 MeV, corresponding to beam ranges of 5.5, 7.5, 11.0, 14.5, and 17.6 cm. At each beam energy, proton

pencil beams were delivered to 9 different locations corresponding to a 3×3 grid of positions with 5 cm lateral and vertical spacing. A total of 50 beams were delivered at each beam position at the maximum intensity per beam, resulting in a total of 2 MUs per beam location.

The measurement of all 45 beams was completed in a single beam delivery, requiring less than one minute of beam time. Because the beam delivery was not synchronized with the image acquisition, some images contained light from two different beam locations. These images with multiple beams were removed from the data set. Because of this and the inherent variability of the beam delivery time, the number of image pairs per beam location varied from 6 to 13.

5.2.6.2 Data processing procedure

The selected beam images from both cameras were corrected for optical artifacts as described in section 2.5.2. In addition, these images were corrected for blurring by deconvolving a measured point spread function, as described in chapter 3. All images for each beam location were analyzed separately in order to evaluate the precision of the measurement technique.

First, the location of the distal 80% point of the depth-light curve was determined in each image. This was accomplished by fitting a Gaussian function to the lateral profile of the beam at multiple depths, and then fitting a line to the center of each Gaussian distribution. The light signal perpendicular to this line was integrated for form a 1D depth-light profile. The distal 80% of this profile was located via linear interpolation. For each image pair, the result was an (x,y) pixel position for each camera.

Second, triangulation was used to locate the distal 80% of the depth-light curve in real space inside the scintillator tank. Starting with the pair of (x,y) pixel positions from the previous step, the camera calibration model was used to project each point into real space, assuming the point was located in air at the focal plane. Using similar triangles and the known

distance between the camera and tank window, the pixel positions were projected to locations at the front surface of the tank window. The angle of incidence of the light ray at the air-window interface was determined, and the angle of the refracted light ray inside the tank was calculated using Snell's law. The angle and the location at the tank window were used to write the equation of a line in point-vector form for the refracted ray from each camera. The line from the window-facing camera was translated into the coordinate system of the mirror-facing camera using the extrinsic parameters from the stereo camera calibration, and then both lines were translated into the scintillator tank coordinate system.

The point of closest approach between the two lines was calculated using the following algorithm:

1. Calculate the unit vector perpendicular to both lines.
2. Define the perpendicular vector reaching from one line to the other.
3. Find the points of intersection of this vector with each line.
4. The average of the two intersection points is taken as the location in real space.
5. The distance between the intersection points is the distance of closest approach between the two lines. This value gives an indication of the accuracy of the point triangulation technique.

Finally, the distal 80% depth-light curve locations were projected back to the isocenter plane for comparison with the nominal positions. The projection accounted for the different source-axis distance (SAD) of the X- and Y-directions using the method described by Li et al. (2013).

The triangulation technique was verified using the camera calibration images. The calibration file for the stereo camera calibration contains a list of (x,y) pixel positions of the checkerboard corners imaged by both cameras for all calibration images. These corner positions were projected back into 3D space in the tank using the triangulation algorithm, and

the measured distance between corners was compared to the known size of the checkerboard squares.

The re-projected calibration data was also used to refine the values of the camera-tank distances used in the triangulation algorithm. A rough measurement of these distances with a tape measure was provided as the initial value, after which the camera-tank distance was optimized using the MATLAB optimization routines. The objective function to be minimized was the difference between the true size of the checkerboard squares and the measured distance between the re-projected checkerboard corners. Table 5.1 gives the mean and standard deviation of the corner-corner distances for all calibration images before and after optimization. The optimized values of the camera-tank distances were used in the triangulation of the beam locations.

Table 5.1 The mean and standard deviation of the corner-corner distances of the checkerboard calibration pattern before and after optimization of the camera-tank distances. The actual distance is 13.7 mm.

	Mean (mm)	Standard Deviation (mm)
Pre-optimization	13.42	0.271
Post-optimization	13.7	0.275

The detector system was designed to rigidly and reproducibly maintain the spatial relationship between the two cameras and the tank-and-mirror assembly. However, it was determined that the camera mounts allow up to one degree of rotation in the vertical and horizontal directions. Because the calibration and data acquisition were performed on different days, there was a possibility of a difference in the camera angle for these two measurements. Additionally, the focus distance wheels of the camera lenses were not rigidly fixed, which may have resulted in a small shift in the focus settings between the measurement of the calibration and proton beam data. This shift is expected to have a small impact on the effective focal

length of the lenses. The point triangulation algorithm is sensitive to small changes in the camera angle and focal length, so these small shifts could potentially cause significant systematic errors in the measured locations.

A systematic error was identified in the distance of closest approach of the projected rays in the measured data, and the uncertainties in the camera angles and focus distances were expected to be the cause. In an effort to correct for this systematic error, the camera angles and focal lengths were optimized using Matlab's nonlinear optimization routines, seeking to minimize the sum of the distance of closest approach of the projected rays for all measured beam positions. Figure 5.4 shows the closest approach of the projected rays for all image pairs before and after optimization of the focal length and the camera tilt angle. The optimized values of these parameters were used in the final beam position triangulation.

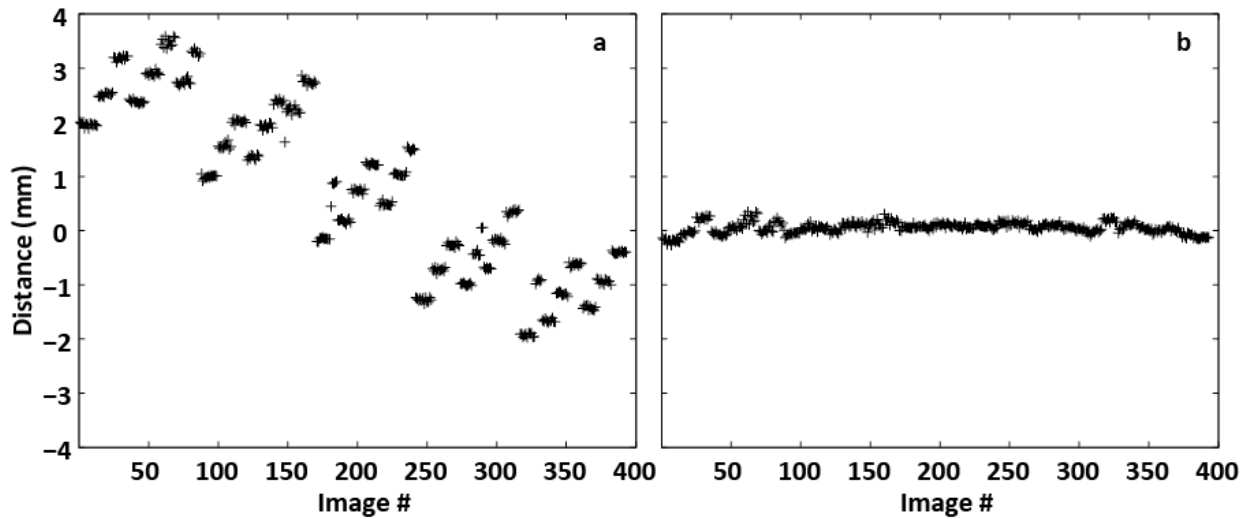


Figure 5.4 The distance of closest approach of the projected rays for all image pairs from the two cameras, (a) before and (b) after optimization of the focal length and the camera tilt angle.

The image processing and point triangulation procedures each required approximately 1 second per image. The data set analyzed here contained 390 images, requiring a total of 14 minutes computation time for image processing and 12 minutes for point triangulation. All

other processing steps required a fraction of a second per beam and were completed in about 1 minute for the entire data set.

5.2.6.3 Data analysis

To evaluate the consistency of the algorithm for automatically identifying the (x,y) pixel location of the distal 80% depth-light curve, the mean pixel location was calculated for the group of measurements at each beam location and energy. The distance of each pixel location from the mean was calculated, and the standard deviations of the distances from the mean for each location and for all locations together were calculated.

For the beam positions projected to the isocenter plane, the average distance of the measured points from the mean as well as the standard deviation of those distances were calculated for all beam locations and energies. In order to identify spatial trends and systematic errors, the average distance from the mean and the standard deviation were also evaluated for the set of all beam energies at each location.

5.2.7 Study 3: Lateral profile measurement

5.2.7.1 Measurement parameters

This study was completed using the data acquired in the first two studies.

5.2.7.2 Data processing procedure

The first step of the FWHM fitting procedure was to identify the maximum of the lateral profile. In order to decrease the effects of noise, the top 10% of the intensity values of the lateral profile were fit to a Gaussian function, and the maximum of the Gaussian was taken as the maximum of the lateral profile. The positions of the 50% values of the distribution were determined via linear interpolation. The calculations required less than one minute of computation time for each data set.

5.2.7.3 Data analysis

The FWHM was measured for all beam energies in the range measurement data set (section 2.5) and for the central-axis beams in the lateral position measurement data set (section 2.6). The range measurement data set provides a large number of different beam energies that can be compared with other measurements from the PTCH. The lateral position measurement data provides multiple sequential measurements at several beam energies, which can be used to evaluate the level of uncertainty in the FWHM measurement process.

The measured FWHM values were compared to the FWHM of profiles measured at the PTCH using a scanning pinpoint ionization chamber (Anand *et al.*, 2012). The mean and standard deviation of the FWHM were calculated for each of the 5 beam energies in the lateral position data set.

5.3 Results

5.3.1 Study 1: Beam range measurement

The depth-light curves of the 60 beam energies measured in this study are shown in Figure 5.5.

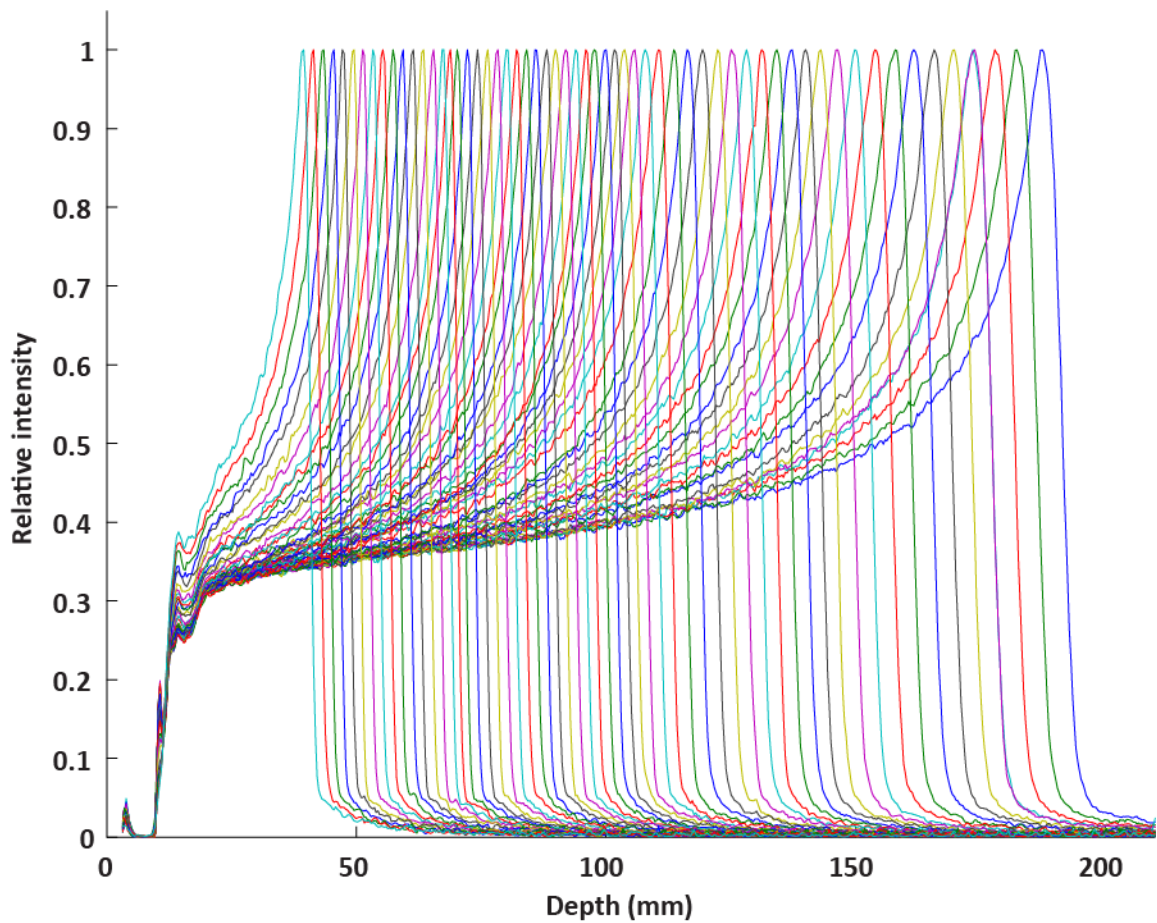


Figure 5.5 The depth-light curves of 60 beam energies measured with the scintillator detector. The first 2 cm of the light signal is absent due to the passage of the beam through the tank wall and tank-edge artifacts.

The mean of the differences between the measured and nominal beam ranges was 0.10 mm, and the standard deviation of the differences was 0.11 mm. All of the measured beam ranges matched the range of the correct nominal energy in the PTCH table of beam data. Table 5.2 gives the measured range, nominal range, and difference for all beam energies.

Table 5.2 Measured and nominal proton beam ranges.

Energy (MeV)	Measured Range (mm)	Nominal Range (mm)	Difference (mm)
168.8	190.0	190.0	0.0
166.2	185.0	185.0	0.0
163.9	180.5	180.5	0.0
161.6	176.0	176.0	0.0
161.6	176.0	176.0	0.0

159.5	171.9	172.0	-0.1
157.4	168.0	168.0	0.0
155.3	164.1	164.0	0.1
153.2	160.0	160.0	0.0
151	156.0	156.0	0.0
148.8	152.0	152.0	0.0
146.9	148.5	148.5	0.0
144.9	145.0	145.0	0.0
143.2	142.0	142.0	0.0
141.6	139.0	139.0	0.0
139.8	135.9	136.0	-0.1
138.1	133.0	133.0	0.0
136.4	130.0	130.0	0.0
134.6	127.1	127.0	0.1
132.8	124.1	124.0	0.1
131	121.1	121.0	0.1
129.2	118.0	118.0	0.0
127.4	115.1	115.0	0.1
125.6	112.1	112.0	0.1
124	109.6	109.5	0.1
122.5	107.1	107.0	0.1
121.2	105.2	105.0	0.2
119.9	103.1	103.0	0.1
118.6	101.2	101.0	0.2
117.3	99.1	99.0	0.1
116	97.1	97.0	0.1
114.7	95.1	95.0	0.1
113.4	93.2	93.0	0.2
112.1	91.2	91.0	0.2
110.7	89.1	89.0	0.1
109.4	87.1	87.0	0.1
108	85.2	85.0	0.2
106.6	83.2	83.0	0.2
105.2	81.1	81.0	0.1
103.8	79.2	79.0	0.2
102.4	77.2	77.0	0.2
100.9	75.2	75.0	0.2
99.5	73.2	73.0	0.2
98	71.2	71.0	0.2
96.9	69.7	70.0	-0.3
95.7	68.2	68.0	0.2
94.2	66.2	66.0	0.2

92.7	64.2	64.0	0.2
91.1	62.2	62.0	0.2
89.6	60.2	60.0	0.2
88	58.2	58.0	0.2
86.4	56.2	56.0	0.2
84.7	54.2	54.0	0.2
83.1	52.2	52.0	0.2
81.4	50.2	50.0	0.2
79.7	48.2	48.0	0.2
77.9	46.2	46.0	0.2
76.1	44.2	44.0	0.2
74.3	42.2	42.0	0.2
72.5	40.2	40.0	0.2

5.3.2 Study 2: Lateral position measurement

To evaluate the consistency of the algorithm for automatically identifying the (x,y) pixel location of the distal 80% depth-light curve, the standard deviation of the distance from the mean was calculated for all locations. For the window-facing camera, the standard deviation was 0.08 pixels, and for the mirror-facing camera the standard deviation was 0.07 pixels.

For the measured lateral beam positions at isocenter, Table 5.3 lists the difference between each nominal position and the mean of the measured position, as well as the standard deviation of the measured locations. Figure 5.6 plots the measured and nominal locations for all beams projected to the isocenter.

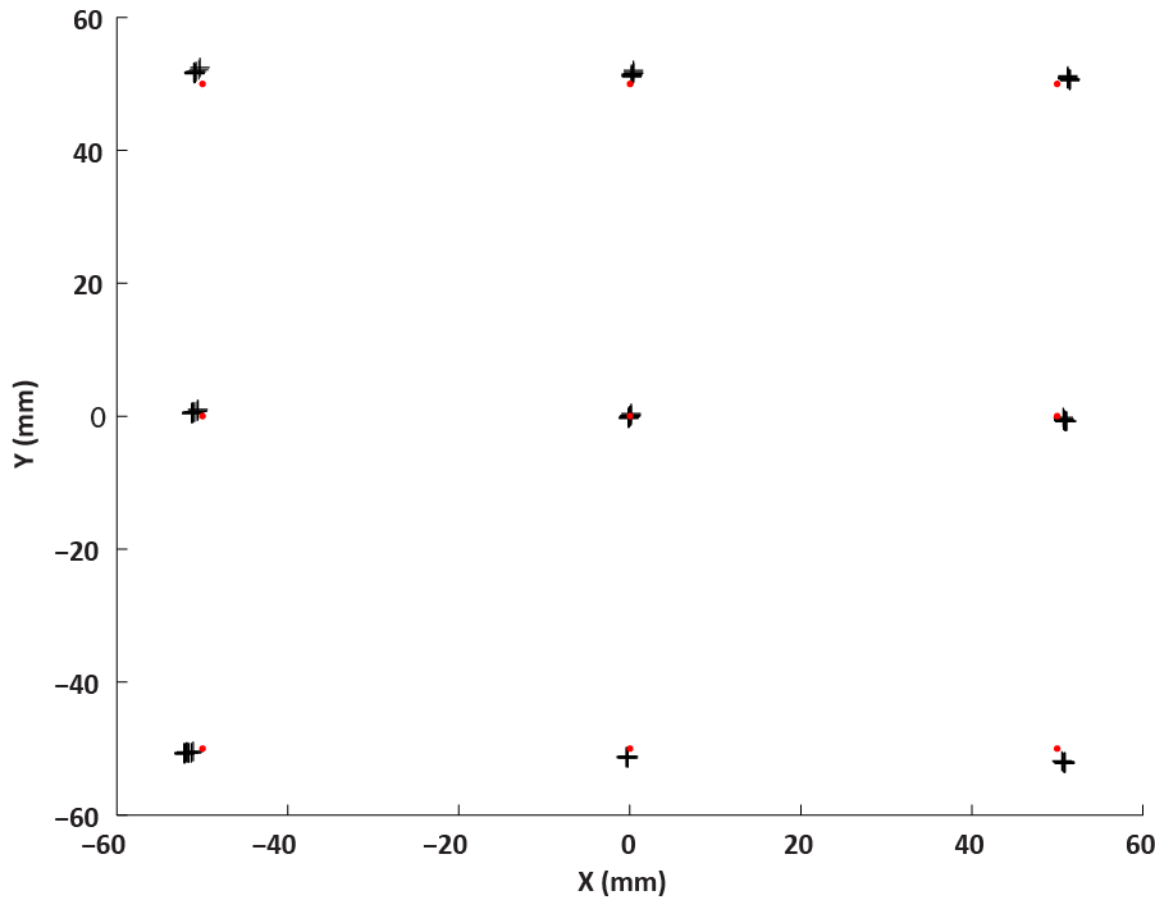


Figure 5.6 The measured (black +) and nominal (red •) lateral positions of proton beams of 5 energies at the isocenter plane.

Table 5.3 The difference between the nominal lateral position and the mean of the measured position, as well as the standard deviation of the measured locations.

Nominal position (mm)	Distance of mean from nominal (mm)	Standard Deviation (mm)
(-50,-50)	2.23	0.37
(0,-50)	1.69	0.21
(50,-50)	2.76	0.15
(-50,0)	1.50	0.19
(0,0)	0.22	0.15
(50,0)	1.36	0.20
(-50,50)	2.64	0.21
(0,50)	1.91	0.29
(50,50)	2.16	0.10

5.3.3 Study 3: Lateral profile measurement

Figure 5.7 shows the FWHM of 60 beam energies at the PTCH measured with the scintillator detector, compared with data measured with a pinpoint ionization chamber in a water tank (Anand *et al.*, 2012). The FWHM values measured with the scintillator are about 1 mm greater than those measured with the ionization chamber. Figure 5.8 shows the lateral profile of a 131 MeV proton beam measured with the scintillator detector and a scanned pinpoint ionization chamber.

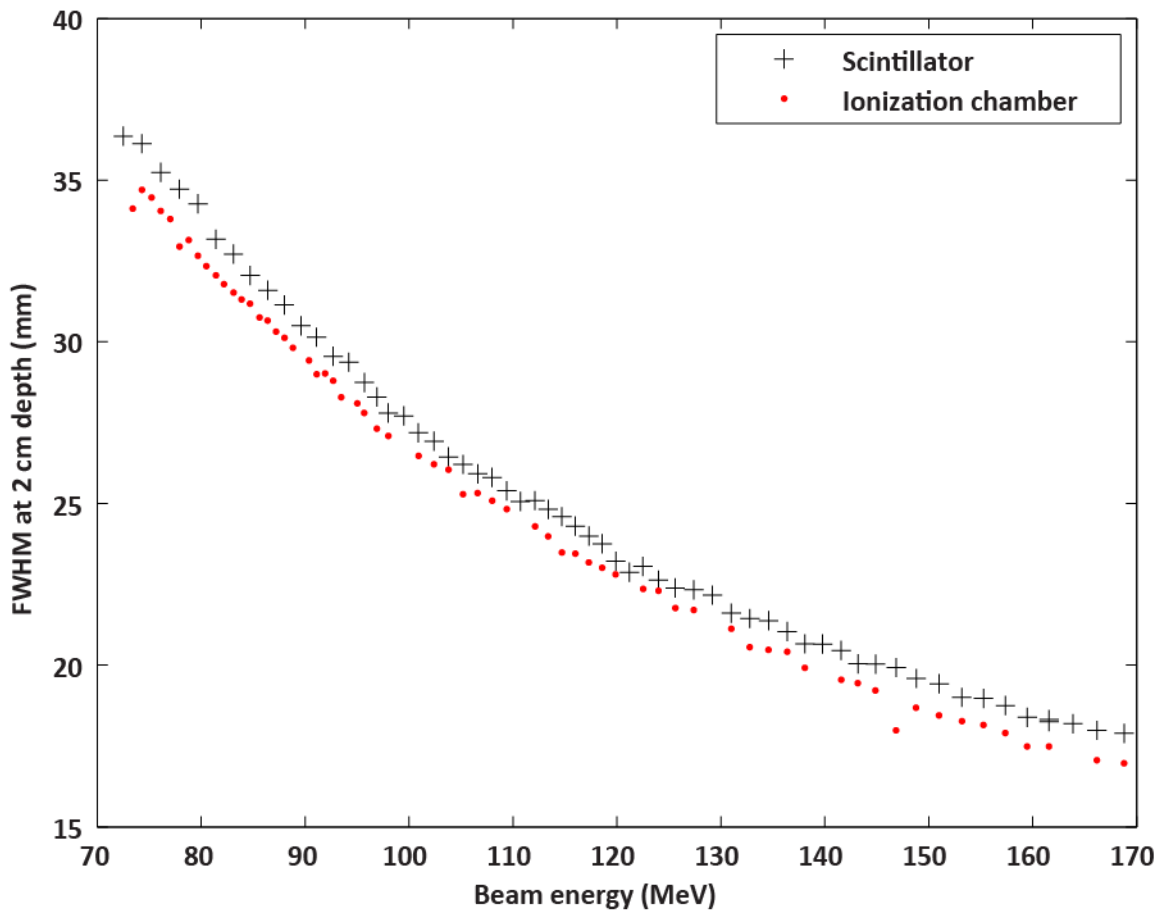


Figure 5.7 The full width at half-maximum (FWHM) of proton beams ranging from 72.5 MeV to 168.8 MeV, measured with the scintillator detector (black +) and a pinpoint ionization chamber (red •).

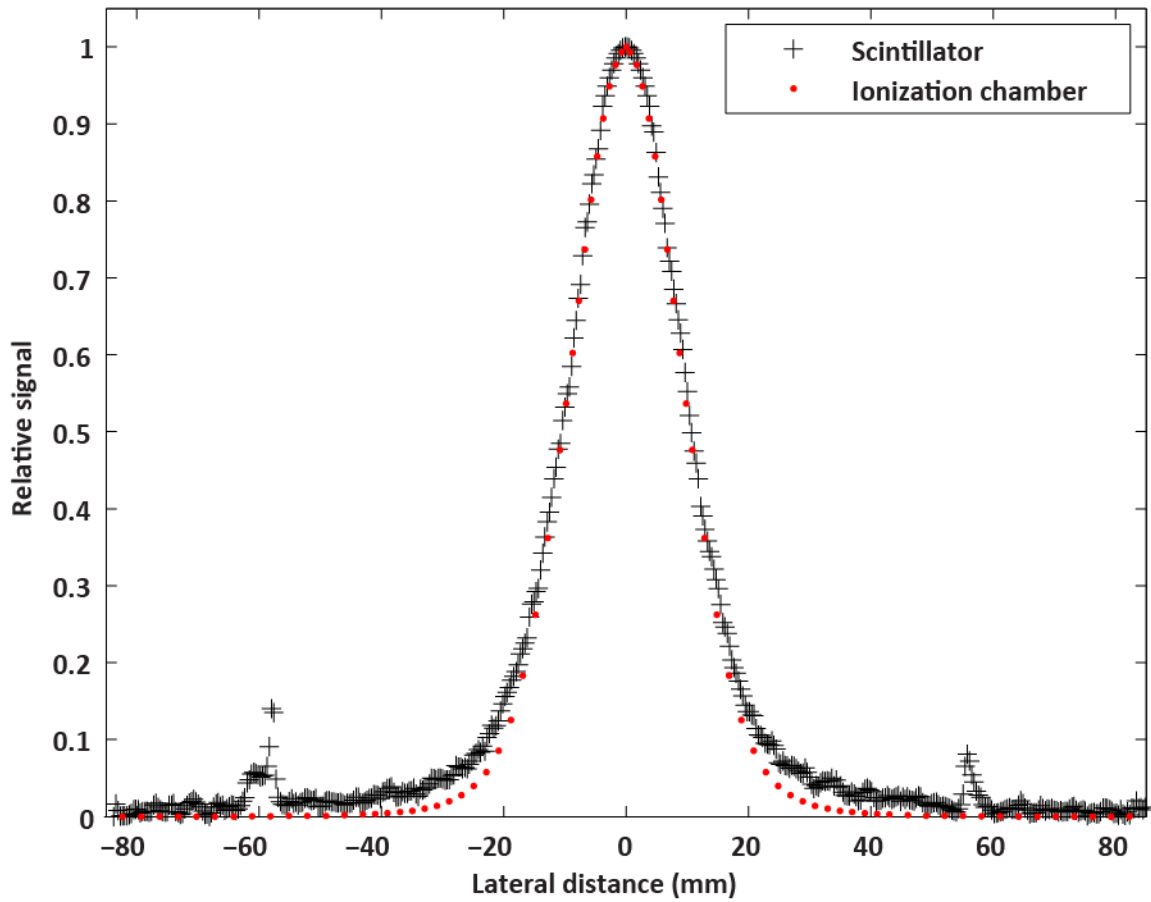


Figure 5.8 The lateral profile of a 131.0 MeV proton beam at a depth of 2 cm, measured with the scintillator detector (black +) and a pinpoint ionization chamber (red •). The spikes in the scintillator signal at -60 mm and 55 mm are reflections from screws in the scintillator tank assembly.

Table 5.4 lists the mean and standard deviation of multiple FWHM measurements for the five beam energies in the lateral position data set.

Table 5.4 Mean and standard deviation of proton beam FWHM for five beam energies.

Energy (MeV)	Mean FWHM (mm)	Standard deviation (mm)
85.6	32.4	0.7
100.9	27.9	0.5
124.0	22.6	0.3
144.9	19.4	0.4
161.6	17.7	0.3

5.4 Discussion

The measurements of the beam range, lateral position, and lateral profile FWHM were all found to be very precise. The measured beam ranges were accurate to within less than a millimeter, indicating that this detector is capable of clearly distinguishing between even the closely spaced low-energy beams, which are spaced at 1 mm intervals.

The lateral position measurements were very reproducible, and the automatic peak-finding algorithm was particularly stable, with variation less than a pixel despite the presence of noise in the images. The small standard deviations in the lateral position measurements at isocenter indicate the potential for highly accurate and reproducible lateral position measurements with this system. However, at the present time this accuracy is not realized due to a systematic error which results in the measured locations being 1-3 mm closer to the central axis than expected. This systematic error is likely caused by uncertainties in the camera alignment and focus setting, which may change from day to day as the detector is set up.

These errors required optimization of the camera angle and focal length parameters. A more rigid, reproducible detector design is expected to minimize these effects and provide a level off accuracy in lateral position measurements that would make this detector more suitable in a clinical QA role. In addition, improved optical engineering methods for measuring the focal length and the effective distance between the camera and tank window would simplify the detector calibration process and make it more robust.

The lateral profile measurements follow the same trend as those measured using a pinpoint ionization chamber, but with a FWHM approximately 1 mm larger. This discrepancy could be caused by several factors, including detector size effects, imperfections in the point spread function used for deblurring of the camera images, and uncertainties in the measurement of the maximum value of the lateral profile, which can have a large effect on the determination of the FWHM. This discrepancy is not a major concern in regard to the lateral

profile measurements, as the primary concern of a regular QA program is to check the consistency of the beam properties. In this study, high reproducibility was observed in the measurement of the lateral profile. The high resolution of the scintillator detector and the sub-millimeter standard deviation of its FWHM measurements suggest that it would be an effective tool for regular verification of the consistency of the proton beam lateral profile.

While the scintillator detector is very successful at quickly and efficiently measuring the parameters of many proton beams, the time required to set up and disassemble the current prototype detector is longer than other detectors currently used for daily QA measurements. These time requirements could be decreased with the design of a more optimized system. Although the setup time may prevent the use of this detector for daily beam checks, the detector could certainly save time in more comprehensive periodic QA measurements, such as monthly and annual QA and the verification of the treatment delivery system after major maintenance or component replacements.

The potential use of this detector for patient-specific QA measurements is clear. With modest improvements in the camera frame rate and with synchronization between the cameras and delivery system, the detector could efficiently check the spot positions, ranges, and intensities of all beams in an IMPT treatment plan prior to delivery. In its current state, the detector could measure the light distribution of individual energy layers in patient treatments with sufficient accuracy and resolution to detect discrepancies between the planned and delivered dose distributions. This application of the new prototype detector to patient-specific QA is the subject of ongoing work.

5.5 Conclusions

In conclusion, the novel liquid scintillator detector described in this study can provide fast, high-resolution measurements of the beam range, lateral position, and lateral profile for

therapeutic scanned proton beams. The precision of the detector was very good for all measurements in this study. The accuracy of the beam range measurements was exceptional. The lateral position measurements, while reproducible, were subject to a systematic error related to small variations in the camera angles and focus settings between the time of calibration and the beam measurements. The lateral profile measurements, while slightly wider than profiles measured using ionization chambers, followed the same trend of decreasing profile width with increasing energy.

The ability of the liquid scintillator detector to rapidly measure the beam range and lateral profile of many proton beams makes it particularly promising as a tool for scanned proton beam QA. This measurement efficiency could save valuable time in busy proton therapy clinics and facilitate more comprehensive commissioning and QA measurements than currently available techniques could provide.

CHAPTER 6

CONCLUSIONS AND FUTURE DIRECTIONS

6.1 Summary and conclusions

The body of work recorded in this dissertation comprises a few important steps in the development of three-dimensional scintillator-based radiation detectors for use in characterization of therapeutic radiation beams. While this promising area of study has many interesting problems to solve, this body of work is limited to the study and solution of three particular problems: the characterization and correction of optical artifacts, the characterization and correction of ionization quenching, and the measurement of important aspects of therapeutic scanned proton beams using a prototype volumetric scintillator detector.

The first study showed that optical artifacts have a significant effect on the spatial distribution of light measured with a volumetric scintillator detector. Of all artifacts considered, those which caused the largest changes in the measured light distribution were blurring caused by the lens and refraction at the interface between the air and the tank window. Contrary to expectations, scattering of the scintillation photons in the scintillator material was not found to be a significant source of optical artifacts.

Other artifacts that were considered include vignetting, lens distortion, and stray radiation directly impacting the image sensor. While these mechanisms produced visible effects in the detector images, the magnitude of these effects was small enough that they made little difference in the quantitative analysis of the light distributions. That being said, these effects may be more important for cameras with poor optics or different image sensors.

Correction strategies were developed for all optical artifacts evaluated in this study. These correction methods were primarily implemented through camera calibration and various image processing algorithms. When comparing theoretical calculations of the light output of individual proton beams to corrected images of the same proton beams, gamma analysis passing rates of 95% or greater were found in all cases using the stringent criteria of 2% of the local dose and 2 mm to agreement. This was a marked improvement over the 60 – 75% passing

rates of the uncorrected images. It was concluded that characterization and correction of optical artifacts is an essential step in obtaining accurate measurements of the light distributions produced in volumetric scintillator detectors.

The second study provided measurements of the relationship between the LET of the incident radiation beam and the level of light production in the scintillator. A correction method was developed for this LET-dependence, based on a semi-empirical model of the scintillator response. This approach requires prior knowledge of the LET distribution of the proton beam. The accuracy of analytical LET calculation methods was compared to the standard Monte Carlo radiation transport approach. The analytical method, while less accurate than the Monte Carlo approach, resulted in dose errors of less than 1% in the quenching-corrected data, suggesting that analytical LET calculations are sufficiently accurate for quenching correction. It was concluded that it is possible to correct for the LET-dependence of the scintillator response with an accuracy of $\pm 5\%$. The data suggested that an accuracy of $\pm 2-3\%$ could be achieved with improved measurements and better alignment between the light signal and LET distribution.

The third study described a new prototype volumetric scintillator detector featuring two cameras with orthogonal viewing directions. This detector was used to measure the range, lateral profile, and lateral position of scanned proton beams at multiple energies and lateral locations. The results were notable in the small amount of time required for the measurement of a large number of proton beams. They were also notable because of the high precision of all measurements and the high accuracy for the beam range and lateral profile measurements. A systematic error was found in the lateral position measurements performed with the system. Closer investigation indicated that the prototype system was prone to small setup errors in the camera angles and the focus settings, which resulted in differences between the state of the system at calibration and during data acquisition. The triangulation method used for lateral

position measurement was found to be particularly sensitive to these setup errors, leading to the observed systematic errors. A more robust and reproducible detector design is expected to eliminate these issues.

Despite the systematic errors found in the lateral position measurements, the new detector design shows the potential to significantly improve the efficiency and completeness of quality assurance for scanned proton beam delivery systems. The new detector design provides the novel capability of measuring proton beam range, lateral profile, and lateral position simultaneously and rapidly with high resolution. This will make it possible to perform more comprehensive commissioning and quality assurance measurements in a clinically practicable time frame, leading to increased patient safety and an improved capacity to detect beam delivery errors.

6.2 Evaluation of the hypothesis

Restatement of hypothesis: A large liquid scintillator detector can measure three-dimensional dosimetric information in scanned proton beams within 3% or 3 mm to agreement with calculated doses. Dose distributions and the locations and profiles of individual pencil beams can be measured during a single delivery of each treatment field.

The first element of the hypothesis relates to the measurement of 3D dosimetric information in scanned proton beams. With the current 2-camera detector prototype it is not possible to accurately reconstruct a complete 3D light emission distribution. However, 3D information on the range, lateral profile, and lateral position of individual proton beams was successfully measured. Additionally, two-dimensional projections of the 3D light distributions were evaluated for single proton beams in the second specific aim. The projected light signal was found to be within 2% or 2 mm to agreement with the calculated light signal based on

validated Monte Carlo calculations. In this respect, this element of the hypothesis was confirmed.

The second specific aim featured comparisons of measured and calculated central-axis depth-dose distributions of proton pencil beams after quenching correction. The dose error in the Bragg peak reached up to 5%. These errors were in regions of steep dose gradients, and were likely caused by a misalignment between the LET values and the light signal. However, this level of error is still large enough as to cast doubt on the effectiveness of volumetric scintillation detectors for measurements of dose distributions. Further work is needed to determine whether or not quenching correction can be performed to the level of accuracy required for dosimetric measurements.

The second element of the hypothesis relates to the measurement of the ranges, lateral positions and profiles of individual proton beams in the course of a single beam delivery. The results of the third specific aim demonstrated that beam ranges and lateral profiles could be measured with high accuracy and precision. Measurements of the lateral positions of proton beams suffered from a systematic error that was likely caused by uncertainties in the orientations and focus settings of the cameras from day to day. A more robust and reproducible detector design is expected to remedy this problem. With the caveat of the systematic error in the lateral position measurement, this element of the hypothesis was confirmed.

The measurements of range, lateral profile, and lateral position can be performed simultaneously in the course of a single delivery of a beam pattern. While the current cameras used in the prototype are not fast enough to measure each individual proton beam during the delivery of a scanned field, faster cameras are available, and the light intensity produced by the scintillator is sufficient for accurate measurements of individual beams. To measure each beam in a treatment without intensity loss due to camera dead time would also require

synchronization of the camera acquisition with the beam delivery system. While this has not yet been accomplished, it is technically feasible. For the purposes of QA measurements of the beam delivery system, control files can be prepared that deliver several sequential proton beams to the same location before moving to the next step in the pattern. This decreases the temporal resolution requirements such that the current detector prototype can measure the entire spot pattern in a single uninterrupted delivery. Given these results, this element of the hypothesis is confirmed.

6.3 Future directions

The work described in this dissertation opens the way for future developments in volumetric scintillation dosimetry. Some areas of future work that follow directly from this study include improvements in the detector design, further quenching studies, the development of 3D reconstruction methods, and the application of volumetric scintillation dosimetry to other therapeutic radiation sources.

Design improvements to be pursued include a more robust and reproducible assembly of the tank and camera components. This is expected to resolve systematic errors that occurred in the lateral position measurements. In addition to improving the alignment of the different detector components, self-calibration methods can be implemented to correct for day-to-day setup variations. An additional area for design improvements is the synchronization of the camera acquisition with the beam delivery system. This would allow for the measurement of individual proton spots during scanning delivery and remove the possibility of signal loss during the camera readout period.

While important progress in quenching correction was achieved in this study, additional work remains in this area. Quenching correction could be automated and the process streamlined to make it more clinically useful. More robust miniature liquid scintillator

detectors would improve in the characterization of the quenching coefficients of various liquid scintillators. Refinements in the quenching measurement and correction procedures are expected to bring the accuracy down to the level of $\pm 2-3\%$. Clearly, the best solution to quenching is to find a scintillator that does not exhibit an LET-dependent response. This is another interesting area of research.

While the current detector system can measure projections of 3D dose distributions, the addition of one or more additional camera angles should make it possible to perform a complete reconstruction of the scintillation light distribution in certain cases. This important development will harness one of the greatest potential benefits from volumetric scintillation dosimetry – a 3D dosimeter with high spatial and temporal resolution.

Finally, volumetric scintillation dosimetry could be useful in other radiotherapy modalities such as passive scattering proton therapy, intensity-modulated photon therapies, and even high-dose rate brachytherapy.

BIBLIOGRAPHY

- Anand A, Sahoo N, Zhu X R, Sawakuchi G O, Poenisch F, Amos R A, Ciangaru G, Titt U, Suzuki K, Mohan R and Gillin M T 2012 A procedure to determine the planar integral spot dose values of proton pencil beam spots *Med. Phys.* **39** 891-900
- Archambault L, Beddar A S, Gingras L, Lacroix F, Roy R and Beaulieu L 2007 Water-equivalent dosimeter array for small-field external beam radiotherapy *Med. Phys.* **34** 1583-92
- Archambault L, Briere T M and Beddar S 2008 Transient noise characterization and filtration in CCD cameras exposed to stray radiation from a medical linear accelerator *Med. Phys.* **35** 4342-51
- Archambault L, Poenisch F, Sahoo N, Robertson D, Lee A, Gillin M T, Mohan R and Beddar S 2012 Verification of proton range, position, and intensity in IMPT with a 3D liquid scintillator detector system *Med. Phys.* **39** 1239-46
- Arjomandy B, Sahoo N, Ciangaru G, Zhu R, Song X and Gillin M 2010 Verification of patient-specific dose distributions in proton therapy using a commercial two-dimensional ion chamber array *Med. Phys.* **37** 5831-7
- Arjomandy B, Sahoo N, Ding X N and Gillin M 2008 Use of a two-dimensional ionization chamber array for proton therapy beam quality assurance *Med. Phys.* **35** 3889-94
- Baldock C, De Deene Y, Doran S, Ibbott G, Jirasek A, Lepage M, McAuley K B, Oldham M and Schreiner L J 2010 Polymer gel dosimetry *Phys. Med. Biol.* **55** R1-R63
- Beddar A S 2006 Plastic scintillation dosimetry and its application to radiotherapy *Radiat. Meas.* **41**, **Supplement 1** S124-S33
- Beddar A S, Mackie T R and Attix F H 1992a Cerenkov Light Generated in Optical Fibers and Other Light Pipes Irradiated by Electron-Beams *Phys. Med. Biol.* **37** 925-35

- Beddar A S, Mackie T R and Attix F H 1992b Water-Equivalent Plastic Scintillation Detectors for High-Energy Beam Dosimetry .1. Physical Characteristics and Theoretical Considerations *Phys. Med. Biol.* **37** 1883-900
- Beddar A S, Mackie T R and Attix F H 1992c Water-Equivalent Plastic Scintillation Detectors for High-Energy Beam Dosimetry .2. Properties and Measurements *Phys. Med. Biol.* **37** 1901-13
- Beddar S, Archambault L, Sahoo N, Poenisch F, Chen G T, Gillin M T and Mohan R 2009 Exploration of the potential of liquid scintillators for real-time 3D dosimetry of intensity modulated proton beams *Med. Phys.* **36** 1736-43
- Berger M J 1993 Penetration of proton beams through water I. Depth-dose distribution, spectra, and LET distribution *NIST Interagency/Internal Report* (National Institute of Standard and Technology)
- Biggs D S C and Andrews M 1997 Acceleration of iterative image restoration algorithms *Appl. Opt.* **36** 1766-75
- Birks J B 1951 Scintillations from Organic Crystals: Specific Fluorescence and Relative Response to Different Radiations *Proc. Phys. Soc. Sec. A* **64** 874
- Birks J B 1964 *The Theory and Practice of Scintillation Counting* (Oxford, England: Pergamon Press)
- Boehling N S, Grosshans D R, Bluett J B, Palmer M T, Song X, Amos R A, Sahoo N, Meyer J J, Mahajan A and Woo S Y 2012 Dosimetric Comparison of Three-Dimensional Conformal Proton Radiotherapy, Intensity-Modulated Proton Therapy, and Intensity-Modulated Radiotherapy for Treatment of Pediatric Craniopharyngiomas *Int. J. Radiat. Oncol.* **82** 643-52

- Boon S N, van Luijk P, Bohringer T, Coray A, Lomax A, Pedroni E, Schaffner B and Schippers J M 2000 Performance of a fluorescent screen and CCD camera as a two-dimensional dosimetry system for dynamic treatment techniques *Med. Phys.* **27** 2198-208
- Boon S N, van Luijk P, Schippers J M, Meertens H, Denis J M, Vynckier S, Medin J and Grusell E 1998 Fast 2D phantom dosimetry for scanning proton beams *Med. Phys.* **25** 464-75
- Bortfeld T 1997 An analytical approximation of the Bragg curve for therapeutic proton beams *Med. Phys.* **24** 2024-33
- Bortfeld T and Schlegel W 1996 An analytical approximation of depth-dose distributions for therapeutic proton beams *Phys. Med. Biol.* **41** 1331-9
- Bouguet J-Y 2010 Camera Calibration Toolbox for Matlab (Pasadena, CA: California Institute of Technology)
- Caprile B and Torre V 1990 Using vanishing points for camera calibration *Int. J. Comput. Vision* **4** 127-39
- Chou C N 1952 The Nature of the Saturation Effect of Fluorescent Scintillators *Phys Rev* **87** 904
- Clasie B, Wroe A, Kooy H, Depauw N, Flanz J, Paganetti H and Rosenfeld A 2010 Assessment of out-of-field absorbed dose and equivalent dose in proton fields *Med. Phys.* **37** 311-21
- Collomb-Patton V, Boher P, Leroux T, Fontbonne J M, Vela A and Batalla A 2009 The DOSIMAP, a high spatial resolution tissue equivalent 2D dosimeter for LINAC QA and IMRT verification *Med. Phys.* **36** 317-28
- Coray A, Pedroni E, Bohringer T, Lin S, Lomax A and Goitein G 2002 Dosimetry with the scanned proton beam on the PSI gantry *Int. Symp. on Standards and Codes of Practice in Medical Radiation Dosimetry*, Vienna, Austria **IAEA-CN-96** 213
- Cruz-Galindo H S, Michaelian K, Martinez-Davalos A, Belmont-Moreno E and Galindo S 2002 Luminescence model with quantum impact parameter for low energy ions *Nucl. Instrum. Meth. B* **194** 319-22

- Dhanesar S, Sahoo N, Kerr M, Taylor M B, Summers P, Zhu X R, Poenisch F and Gillin M 2013 Quality assurance of proton beams using a multilayer ionization chamber system *Med. Phys.* **40**
- Fontenot J, Taddei P, Zheng Y, Mirkovic D, Jordan T and Newhauser W 2008 Equivalent dose and effective dose from stray radiation during passively scattered proton radiotherapy for prostate cancer *Phys. Med. Biol.* **53** 1677
- Fukushima Y, Hamada M, Nishio T and Maruyama K 2006 Development of an easy-to-handle range measurement tool using a plastic scintillator for proton beam therapy *Phys. Med. Biol.* **51** 5927-36
- Gillin M T, Sahoo N, Bues M, Ciangaru G, Sawakuchi G, Poenisch F, Arjomandy B, Martin C, Titt U, Suzuki K, Smith A R and Zhu X R 2010 Commissioning of the discrete spot scanning proton beam delivery system at the University of Texas MD Anderson Cancer Center, Proton Therapy Center, Houston *Med. Phys.* **37** 154-63
- Goldman D B 2010 Vignette and Exposure Calibration and Compensation *IEEE Trans. Pattern Analysis and Machine Intelligence* **32** 2276-88
- Grassberger C, Trofimov A, Lomax A and Paganetti H 2011 Variations in Linear Energy Transfer within Clinical Proton Therapy Fields and the Potential for Biological Treatment Planning *Int. J. Radiat. Oncol.* **80** 1559-66
- Guillot M, Beaulieu L, Archambault L, Beddar S and Gingras L 2011 A new water-equivalent 2D plastic scintillation detectors array for the dosimetry of megavoltage energy photon beams in radiation therapy *Med. Phys.* **38** 6763-74
- ICRU 1970 Linear energy transfer *ICRU Report No. 16* 1-51
- ICRU 1993 Stopping powers and ranges for protons and alpha particles *ICRU Report No. 49* 1-286

- ICRU 2007 Prescribing, recording, and reporting proton-beam therapy *ICRU Report No. 78* 1-222
- ISO 2000 ISO 12233: Photography -- Electronic still-picture cameras -- Resolution measurements (Geneva, Switzerland: International Organization for Standardization)
- Jordan K 2010 Review of recent advances in radiochromic materials for 3D dosimetry *J. Phys. Conf. Ser.* **250** 012043
- Karger C P, Jakel O, Hartmann G H and Heeg P 1999 A system for three-dimensional dosimetric verification of treatment plans in intensity-modulated radiotherapy with heavy ions *Med. Phys.* **26** 2125-32
- Karger C P, Jakel O, Palmans H and Kanai T 2010 Dosimetry for ion beam radiotherapy *Phys. Med. Biol.* **55** R193
- Kim C, Hong B, Jhang G, Joo E, Lee K S, Lee K S, Lee S, Lee S K, Park S K, Shim H H, Shin S S, Sim K S and Cha H K 2012a Measurement of Scintillation Responses of Scintillation Fibers for Dose Verification in Proton Therapy *J. Korean Phys. Soc.* **60** 725-30
- Kim J, Yoon M, Kim S, Shin D, Lee S B, Lim Y K, Kim D W and Park S Y 2012b Three-Dimensional Radiochromic Film Dosimetry of Proton Clinical Beams Using a Gafchromic Ebt2 Film Array *Radiat. Prot. Dosim.* **151** 272-7
- Kirov A S, Piao J Z, Mathur N, Miller T R, Devic S, Trichter S, Zaider M, LoSasso T and Soares C 2005a A test of the 3D scintillation dosimetry method for a Ru-106 eye plaque applicator *Med. Phys.* **32** 2002
- Kirov A S, Piao J Z, Mathur N K, Miller T R, Devic S, Trichter S, Zaider M, Soares C G and LoSasso T 2005b The three-dimensional scintillation dosimetry method: test for a Ru-106 eye plaque applicator *Phys. Med. Biol.* **50** 3063-81
- Kirov A S, Shrinivas S, Hurlbut C, Dempsey J F, Binns W R and Poblete J L 2000 New water equivalent liquid scintillation solutions for 3D dosimetry *Med. Phys.* **27** 1156-64

- Lee B, Jang K W, Cho D H, Yoo W J, Shin S H, Kim H S, Yi J H, Kim S, Cho H, Park B G and Moon J H 2008 Measurement of Two-Dimensional Photon Beam Distributions Using a Fiber-Optic Radiation Sensor for Small Field Radiation Therapy *IEEE Trans. Nucl. Sci.* **55** 2632-6
- Li H, Sahoo N, Poenisch F, Suzuki K, Li Y P, Li X Q, Zhang X D, Lee A K, Gillin M T and Zhu X R 2013 Use of treatment log files in spot scanning proton therapy as part of patient-specific quality assurance *Med. Phys.* **40**
- Litvinov A and Schechner Y Y 2005 Radiometric framework for image mosaicking *J. Opt. Soc. Am. A* **22** 839-48
- Lomax A J, Boehringer T, Coray A, Egger E, Goitein G, Grossmann M, Juelke P, Lin S, Pedroni E, Rohrer B, Roser W, Rossi B, Siegenthaler B, Stadelmann O, Stauble H, Vetter C and Wisser L 2001 Intensity modulated proton therapy: A clinical example *Med. Phys.* **28** 317-24
- Lomax A J, Bohringer T, Bolsi A, Coray D, Emert F, Goitein G, Jermann M, Lin S X, Pedroni E, Rutz H, Stadelmann O, Timmermann B, Verwey J and Weber D C 2004 Treatment planning and verification of proton therapy using spot scanning: Initial experiences *Med. Phys.* **31** 3150-7
- Low D A, Harms W B, Mutic S and Purdy J A 1998 A technique for the quantitative evaluation of dose distributions *Med. Phys.* **25** 656-61
- Menchaca-Rocha A 2009 A simplified scintillator-response formula for multiple-ion energy calibrations *Nucl. Instrum. Methods Sec. A* **602** 421-4
- Michaelian K and Menchacarocha A 1994 Model of Ion-Induced Luminescence Based on Energy Deposition by Secondary Electrons *Phys. Rev. B* **49** 15550-62

- Mouatassim S, Costa G J, Guillaume G, Heusch B, Huck A and Moszynski M 1995 The Light Yield Response of Ne213 Organic Scintillators to Charged-Particles Resulting from Neutron Interactions *Nucl. Instrum. Methods Sec. A* **359** 530-6
- Papadopoulos L 1999 Scintillation response of organic and inorganic scintillators *Nucl. Instrum. Methods Sec. A* **434** 337-44
- Pedroni E, Scheib S, Bohringer T, Coray A, Grossmann M, Lin S and Lomax A 2005 Experimental characterization and physical modelling of the dose distribution of scanned proton pencil beams *Phys. Med. Biol.* **50** 541-61
- Ponisch F, Archambault L, Briere T M, Sahoo N, Mohan R, Beddar S and Gillin M T 2009 Liquid scintillator for 2D dosimetry for high-energy photon beams *Med. Phys.* **36** 1478-85
- Ray S F 1994 *Applied Photographic Optics: Lenses and Optical Systems for Photography, Film, Video, and Electronic Imaging* (Woburn, MA: Focal Press)
- Robertson D, Mirkovic D, Sahoo N and Beddar S 2013 Quenching correction for volumetric scintillation dosimetry of proton beams *Phys. Med. Biol.* **58** 261-73
- Robertson D, Hui C, Archambault L, Mohan R and Beddar S 2014 Optical artifact characterization and correction in volumetric scintillation dosimetry *Phys. Med. Biol.* **59** 23-42
- Safai S, Lin S X and Pedroni E 2004 Development of an inorganic scintillating mixture for proton beam verification dosimetry *Phys. Med. Biol.* **49** 4637-55
- Sawakuchi G O, Mirkovic D, Perles L A, Sahoo N, Zhu X R, Ciangaru G, Suzuki K, Gillin M T, Mohan R and Titt U 2010a An MCNPX Monte Carlo model of a discrete spot scanning proton beam therapy nozzle *Med. Phys.* **37** 4960-70

- Sawakuchi G O, Sahoo N, Gasparian P B R, Rodriguez M G, Archambault L, Titt U and Yukihiro E G 2010b Determination of average LET of therapeutic proton beams using Al₂O₃:C optically stimulated luminescence (OSL) detectors *Phys. Med. Biol.* **55** 4963-76
- Shih Y, Guenter B and Joshi N 2012 Image Enhancement Using Calibrated Lens Simulations *Computer Vision – ECCV 2012*, ed A Fitzgibbon, *et al.*: Springer Berlin Heidelberg) pp 42-56
- Smith A, Gillin M, Bues M, Zhu X R, Suzuki K, Mohan R, Woo S, Lee A, Komaki R, Cox J, Hiramoto K, Akiyama H, Ishida T, Sasaki T and Matsuda K 2009 The M. D. Anderson proton therapy system *Med. Phys.* **36** 4068-83
- Smith D L, Polk R G and Miller T G 1968 Measurement of the response of several organic scintillators to electrons, protons, and deuterons *Nucl. Instrum. Methods* **64** 157-66
- Tilly N, Grusell E, Kimstrand P, Lorin S, Gajewski K, Pettersson M, Backlund A and Glimelius B 2007 Development and verification of the pulsed scanned proton beam at The Svedberg Laboratory in Uppsala *Phys. Med. Biol.* **52** 2741-54
- Tilly N, Johansson J, Isacson U, Medin J, Blomquist E, Grusell E and Glimelius B 2005 The influence of RBE variations in a clinical proton treatment plan for a hypopharynx cancer *Phys. Med. Biol.* **50** 2765-77
- Tobias C A, Lawrence J H, Born J L, Mc C R, Roberts J E, Anger H O, Low-Beer B V and Huggins C B 1958 Pituitary irradiation with high-energy proton beams: a preliminary report *Cancer Res.* **18** 121-34
- Torrisi L, Desiderio A and Foti G 2000 High energy proton induced luminescence in F-doped polyvinyltoluene *Nucl. Instrum. Methods Sec. B* **166** 664-8
- Tsai R Y 1992 A versatile camera calibration technique for high-accuracy 3D machine vision metrology using off-the-shelf TV cameras and lenses *Radiometry*, ed L B Wolff, S A Shafer and G Healey (Burlington, MA: Jones and Bartlett Publishers, Inc.) pp 221-44

- Wang L L and Tsai W H 1990 Computing camera parameters using vanishing-line information from a rectangular parallelepiped *Machine Vision and Applications* **3** 129-41
- Wang L L W, Perles L A, Archambault L, Sahoo N, Mirkovic D and Beddar S 2012 Determination of the quenching correction factors for plastic scintillation detectors in therapeutic high-energy proton beams *Phys. Med. Biol.* **57** 7767-82
- Waters L S, Hendricks J and McKinney G 2002 Monte Carlo N-Particle Transport Code system for Multiparticle and High Energy Applications (Los Alamos, NM: Los Alamos National Laboratory)
- Wilkens J J and Oelfke U 2003 Analytical linear energy transfer calculations for proton therapy *Med. Phys.* **30** 806-15
- Wilkens J J and Oelfke U 2004 Three-dimensional LET calculations for treatment planning of proton therapy **14** 41-6
- Wilson R R 1946 Radiological Use of Fast Protons *Radiology* **47** 487-91
- Yoshida S, Ebihara T, Yano T, Kozlov A, Kishimoto T, Ogawa I, Hazama R, Umehara S, Mukaida K, Ichihara K, Hirano Y, Murata I, Datemichi J and Sugimoto H 2010 Light output response of KamLAND liquid scintillator for protons and C-12 nuclei *Nucl. Instrum. Methods Sec. A* **622** 574-82
- Zeidan O A, Sriprisan S I, Lopatiuk-Tirpak O, Kupelian P A, Meeks S L, Hsi W C, Li Z, Palta J R and Maryanski M J 2010 Dosimetric evaluation of a novel polymer gel dosimeter for proton therapy *Med. Phys.* **37** 2145-52
- Zhang Z 1999 Flexible camera calibration by viewing a plane from unknown orientations *Proc. 7th IEEE Int. Conf. Computer Vision*, **1** 666-73
- Zhu X R, Poenisch F, Lii M, Sawakuchi G O, Titt U, Bues M, Song X, Zhang X, Li Y, Ciangaru G, Li H, Taylor M B, Suzuki K, Mohan R, Gillin M T and Sahoo N 2013 Commissioning

dose computation models for spot scanning proton beams in water for a commercially available treatment planning system *Med. Phys.* **40**

Zhu X R, Poenisch F, Song X F, Johnson J L, Ciangaru G, Taylor M B, Lii M, Martin C, Arjomandy B, Lee A K, Choi S, Nguyen Q N, Gillin M T and Sahoo N 2011 Patient-Specific Quality Assurance for Prostate Cancer Patients Receiving Spot Scanning Proton Therapy Using Single-Field Uniform Dose *Int. J. Radiat. Oncol.* **81** 552-9

VITA

Daniel Gordon Robertson was born in Lebanon, New Hampshire on May 28, 1983. He is the second of four children born to Mark and Theresa Robertson. The family moved to Saint George, Utah in 1990, where he attended primary and secondary school. Daniel graduated from Pine View High School in 2001, and went on to study physics at Brigham Young University the same year. He interrupted his studies during the summer of 2002 to serve for two years as a full-time missionary of the Church of Jesus Christ of Latter-day Saints in the Connecticut, Hartford mission. Daniel returned to Brigham Young University and graduated in 2008, majoring in Applied Physics with a minor in Music. In the Fall of 2008 he entered The University of Texas Graduate School of Biomedical Sciences at Houston. Daniel is married to Angela Marie Robertson, and they are the parents of Mark Berg Robertson, who was born on June 4, 2013.

Permanent address:

1104 East Lizzie Lane
Saint George, Utah 84790